Slow body magnetohydrodynamic waves in solar photospheric flux tubes with inhomogeneous equilibria

Fisal Asiri

Supervisors:
Dr Istvan Ballai
Dr Gary Verth
Prof Viktor Fedun

The University Of Sheffield.

University of Sheffield

School of Mathematics and Statistics

A thesis submitted in partial fulfilment of the requirements for the degree of

Doctor of Philosophy

May, 2024

Acknowledgements

I want to start by expressing my sincere gratitude to God.

I wish to express my sincere gratitude and appreciation to my Ph.D. supervisors, Drs. Istvan Ballai, Gary Verth, and Prof Viktor Fedun for their unwavering support and direction. Thanks to their scientific, original, and intelligent direction, I was able to overcome numerous obstacles and successfully accomplish this work. It was an enormous honour and privilege for me to work under their supervision.

I would like to express my gratitude to all of the individuals whose assistance and suggestions allowed me to successfully complete this Thesis. I would like to convey my sincere gratitude to my advisor, Dr. Julia M. Rees, for her support, encouragement, and academic counsel.

I owe a debt of appreciation to my parents, siblings, and other family members and friends who have always supported and believed in my abilities to obtain a Ph.D. I am grateful for all of their support, kindness, and love over the years. Without you, none of this would have been possible. Dedicating this Thesis to you makes me pleased.

I would like to thank Dr. Abdulrahman B Albidah, my colleague, for his suggestions and assisting during my studies, unwavering support, and academic guidance.

Finally, I would like to express my gratitude to the Saudi Government, Ministry of Education, Taibah University, the Royal Saudi Embassy in London, and the Saudi Cultural Bureau in London for their support of my University of Sheffield studies.

Declaration of Authorship

I hereby declare that, except where clear reference is made to the work of others, the contents of this dissertation are original and have not, in whole or in part, been submitted to this or any other university for consideration for any other degree or qualification. This dissertation is my own work and contains nothing which is the outcome of work done in collaboration with others, except as specified in the text and Acknowledgements. This dissertation contains fewer than 80,000 words including appendices, bibliography, footnotes, tables, figures and equations.

Fisal Asiri
Friday 31st May, 2024

Abstract

Intense magnetic waveguides in the solar photosphere, such as pores and sunspots are ideal environments for the propagation of guided waves. However, modelling these photospheric waveguides with varying background quantities such as plasma density and magnetic field has thus far been very limited. Such modelling is required to correctly interpret MHD waves observed in pores and sunspots with resolved inhomogeneities such as light bridges and umbral dots. Theoretical descriptions of waves are very sensitive to the way density is distributed and configuration of waveguides. Current theoretical models assume a homogeneous distribution of plasma parameters and magnetic field. High resolution observations of the last decade show that these assumptions are very crude and alterations from this ideal setup are expected to have a major effect on the property of waves. One major impediment in extending the existing theoretical modelling to more realistic situations was the complexity of the mathematical framework in which waves are investigated.

The aim of my research presented in this Thesis is to address this shortcoming and propose analytical and numerical techniques for wave identification in the presence of inhomogeneous magnetic waveguides. Here, we provide two various types of models that can be used to investigate slow MHD modes in solar photospheric flux tubes in the presence of local equilibrium density, pressure and magnetic field inhomogeneity. In all studied cases, the equilibrium profile inhomogeneity is represented by a local circular enhancement or depletion whose strength, size and position can change.

First, we investigate the propagation characteristics and the spatial structure of slow body eigenmodes in a magnetic flux tube with circular cross section. For analytical progress we assume that

the model has constant plasma-β, assuming that only the plasma equilibrium density has a spatial dependence.

Later, the constant plasma-β model (which is a rather restrictive approximation) is relaxed and results of the modification of the properties and morphology of slow body modes are investigated considering a case where not only the equilibrium density as function of coordinates, but also equilibrium pressure and magnetic field, in line with observations and numerical modelling. Analytical progress was made by considering that the plasma pressure and density vary following the same dependency on coordinates, meaning that we are dealing with a constant sound speed, i.e. isothermal equilibrium. Given the complexity of the problem, the task was addressed numerically via the Fourier-Chebyshev Spectral method (FCS), as well as Galerkin Finite Element method (FEM), respectively. The radial and azimuthal variation of eigenfunctions is obtained by solving a Helmholtz-type partial differential equation with Dirichlet boundary conditions for slow body waves.

The inhomogeneous transverse equilibrium density profile results in modified eigenvalues and eigenvectors. In particular, a modification in the equilibrium density distribution leads to a decrease in the eigenvalues and the spatial structure of modes ceases to be global, as the modes migrate towards regions of lower density in the case of the constant plasma-β model. Comparing the homogeneous case and the cases corresponding to depleted density enhancement, the dimensionless phase speed undergoes a significant drop in its value (at least 40%). In contrast to the density enhancement, the slow body modes investigated here preserve their morphology.

Our investigations can be considered as a very first step in studying the properties of waves in sunspots and pores in the presence of local inhomogeneities in the form of umbral dots (UDs) and light bridges (LBs). Multistructure density distributions (as observations show) can often be replaced by a resulting structure that adequately captures the effects of multiple UDs present in the sunspot umbra. This means that the equilibrium density inhomogeneity profile is represented by a single local density inhomogene-

ity, which simulates the UDs observed in the sunspot umbra region, assuming that they are placed close to each other. Furthermore, the LB observed in sunspots can be modeled by a single local density inhomogeneity that separates the sunspot umbra region. The more complex the shape of the density inhomogeneity, the spatial structure of the higher-order slow-body modes will be modified depending on the considered density shape and the cross-sectional configuration of the waveguide. As a result, the pattern of possible waves loses the high-degree of symmetry one can meet in homogeneous cases, especially for higher-order modes, which means that the pattern is no longer global and, therefore, cannot be easily identified. Local wave observations in sunspots may be a way to identify the location and size of density inhomogeneities in the umbra region.

These intriguing findings have significant ramifications for optimising modal structures that may be viewed, compared, and correlated in observational data as well as for constructing and organising modes in circular structures.

List of Publications

This Thesis is based on the following publications:

- Asiri, F., Ballai, I., Fedun, V., Verth, G., Ruzheinikov, S. N., Albidah, A. B. (2024). Slow body magnetohydrodynamic waves in solar photospheric flux tubes with density inhomogeneity. Monthly Notices of the Royal Astronomical Society, stae497.
- Asiri, F., Ballai, I., Fedun, V., Verth, G,. *Slow body MHD wave modes in isothermal and inhomogeneous flux tubes*, MRAS (in preparation).
- Asiri, F., Ballai, I., Fedun, V., Verth, G., *Slow body MHD wave modes of solar magnetic flux tubes with multi-stranded inhomogeneity* MNRAS (in preparation).

Contents

List of Figures

List of Tables

CHAPTER 1

Introduction

1.1 A synopsis of the Sun's history and formation.

For thousands of years mankind has been fascinated by the Sun, a magnificent celestial object that has attracted scientific interest and inquiry. Despite centuries of solar-related discoveries, a large number of solar phenomena continue to confound scientists and several questions regarding their nature and evolution remain unanswered. The first solar eclipse documented by modern humans in 800 BC marked the beginning of the exploration of the Sun. With the advent of telescopes, solar studies received a new impetus. Using the available optical advances, Galileo Galilei (1564-1642) developed his telescope that was able to perform a thirty-times magnification. With the help of this instrument he was able to observe "imperfections" on the surface of the Sun, which he labelled as sunspots. As he observed a clear translational movement of sunspots across the solar disk, he concluded that the Sun rotates. In the 19th century solar spectroscopy introduced by William Herschel opened up a novel investigation pathway for celestial bodies (including the Sun) and he was the first scientist to detect infrared radiations in 1800. One year later, Johann Willhelm, detected solar ultraviolet radiation.

Nowadays, extensive studies are conducted using a myriad of high-resolution ground-based telescopes (e.g. Swedish Solar Telescope (SST), Vacuum Tower Telescope (VTT), Daniel K. Inouye Solar Telescope (DKIST), etc.), and space-based telescopes (e.g. Solar and Heliospheric Observatory (SOHO), Interface Region Imaging Spectrograph (IRIS), Transition Region and Coronal Explorer (TRACE), Solar-B (Hinode), Solar Dynamic Observatory (SDO), Solar Orbiter, etc.) in an attempt to understand the intricate aspects of mechanisms

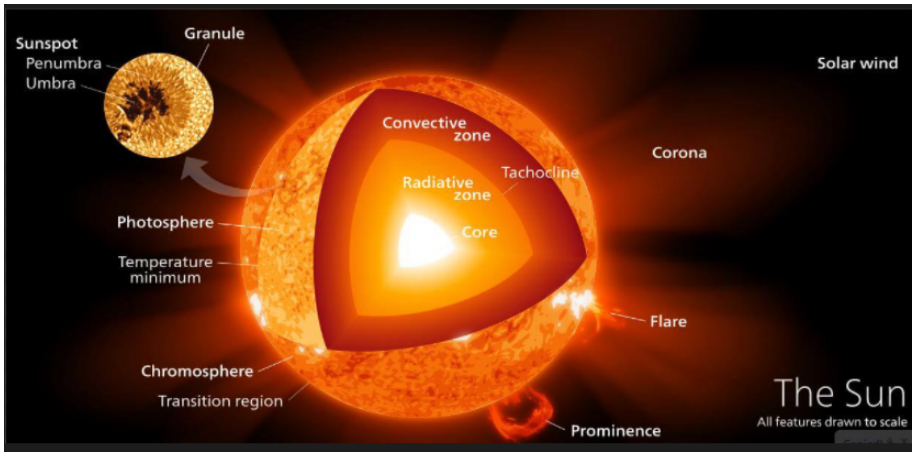

Figure 1.1: A schematic picture of the solar interior (the core, radiative zone, and convective zone) and its atmosphere (photosphere, chromosphere, transition region, and corona). The picture also displays several solar transient atmospheric events, including sunspots, solar flares, prominences, and coronal loops Priest (2014*a*).

that control the processes of variability and activity of the Sun. Over the years, these studies have accumulated extensive and important information regarding different aspects of the Sun, such as its structure, the role of the magnetic field, the connectivity of various regions in the solar atmosphere, the generation and evolution of large and energetic phenomena across many spatial scales, its activity, etc. However, these studies have not provided adequate and enough information to allow a comprehensive understanding of the physics behind different phenomena of the Sun that occur at very small scales.

The Sun is a massive ball of plasma compressed by its own gravitational attraction. It mainly comprises hydrogen (91.7%) and helium (7.3%) atoms. In addition, about 1% of the remaining structure consists of heavier elements such as carbon, nitrogen and oxygen Priest (2014*a*). Due to high temperatures in the Sun, the matter is found in the plasma state (the fourth state of matter), which is an ionized gas whose behaviour is controlled by electromagnetic fields and that shows collective motion. The movement of the plasma generates strong electric and magnetic fields and corresponding electric currents. Unless a separate reference is specified, the majority of the current section is based on work by Aschwanden (2004); Priest (2014*b*), and should be regarded as references.

Broadly speaking the regions in the solar visible atmosphere can be classified as belonging to the quiet or the active Sun. The quiet Sun is defined

as a plasma ball that is static, spherically symmetric, whose properties vary based on radial distance from the centre and for which the magnetic field is negligible. Conversely, the active Sun has a significant magnetic field that results in a range of transient phenomena, such as sunspots, prominences, solar flares and coronal mass ejections (CMEs), as shown in Fig. 1.1. The sunspots are located in the photosphere which are regions where intense magnetic fields emerge to the solar surface. They have a reduced surface temperature and tend to be darker than their surroundings, due to magnetic field flux concentrations that inhibit convection. Prominences are bright, large, gaseous features anchored in the photosphere on the surface of the Sun, and further extend in outward direction into the Solar corona, often in a loop shape. Solar flares are sudden energy explosions induced by magnetic field line interactions near sunspots. Coronal mass ejections occur at the location of topological reorganisation of the magnetic field of the solar corona and are associated with an immense amount of particle and radiation emission into the solar wind and the interplanetary space.

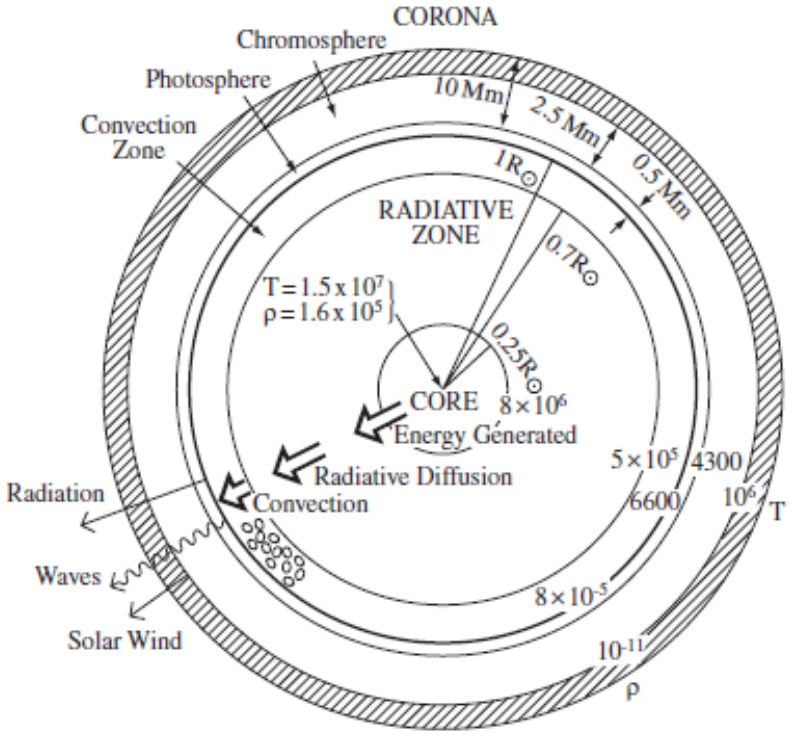

Figure 1.2: Schematic diagram of the inner layers of the Sun. Credit: Priest (2014*a*).

The Sun's ability to have a tremendous impact on the highly advanced and

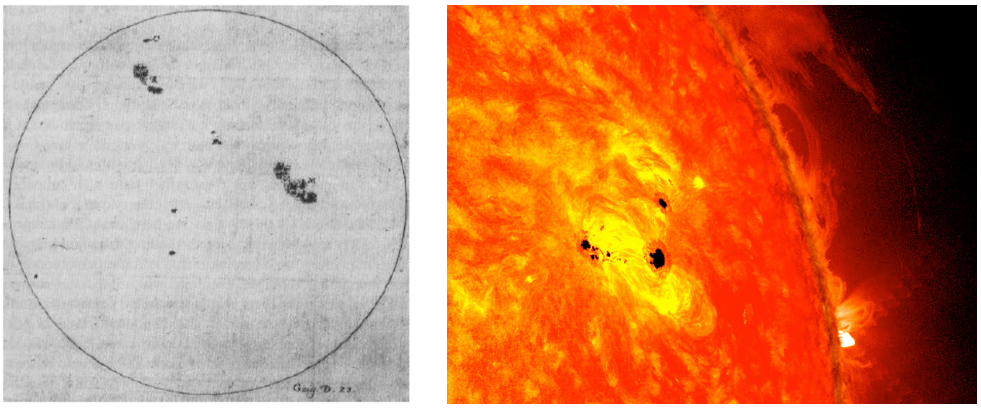

Figure 1.3: Galileo Galilei's drawing of a sunspot in the 1612 (left panel). The active zone of the Sun with its dark sunspots is depicted in the right panel. Credit: *Solar Dynamics Observatory (SDO)*.

technology-based human world is another important aspect for which the Sun is studied. Magnetic fields and energetic particles are constantly being transported in the outermost layer of the solar atmosphere. Storm conditions in the solar atmosphere can, therefore, carry radiation and energetic particles from the Sun to Earth, impacting satellites used for communication, power grids and other ground-based technology. Therefore, in order to avoid dangerous repercussions on our technology, it is imperative that we comprehend the primary mechanics underlying energetic solar activity events. Stated differently, research on the solar atmosphere facilitates a more profound comprehension of the processes governing space weather phenomena and the circumstances surrounding near-Earth space.

1.1.1 The structure of the Sun

The Sun, generally speaking, can be divided into two natural parts, the interior and its atmosphere, each with very distinct physics. The solar interior is the region of the Sun that is shielded from our view, while the atmosphere is defined as the region where light can escape and, therefore, it can be studied in a much more detailed way.

The solar interior (for a schematic picture, see Fig. 1.2) is the location where nuclear reactions take place and where the magnetic field is generated. The core is the hottest region of the Sun (and the whole solar system), with a radius of about $0.25R_{\odot}$ from the centre. The core has a temperature $T = 1.5 \times 10^7$ K and a density of $\rho = 1.6 \times 10^5$ kg m $^{-3}$. At this high

temperature and density, hydrogen nuclei interact by nuclear fusion to form helium, a mechanism that releases massive amounts of energy. This energy travels outwards towards the outer layers of the Sun. As the distance from the center of the core increases, there are significant changes in the properties and characteristic behaviors of the Sun. Enveloping the core is the radiative zone that has a temperature of about 7 million K. The energy emitted from the core is transported through radiation (hence the name of this region) and it passes through the radiative zone incredibly slowly as photons can travel only a few millimetres before they are absorbed, later released. Therefore, a photon could travel through the radiative zone for as long as 50 million years. The radiative region of the Sun extends to distances of about $0.7R_{\odot}$. With the increase of the distance from the core the density of the plasma also decreases. At the top of the radiative zone the density reaches a lower value and the energy starts to be transported by convection and the region where this transport mechanism is dominant is called the convective zone that extends till the surface of the Sun. Hot and dense material is convected towards from the top of the radiative zone towards the surface, and in this journey the plasma cools down and becomes less dense. Convective cells reaching the solar surface become visible and they form the granular network we can see in white light observations. Convection also transports the magnetic field that is generated in the solar interior by dynamo effects to the surface and becomes visible as, e.g. sunspots and pores.

The solar atmosphere is the region that can be sampled by observing the radiation emitted by the plasma in various wavelengths. This radiation is observed either as emission or absorption lines in the electromagnetic spectrum. Traditionally, the atmosphere is divided into four regions, each with their own distinctive properties. First, we have the dense and relatively cool photosphere (with a thickness of about 500 km) that is dominated by the granular motion and is the layer where the emerging large-scale magnetic field becomes visible (discussed in detail later). At these heights, the magnetic field is mostly vertical. In this region the temperature reaches its minimum value (approximately 4,300 K).

The chromosphere is the next layer of thickness of about 1500-2000 km where temperature rises steadily to about 20,000 K (see Fig. 1.4) and it can be considered as one of the most dynamic regions of the solar atmosphere. The chromosphere is also the location where the plasma is changing from being

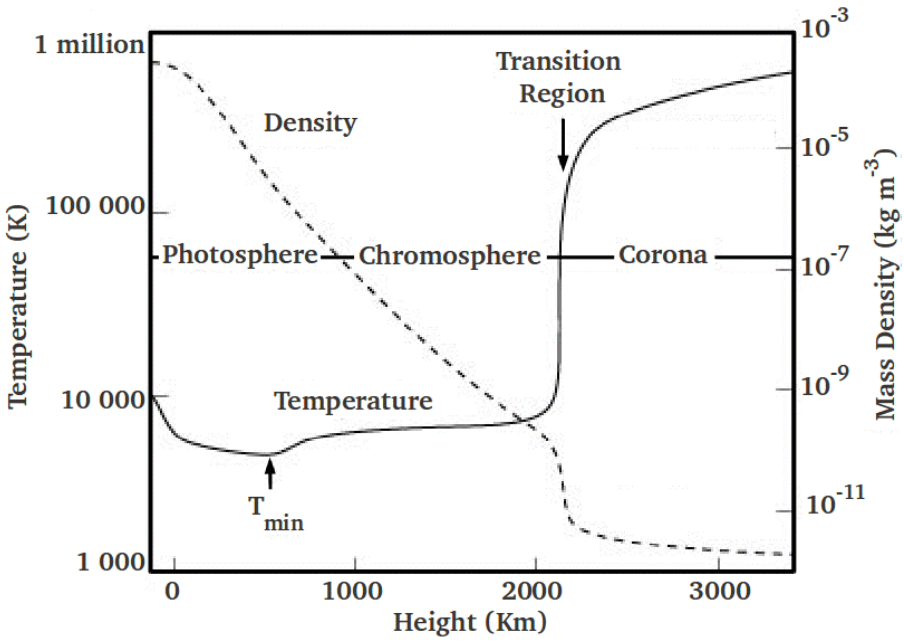

Figure 1.4: Variation of the temperature and density with height in the solar atmosphere (Priest, 2014*a*).

partially ionised to fully ionised, from optically thick to optically thin and from being pressure force-driven to magnetic force-driven. The magnetic field becomes more inclined forming the magnetic network and it is responsible for the existence of several phenomena in the chromosphere such as prominences and spicules. Prominences are luminous ionised gas eruptions (when seen on the limb) that may stretch thousands of kilometres from the chromosphere to corona Nakariakov and Kolotkov (2020), Kerr (2023). When seen on the solar disk, these features are called fibrils. Spicules are defined as dynamic jets that stretch from the photosphere to the chromosphere Bose et al. (2021), Srivastava et al. (2023).

At the interface between the chromosphere and corona, we have the transition region which is a very thin layer (approximately 100 km thick), where the temperature has a very steep increase from a few ten thousand to million degrees Kelvin (see Fig. 1.4). Finally, the corona is the layer that extends well into the interplanetary space. The corona cannot normally be seen in visible light because of the dazzling light of the photosphere, except in eclipses or with coronagraphs (in which a masking disk is used to eliminate the photospheric emission). Early observations of the visible spectrum of the corona revealed

bright emission lines at wavelengths that did not correspond to any known materials. The true nature of the corona remained a mystery until it was determined that coronal gases are heated to temperatures greater than 1,000,000 K. At these high temperatures both hydrogen and helium (the two dominant elements) are completely stripped of their electrons. Only the heavier trace elements like iron and calcium are able to retain a few of their electrons in this high temperature and are able to produce the spectral emission lines that were so mysterious to nineteenth century astronomers.

The peculiar variation of the temperature with height shown in Fig. (1.4) constitutes the foundation of what is known as the *coronal heating problem*, one of the biggest mysteries surrounding our Sun. The nature of the processes that heat the corona, maintain it at these high temperatures and accelerate the solar wind is still unknown. Usually temperatures fall as you move away from a heat source (like in the case of the solar interior), however as Fig. (1.4) shows, over a relatively short distance, the temperature suddenly rises to extremely high values. For this behaviour thermal energy must be continually supplied to maintain such temperature against radiative cooling. Several mechanisms have been suggested as the source of this heating, however a definite answer as to what mechanisms act in the solar atmosphere to provide the necessary heat still eludes the scientists. Broadly speaking the proposed mechanisms are divided into AC heating mechanisms (basically heating by transferring the kinetic energy of waves into heat) and DC mechanisms (the transformation of magnetic energy into heat). Nowadays there is wide consensus that coronal heating is a complex process where both AC and DC mechanisms act to maintain the high temperature of the plasma. As such, the coronal heating problem remains one of the most challenging questions in solar physics Nicholeen et al. (2022), De Pontieu et al. (2022), Sigalotti and Cruz (2023), Shi et al. (2024) and Enerhaug et al. (2024).

The solar magnetic field is one of the most important physical quantities that controls the dynamical and thermodynamical state of the plasma, as well as its stability. In the solar chromosphere and corona the magnetic field determines the structure and the behaviour of the plasma. High resolution observations in the corona are able to provide evidence for the intricate structuring of the magnetism. It is clear that the magnetic field in these regions is not diffuse, instead it tends to accumulate into entities of different sizes (e.g. magnetic flux tubes, coronal loops, etc.). In general we can talk about two

types of regions, depending on whether the magnetic field lines are open and connect to the interplanetary field (coronal holes) or closed over the surface, so that field lines form arches with their two endpoints in the photosphere, with small-scale energetic features (X-ray bright points) scattered over all the Sun's surface. Closed regions are in fact composed of myriads of coronal loops, with a wide range of dimensions, densities and temperatures.

1.2 Magnetic structures in the solar photosphere: pores and sunspots

The research presented in this Thesis deals with the properties of waves in photospheric magnetic structures, such as magnetic pores and sunspots. Although the magnetism in the solar photosphere is not as complicated as in the case of other solar regions, its relative simplicity offers the chance to study them better.

Sunspots are large, transient, tubes of magnetic flux located in the photosphere whose intricate structure appear not just due to their uneven distribution of magnetic field and density, but also due to "invisible" external forces that are responsible for their dynamic behaviour. Sunspots are magnetic structures whose transverse shape changes over time, influencing the type and characteristics of waves that propagate along (and across) these structures. The transversal shape of a realistic waveguide is far from being regular such as a circle. They have reduced surface temperature and tend to be darker than the surrounding areas due to magnetic field flux concentrations that inhibit convection. The sunspots consist of a dark central part named umbra (with more vertical magnetic field) and a brighter and striated part with more inclined magnetic field surrounding the umbra known as penumbra (see Fig. 1.5). The actual temperature of sunspots is, on average, 3,800 K, while that of the photosphere is 5,800 K (Jess et al., 2015). Sunspots first appear in the photosphere as little darkish spots with no penumbra. These features are known as solar pores (smallest flux tubes) (Solanki, 2003). Pores increase in their size and can get closer together over time. When a pore becomes large enough (in diameter, typically around 3,500 km), a penumbra begins to form. Pores are located along the dividing lines between larger sunspots. The strength of the magnetic field in sunspots can be measured (using, e.g. the Zeeman or Hanle

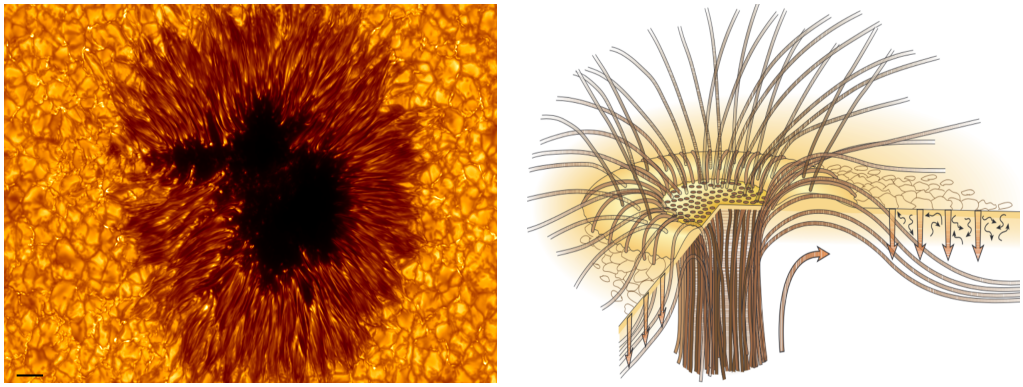

Figure 1.5: The left panel shows a high-resolution view of a sunspot. The dark area in the centre is the umbra, surrounded by the striated penumbra. Credit: *The Swedish Solar Telescope (SST)*. The right panel shows schematically the topology of the magnetic field in a sunspot. The convection motion is shown by arrows. Credit: Thomas et al. (2002).

effects) and the field strength varies between 1000 and 3000 G.

A particular manifestation of inhomogeneities in pores and the umbral region of sunspots are umbral dots (UDs) (see Fig. 1.6), which are regions of limited extent believed to play an important role in the energy balance in sunspots (Solanki, 2003). Light-bridges are luminous material channels that separate the umbra of a sunspot and indicate sunspot decay or fragmentation. They are frequently detected during sunspot break-up and may indicate the re-establishment of convection, which is generally prevented by the sunspots' strong magnetic field. They have been shown to have greatly improved chromospheric brightness and activity, including jets and surges (Cristaldi et al., 2014; Louis et al., 2014; Hou et al., 2020; Zhao et al., 2022). In light bridges, the intensity of the magnetic field is diminished and it tends to be more horizontal. The emergence of a new light bridge or the brightening of an existing one could indicate the fragmentation and disintegration of the sunspot. The study by Sobotka and Hanslmeier (2005) showed that umbral dots are hotter than the coldest region in the umbra by 1000 K and colder than the undisturbed photosphere after analysing observations of two sunspots and two pores. The core and periphery of umbral dots are used to categorise them. Central dots appear in the interior of the umbra, while peripheral dots appear near the edge of the umbra. Peripheral dots are brighter and their magnetic field is weaker (and slanted). Umbral dots appear in regions where the magnetic field is weaker and inclined and disappear where the magnetic field is greater and

vertical (Watanabe et al., 2009).

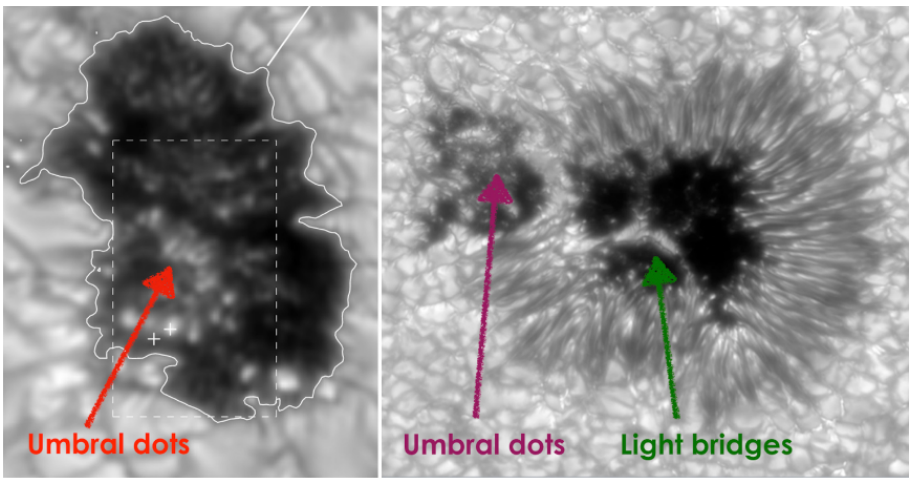

Figure 1.6: Left panel shows the sunspot with umbral dots and the right panel shows the sunspots with both umbral dots and light bridges. Credit: Yadav and Mathew (2018).

1.2.1 Waves and Oscillations in Sunspots

The study of solar oscillations began with the identification of standing pressure waves (acoustic global p modes) that can travel deep inside the solar interior and reflect upward in the photosphere (Leighton et al., 1962). These waves are used to determine the state of the plasma in the solar interior using various techniques imported from seismology (helioseismology). The existence of waves and oscillations in sunspots has been extensively studied since Beckers and Tallant (1969)'s pioneering work demonstrated the oscillatory behavior of sunspots by measuring observed parameters of umbral flashes. Later, Bhatnagar (1971) detected oscillations of the order of $180-220$ s in Doppler velocity in sunspots. Beckers and Schultz (1972) detected the umbral sunspot's vertical velocity oscillation for a period of three minutes. More research into the problem of Doppler velocity oscillations has been conducted by Moore (1981), who discovered Doppler velocity oscillations in the umbral and penumbral regions of the order of $120-180s$ and $240-300s$, respectively. Bhatnagar and Tanaka (1972) measured the intensity directly from time lapse filtergram movies to find oscillations with a period of 170 ± 40 s. With the wealth of detection of oscillatory behaviour in and around sunspots it became clear that the oscillations vary in frequency and strength depending on which layer the oscillations

are found. The study by Thomas et al. (1984) found 3.5 mHz ($\sim$ 5-min) oscillations in the photospheric layer and 6 mHz ($\sim$ 3-min) in the chromospheric layers. As a result, as the wave gets closer to the chromosphere above the umbra, its power multiplies by more than ten. Sunspot umbrae's chromospheric oscillations are nonlinear that can often steepen into shock waves (Lites, 1984). These shock waves are believed to be responsible for the heating of the non-magnetic solar chromosphere (Erdélyi and Ballai, 2007).

Subsequent studies have shown that the most significant oscillation periods in sunspots and pores are 5 minutes at photospheric heights and 3 minutes at chromospheric heights, while the periods of global sunspot oscillations vary from hours to days (Stangalini et al., 2011; Jess et al., 2012, 2015; Grant et al., 2015). In addition, Stangalini et al. (2021) demonstrated that, in contrast to the anticipated 5 minutes, the dominant oscillations of a magnetic pore observed with the Interferometric BIdimensional Spectropolarimeter (IBIS) have periods of 3 minutes in the photosphere. Nagashima et al. (2007) studied the spatial distribution of the power spectral density of the oscillatory signal in and around an active region (AR) using high-resolution observations from the Solar Optical Telescope (SOT) onboard Hinode. In all the observed frequency ranges, the oscillatory power was suppressed in the umbra. On the other hand, oscillations in the umbra, also known as umbral flashes, could be clearly seen in CaII H intensity maps, with the power peaking at about 5.5 mHz (3 minutes). The CaII H power distribution also revealed enhanced elements with the umbral flashes' spatial scale throughout the majority of the umbra, with an area of suppressed power in the centre. Xu et al. (2017) investigated the relationship between 3-min and 5-min oscillations in sunspots, obtaining that running waves propagate through the umbra–penumbra as 3-min oscillations in the umbra region and 5-min oscillations in the penumbra region.

The study of magnetohydrodynamics (MHD) modes and their characteristics in the sunspot umbra region has also made extensive use of the wavelet time series analysis. The umbral regions of an observed sunspot were subjected to a combined wavelet and Fourier analysis using various spectral lines that cover the range of temperatures from the low chromosphere to the corona in order to show the existence of oscillations at all investigated temperatures, with frequencies in the range of 5.4 mHz to 8.9 mHz O'shea et al. (2002). The 3-min oscillations in the sunspot umbral zone were identified using this technique by Christopoulou et al. (2003). Jess et al. (2017) recently used H_α

observations by the Hydrogen-Alpha Rapid Dynamics camera (HARDcam) to find slow body kink patterns travelling along the azimuthal path of a sunspot. In order to isolate the major umbral oscillations and the larger spatial fluctuations, the authors applied a temporal and spatial bandpass Fourier filter encompassing ($5 < \omega < 6.3$ mHz) and ($0.45 - 0.90$ arcsec^{-1}).

The study by Keys et al. (2018) revealed the distinct existence of surface and body surface sausage modes (modes that propagate without disturbing the symmetry axis of the magnetic flux tube, discussed in detail in Chapter 2) propagating in all the 7 investigated pores, the majority of which had elliptical cross sections. In order to determine the sausage mode, their study involved taking a one-dimensional cross-cut along the pore and measuring the power at the pore's edge and at its centre during the time series. The authors identified the types of the modes by imposing the conditions according to which the amplitude of surface waves has its maximum at the boundary and its minimum at the centre of the pore, whereas the amplitude of body modes has its maximum at the centre and minimum at the boundary. However, in reality, in a magnetic structure of elliptical cross-section the magnitude of the surface sausage mode reaches its maximum amplitude at the boundary along the minor axis and its minimal amplitude at the boundary along the main axis, as recently demonstrated by Aldhafeeri et al. (2021). As a result, the assumption made by Keys et al. (2018) may only be true for pores with roughly circular cross sections. The recent study by Albidah et al. (2021*b*) addressed this problem and demonstrated how the Proper Orthogonal Decomposition (POD) and Dynamic Mode Decomposition (DMD) methodologies are accurate at simultaneously identifying surface and body modes.

In a recent study, Jess et al. (2017) used HARDcam H_α images in conjunction with $k-\omega$ Fourier filter to evidence slow body kink modes travelling along the azimuthal direction in the chromospheric umbra of sunspot with periods of 170 s. For the same set of observations Albidah et al. (2021*b*) employed the POD/DMD techniques to recover not only the fundamental slow body sausage and kink modes propagating in a sunspot, but also the existence of higher order modes (also called fluting modes) that were elusive for solar physicists for a very long time. The possibility that observed oscillatory wave patterns are due to existence of fluting modes was proposed Kang et al. (2019), who suggested that the observed two-armed spiral wave patterns in pores could be explained in terms of a superposition of slow sausage body mode (corresponding to an

azimuthal wavenumber $n = 0$) and a fluting mode ($n = 2$) using ground-based observations with the 1.6 m Goode Solar Telescope. However, their study did not include a correlation analysis to verify the results obtained between the numerically simulated and observed modes. Another result of the study by Albidah et al. (2022*b*), who employed a pixel-by-pixel cross-correlation analysis to compare modes observed in observational data and theoretical models. This investigation demonstrated that the irregularities in the shape of the waveguide influence mainly the higher order modes.

Recent research by Gilchrist-Millar et al. (2021) used inversions of spectropolarimetric Si I 10827 Å data to further constrain sausage-mode damping in a series of adjacent pores and identify extensive wave damping in the lower solar atmosphere. Using chromospheric spectral data that are further defined with regard to future solar missions, these authors also determined the nature of the observed waves as they cross into the chromosphere and investigated the effect the characteristics of pores have on wave propagation. The study by Riedl et al. (2021) suggested that sausage modes were generated by localised drivers in the pore and were damped by wave leakage as well as geometric effects from the attenuation of the magnetic field as a function of height. Grant et al. (2022) investigated the propagation of coherent waves across several solar magnetic pores. Since isolated and/or disconnected structures frequently appear in pores, wave activity as a function of atmospheric height cannot be statistically examined. These authors studied photospheric and chromospheric wave signatures from a distinctive collection of magnetic pores emanating from the same sunspot using high-resolution data by the Dunn Solar Telescope. Through comparisons of intensity and area variations, wavelet analysis of high-cadence photospheric imaging revealed the universal presence of slow sausage-mode oscillations that are coherent across all photospheric pores and result in statistically significant in-phase connections. They also discovered fine-scale 5 mHz power amplification as the waves traveled into the chromosphere by using bisector Doppler velocity analysis of the Ca II 8542 Å line. Examining the intensity and velocity signals from individual pores revealed that they behave as fractured waveguides rather than monolithic structures, which is consistent with the Fourier analysis of chromospheric velocities between neighbouring pores, which revealed the annihilation of the wave coherency observed in the photosphere. This work is significant because it shows how complex wave morphology is with atmospheric height and how

large changes may be seen at different chromospheric layers even if equal wave modes are put into similar photosphere pores.

Finally, the study by Stangalini et al. (2022) found large-scale coherent magnetohydrodynamic oscillations in solar sunspots. Although theoretically possible, it has not yet been proven that many resonant modes in sunspots are excited simultaneously. Extremely large sunspots did not exhibit several simultaneous resonant modes, with the exception of a few solitary low order eigenmodes in small scale magnetic structures. In their study these authors discovered the largest-scale coherent oscillations ever seen in a sunspot. These oscillations have a spectrum that differs greatly from the Sun's regular global acoustic oscillations and they are a superposition of a number of resonant waves.

1.3 Aims and Thesis outline

One of the most challenging aspects of modern solar physics is describing the plasma dynamics qualitatively and quantitatively. This challenge arises from the combined complexity of dynamics and the complicated interplay between magnetic fields and flows, as well as the limited analytical tools we have to describe a realistic dynamics. MHD waves and oscillations result from the various plasma motions that are subject to restoring forces (such as pressure gradient, gravitational force, Lorentz force, etc.). Without these restoring forces, perturbations could develop into shocks, nonlinear patterns, laminar and turbulent flows, instabilities, etc. MHD waves are essential tools to describe and understand the dynamics, heating, energy and momentum transport, and stability in the solar atmosphere. In particular, intense magnetic waveguides in the solar atmosphere, such as pores, sunspots, coronal loops, fibrils, etc., are ideal environments for the propagation of guided waves. MHD waves are natural manifestations of disturbances in solar plasmas when deviations in the equilibrium state of the plasma are paired with various restoring forces that tend to restore the equilibrium state. In a magnetic fluid (plasma) there is a much richer spectrum of waves compared to ordinary fluids and these waves are strongly anisotropic with respect to the direction of the magnetic field.

Observations in almost every wavelength of the last few decades confirm that the solar atmosphere is filled with MHD waves. Observations of MHD waves are commonly used in solar magnetoseismology to determine plasma

and field properties that are typically difficult to measure in the solar atmosphere (ionisation degree, gravitational scale−height, sub−resolution structuring, magnetic field strength, heating/cooling functions, etc.). When waves dissipate their energy over short length−scales, they also contribute to the total energy balance of the solar atmosphere, providing an additional heating that could compensate for radiative losses.

The solar atmosphere is a highly non-uniform and dynamic environment. Inhomogeneities are known to significantly influence the eigenfunctions and eigenvalues associated with waves. That is why, for an accurate diagnostic of the waves' properties one needs a realistic approach towards modelling. Very often this modelling can be carried out only numerically, as a mathematical (analytical) approach would be far too complicated and the complexity of analytical results would obscure the physical meaning. A correct and accurate knowledge of wave parameters would help carrying out a proper seismological diagnostics. For example, theoretical descriptions of waves are very sensitive to the way plasmas density is distributed; current models assume a homogeneous equilibrium density distribution in magnetic waveguides, such as sunspots. For an improved modelling one needs to understand the modifications in wave properties in realistic waveguides, where the plasma shows a transversal variation of its properties.

In the solar atmosphere the magnetic field tends to accumulate into various structures of different size due to the non-uniformity of the solar plasma (e.g. sunspots, spicules, prominences, coronal loops, etc.). These structures play an important role as observations show that waves predominantly propagate along them, being guided by the magnetic field. Therefore, an accurate diagnostics of the properties of waves in the solar atmosphere needs (as a first step) the analysis of waves along different waveguides.

The present Thesis is structured as follows: in Chapter 2, we provide the theoretical background framework on which the research carried out is based. Here, I briefly describe the mathematical framework that stays at the core of description of MHD waves. Next, I provide a review of the way dispersion relations are obtained and the properties of waves based on solving the derived dispersion relations. Dispersion relations for guided waves will be derived in various geometries, relevant to the content of the Thesis (magnetic slab, and magnetic cylinders) based on earlier studies by Edwin and Roberts (1982*a*,

1983*b*, 1982*b*). We also construct the corresponding dispersion diagrams, as numerical solutions of the dispersion relations for different situations.

Chapter 3 contains a description of the mathematical framework necessary to describe the morphology of MHD waves in an inhomogeneous waveguide which can be derived from the full set of ideal and linearised MHD equations. The equation solved in this Thesis is a Helmholtz-type partial differential equation with Dirichlet boundary condition describing the properties of slow body waves, i.e. waves that are oscillatory inside the waveguide and produce very little disturbance at the boundary. This Chapter is devoted to the investigations of the propagation characteristics and the spatial structure of slow body MHD eigenmodes in a magnetic flux tube with circular cross section with inhomogeneous equilibrium density distribution under solar photospheric conditions in the short and long wavelength limit. The equilibrium density profile inhomogeneity is represented by a local circular density enhancement or depletion whose strength, size and position can change. For analytical progress we will assume that the model has constant plasma-β and the equilibrium pressure is homogeneous. The numerical task will addressed by using the Fourier-Chebyshev Spectral method (FCS) that is employed to solve the governing equation (as a quadratic eigenvalue problem) in circular coordinate systems. The numerical solutions will provide the radial and azimuthal variation of eigenfunctions. The inhomogeneous transverse equilibrium density profile results in modified eigenvalues and eigenvectors. We carry out a parametric analysis to determine the importance of the physical parameters on the dimensionless phase speed of slow body modes corresponding to the spatial structure of the total pressure perturbation under photospheric conditions. The presented model can be considered a first attempt to study theoretically the properties of slow magnetoacoustic body waves in magnetic flux tubes with local density inhomogeneities. A similar investigation is carried out for long wavelength limits, i.e. when the wavelength of waves is larger than the radius of the waveguide.

In Chapter 4 we extend the model used in Chapter 3, by considering not only the equilibrium density as function of coordinates, but also equilibrium pressure and magnetic field, in line with observations and numerical modelling. Analytical progress will be made by considering that the plasma pressure and density vary following the same dependency on coordinates, meaning that we are dealing with a constant sound speed, i.e. isothermal equilibrium. The

profile of the equilibrium density inhomogeneity is represented by a local circular density enhancement or depletion whose strength, size and position can change. It is important to note that a decrease in the magnetic field would result from an increase in density or pressure since the equilibrium total pressure perturbation must be conserved. We derive a Helmholtz-like governing equation and solutions will be obtained numerically by imposing Dirichlet boundary condition at the boundary of the waveguide. We are going to determine the eigenvalues and eigenvectors appearing in the governing equation and we will treat this equation as a Sturm-Liouville problem. The governing equation will be solved using the Galerkin FEM method. Since we are dealing with a short wavelength limit, all dimensionless phase speeds are converging to one, i.e. the constant sound speed. As we expect that the inhomogeneities will affect the higher order modes more, we are displaying the results of these modes, in addition to the three modes analysed in Chapter 3 to provide a clearer picture of the impact of the considered inhomogeneities.

The results presented in the previous two chapters serve as motivation for the research included in Chapter 5, where we extend our analysis to consider the effect of multi-stranded inhomogeneities in density and magnetic field on the spatial structure of slow body modes in a circular waveguide. The analysis is conducted assuming an isothermal equilibrium, where the equilibrium pressures and densities have the same coordinate dependency as the model included in Chapter 4. The system of multi-stranded inhomogeneity can be a very good approximation to the umbral dots that appear in the umbral regions of sunspots. We investigated the spatial structure of waves when the inhomogeneities present themselves as enhancements or depletions. The effect of multi-stranded inhomogeneity will be investigated taking into account higher order modes, as these will likely be more affected by the irregularities in the equilibrium density and magnetic field.

Finally, Chapter 6 presents our conclusions and drafts several possible avenues along which the present research can be carried forward.

CHAPTER 2

Theoretical background: MHD equations and MHD waves in magnetic waveguides

The solar atmosphere is an intriguing and difficult environment of study due to the complexity of plasma behaviour and the interplay between flows and magnetic fields. The evolution, dynamics and stability of the plasma can be studied within the framework of MHD that combines well-known conservation equations from fluid mechanics (mass, momentum, energy) and the Maxwell equations that represent the evolution and coupling of electromagnetic fields. The resulting equations describe the interaction between the plasma and magnetic field.

Plasma is defined as a quasi-neutral gas consisting of charged particles sharing a collective behavior. The plasma dynamics largely depend on the electric and magnetic field developed inside it and its response to the externally applied fields.

In the classical sense, MHD describes changes in the characteristics of plasmas that occur of times much longer than atomic or kinetic processes that take place in this environment (e.g. collisions between particles), therefore one can say that the MHD framework describes slow processes. In addition, the length scales involved in MHD are much longer than the lengths involved in collisional processes, the mean free path of particles, therefore we are interested in changes in the plasma that occur over long length scales (very useful for solar physics). These descriptions impose applicability criteria on MHD that will be discussed in this Chapter together with the system of equations that is used to describe the dynamical and thermodynamic state of the plasma and the possible wave solutions of the MHD system that form the scope of my research. The plasma we are going to study will be considered as being treated as a single, perfectly conducting ideal fluid made up from positive ions and

electrons that are strongly coupled through long-range collisions.

Although MHD is not the most general description of a plasma, it has been successfully used to explain a very large number of phenomena in the solar atmosphere, including the waves and oscillations observed by various high-resolution ground and space-based telescopes. MHD is considered to belong to the "classical" physical formalism, meaning that quantum and relativistic effects are neglected (speeds are usually very small compared with the speed of light). In addition, MHD assumes that particles are in thermodynamic equilibrium and the displacement current is neglected in the Maxwell equations.

One type of solution the MHD system of equations can describe well is the solution whose form is assumed to vary periodically in space and time, i.e. waves that constitute the topic of the present Thesis. This Chapter is dedicated to the analysis of the nature and properties of waves in a plasma, and the modification in the properties of waves when these propagate in a geometrically well-defined magnetic waveguide.

2.1 The system of MHD equations

In spite of all the simplifications made, the MHD system of equations is still very complex because it contains a number of coupled non-linear partial differential equations. To obtain analytical solutions, a number of other assumptions have to be made. In the present Thesis we are going to employ two more simplifications. The first one assumes motions always such that the speeds are much larger than the thermal speed of particles and length scales are much larger than the scales over which transport mechanisms (viscosity, resistivity, thermal conduction, etc.) operate. As a result, dissipative terms will be neglected, so we are dealing with the system of ideal MHD. Secondly, we will consider small amplitude changes in the magnitude of physical variables that leads to a simplified linear approach of perturbations. Finally, we assume that the length scales involved in our problem are much smaller than the gravitational scale-heights, meaning that gravitational effects can be neglected.

The ideal MHD equations describe conservation laws of mass, momentum, energy and magnetic flux. These equations are given in terms of density, ρ, pressure, p, velocity vector $\mathbf{v}$ and magnetic field $\mathbf{B}$ as

$$\frac{D\rho}{Dt} + \rho\nabla \cdot \mathbf{v} = 0, \tag{2.1}$$

$$\rho\frac{D\mathbf{v}}{Dt} = -\nabla p + \frac{1}{\mu_0}(\nabla \times \mathbf{B}) \times \mathbf{B}, \tag{2.2}$$

$$\frac{D}{Dt}\left(p\rho^{-\gamma}\right) = 0, \tag{2.3}$$

$$\frac{\partial \mathbf{B}}{\partial t} = \nabla \times (\mathbf{v} \times \mathbf{B}), \tag{2.4}$$

$$\nabla \cdot \mathbf{B} = 0. \tag{2.5}$$

where $D/Dt = \partial/\partial t + \mathbf{v} \cdot \nabla$ is the material derivative, μ_0 is the magnetic permeability of free space, and γ is the adiabatic index. These equations express the conservation of mass (Eq. 2.1), conservation of momentum (Eq. 2.2), the adiabatic energy conservation law (Eq. 2.3), the induction equation (Eq. 2.4) and the Gauss' law (Eq. 2.5).

Given the density, ρ, kinetic pressure, p, temperature, T, of the plasma can be calculated using the equation of state for an ideal gas. In a pure plasma made up of hydrogen, for example, this equation is given by

$$p = 2\frac{k_B}{m_p}\rho T,$$

where m_p is the mass of the proton and k_B is the Boltzmann constant.

Basically Eq. (2.2) is nothing more than Newton's second law and describes the balance of forces that act upon the plasma element of unit volume. The right-hand side of this equation contains two forces that act upon a plasma element of unit volume. First, there is a pressure gradient force ($-\nabla p$) and there is a magnetic force, called the Lorentz force, that is oriented perpendicular to the magnetic field. The Lorentz force can be rearranged as

$$\frac{1}{\mu_0}(\nabla \times \mathbf{B}) \times \mathbf{B} = (\mathbf{B} \cdot \nabla)\frac{\mathbf{B}}{\mu_0} - \nabla\left(\frac{B^2}{2\mu_0}\right). \tag{2.6}$$

The first term of the RHS in this equation represents the effect of a tension parallel to the magnetic field and the second the gradient of a scalar magnetic pressure. The Lorentz force has, therefore, two effects on the plasma: to compress it through the magnetic pressure term and also to shorten magnetic field lines through the tension force, which represents the effect of a tension parallel to $\mathbf{B}$ which appears whenever magnetic field lines are curved.

Using the above decomposition, Eq. (2.2) is often rearranged as

$$\rho \frac{D\mathbf{v}}{Dt} = -\nabla P_T + (\mathbf{B} \cdot \nabla)\frac{\mathbf{B}}{\mu_0}, \tag{2.7}$$

where the quantity

$$P_T = p + \frac{B^2}{2\mu_0}, \tag{2.8}$$

is the total pressure. This quantity will play a key role in the mathematical framework of the present Thesis.

The set of ideal MHD equations (2.1)-(2.5) contains highly nonlinear terms and mathematical progress can be achieved in the so-called *linear approximation*. In this approach each physical quantity is expressed as the sum of the background (equilibrium) value denoted by the index 0, and its perturbation, denoted by the index 1, i.e. $\rho_0 + \rho_1$, etc. We will assume that the perturbations are just small changes of equilibrium quantities, therefore, every term consisting of the product of two perturbations becomes negligibly small. The equilibrium state will be considered to be static ($\mathbf{v}_0 = 0$), stationary (the equilibrium quantities are independent of time), and homogeneous (the equilibrium quantities are independent on the spatial scales). As a consequence, the linearised version of the MHD equations becomes

$$\frac{\partial \rho_1}{\partial t} + \rho_0 \nabla \cdot \mathbf{v}_1 = 0, \tag{2.9}$$

$$\rho_0 \frac{\partial \mathbf{v}_1}{\partial t} = -\nabla p_1 + \frac{1}{\mu_0}(\nabla \times \mathbf{B}_1) \times \mathbf{B}_0, \tag{2.10}$$

$$\frac{\partial p_1}{\partial t} - C_S^2 \frac{\partial \rho_1}{\partial t} = 0, \tag{2.11}$$

$$\frac{\partial \mathbf{B}_1}{\partial t} = \nabla \times (\mathbf{v}_1 \times \mathbf{B}_0), \tag{2.12}$$

$$\nabla \cdot \mathbf{B}_1 = 0, \tag{2.13}$$

where $C_S^2 = \gamma p_0/\rho_0$ is the square of the constant adiabatic sound speed.

A very important parameter that can help reducing the complexity of the above equations and determine the dominant forces driving the dynamics of the plasma is the so-called plasma-β parameter defined as the ratio of the kinetic and magnetic pressure, i.e. $\beta = 2\mu_0 p_0/B_0^2$. A general expression of this

parameter can be given as (Priest, 2014*a*)

$$\beta = 3.5 \times 10^{-21} nTB^{-2},$$

where n is the number density of the plasma (in m^{-3}), T is temperature (measured in K) and B is the magnetic field (given in G).

If $\beta > 1$, the dynamics is driven mainly by kinetic forces (e.g. pressure gradient). In the opposite case, $\beta < 1$, the dynamics is driven predominantly by magnetic forces, e.g. the Lorentz force. Traditionally the regions in the solar photosphere and lower chromosphere far away from active regions are characterised by $\beta > 1$, while active regions in the lower part of the atmosphere, the upper chromosphere, solar corona and solar wind correspond to $\beta < 1$.

One important consequence of Eq. (2.12) is the Alfvén's frozen flux theorem. For a perfectly conductive fluid (as used here) the field lines are frozen into the fluid, that is the magnetic field moves along with the flow of the plasma. A common way to explain the frozen flux theorem is to use magnetic flux tubes and magnetic field lines. A magnetic flux tube is a region of space that resembles a tube or cylinder and has sides that are entirely parallel to the magnetic field (i.e. tangential discontinuity). As a result, there is no magnetic flux through these sides, and the magnetic flux is constant and equal over the whole length of the tube. Alfvén's theorem implies that these surfaces of constant flux move with the fluid they are embedded in. Magnetic flux tubes are consequently solidified within the fluid.

2.2 MHD waves

High resolution ground and space observations of the last few decades confirmed that the solar atmosphere is filled with MHD waves seen almost in every wavelength (Mathioudakis et al., 2013; Jess et al., 2015; Li et al., 2020; Banerjee et al., 2021; Jess et al., 2022, to name but a few). Waves are natural manifestations of disturbances in the solar plasma when deviations in the equilibrium state of the plasma are paired with various restoring forces that tend to restore the equilibrium state. MHD waves have been extensively studied in connection to plasma heating or acceleration (see, e.g. Erdélyi and Ballai (2007), De Moortel and Browning (2015), Van Doorsselaere et al. (2020), Li et al. (2022) and references therein), and as a diagnostic tool using magneto-

seismological techniques that aim to determine the plasma and field parameters that cannot be measured directly or indirectly (for a few reviews see, e,g. Nakariakov et al. (1999); Ballester (2005); Verth (2007); Ballai (2007); Oliver (2009); De Moortel and Nakariakov (2012); Griffiths et al. (2023); Zheng et al. (2023); Chen et al. (2023).

Waves are essential tools to describe and understand the dynamics in the solar atmosphere. An MHD wave can be seen as a harmonic response to the interaction between electrically conducting fluids (plasmas) and magnetic fields. MHD waves are ubiquitous in the solar atmosphere, and contribute to the heating of the solar atmosphere by transporting mechanical energy from the photosphere into the solar corona, where these waves are dissipated. Waves can also transport information about the medium in which they propagate, therefore they can be used as tools to diagnose the plasma using seismological techniques.

The solar magnetic field tends to accumulate into structures of different strength and cross section. Manifestations of such structuring are continuously observed in the solar atmosphere (e.g. sunspots, spicules, prominences, coronal loops, etc.). These structures play an important role in the process of wave propagation, because waves are predominantly propagating along these structures, making them guided and dispersive. At the same time, waves act as tracers of the magnetic field along which they propagate.

The characteristics of MHD waves are studied by using dispersion relations (i.e. relations that describe the relationship between the frequency of waves, ω, and their wavevector, $\mathbf{k}$) and the associated dispersion diagrams. In contrast to hydrodynamics, plasmas can support a much richer spectrum of waves. The nature of the restoring force acting to restore any deviation from equilibrium will determine the nature and characteristics of waves. For instance, Alfvén waves are the results of changes opposed by the magnetic tension. Magneto-acoustic waves are produced when plasma pressure and magnetic pressure act in conjunction to oppose changes in the dynamics of the plasma. If plasma pressure and magnetic pressure act against each other (out of phase), slow magneto-acoustic waves are produced. On the other hand, when these two restoring forces act in phase, disturbances will propagate as fast magnetoacoustic waves.

The properties of the above propagating in an unbounded and structured plasma environment will be discussed in more detail in the following sections.

2.2.1 Dispersion relation of MHD waves in unbounded homogeneous medium

The simplest approach to investigate the nature and properties of waves supported by a plasma is to focus our attention on the propagation of these waves in the idealistic situation of an unbounded plasma, i.e. when we do not impose restrictions on the spatial extent of the plasma or its structuring. We consider an unbounded plasma environment where the plasma and field parameters are constant. As we would like to concentrate on the fundamental properties of waves, we are going to consider that the plasma is ideal (no transport mechanisms are included), wavelengths are much longer than the characteristic lengths of stratification (gravitational forces are excluded), and changes in the plasma occur adiabatically. We assume a homogeneous magnetic field of the form $B_0\hat{z}$, where $\hat{z}$ is the unit vector in the z direction. The wave that propagates in this environment will be described by the 2-dimensional propagation vector $\mathbf{k} = (k_x, 0, k_z)$ in the $x - z$ plane. The nature and properties of MHD wave propagation in such plasma has been examined previously and analysed by many authors (e.g. Lighthill, 1960; Cowling, 1976; Goedbloed et al., 2004; Priest, 2014*b*). The system of ideal and linearised MHD equations (2.9)–(2.13) can be reduced to a single partial differential equation (Roberts, 1981*a*) that describes spatial and temporal evolution of the velocity divergence in the form

$$\frac{\partial^4 \triangle}{\partial t^4} - \left(C_S^2 + V_A^2\right) \frac{\partial^2}{\partial t^2} \nabla^2 \triangle + C_S^2 V_A^2 \frac{\partial^2}{\partial z^2} \nabla^2 \triangle = 0, \tag{2.14}$$

where $V_A = B_0/\sqrt{\mu_0 \rho_0}$ is the Alfvén speed and $\triangle = \nabla \cdot \mathbf{V}_1$ is the divergence of $\mathbf{V}_1$, or the compressibility of the plasma. In order to obtain a dispersion relation, we Fourier analyse Eq. (2.14) by considering

$$\triangle = \hat{\triangle}(x) \exp^{i(k_y y + k_z z - \omega t)}, \tag{2.15}$$

where $\hat{\triangle}(x)$ is the x-dependent amplitude of perturbations and ω is the frequency of waves. Writing the perturbations in this way is equivalent to replacing $\partial/\partial t$ by $-i\omega$ and the ∇ operator with $i\mathbf{k}$. If the perturbed velocity is perpendicular to the wave vector ($\nabla \cdot \mathbf{V}_1 = 0$) or $\mathbf{k} \cdot \mathbf{V}_1 = 0$, we have incompressible plasma and the only wave that propagates is the Alfvén wave whose dispersion relation is written as $\omega = \pm k V_A \cos\theta$, where θ is the angle

between the direction of wave propagation and the direction of the equilibrium magnetic field, i.e. $k_z = k\cos\theta$. Alfvén waves are transverse, purely magnetic waves that do not perturb density or pressure of the plasma. In a compressible plasma ($\mathbf{k}\cdot\mathbf{V}_1 \neq 0$), we can substitute Eq. (2.15) into (2.14) resulting in the dispersion relation of fast and slow magneto-acoustic waves of the form

$$\omega^4 - k^2\left(C_S^2 + V_A^2\right)\omega^2 + k_z^2 C_S^2 k^2 V_A^2 \ = 0. \tag{2.16}$$

The solution of this bi-quadratic equation has two unique solutions that corresponds to slow and fast wave propagating in opposite direction as follows

$$\omega^2 = \frac{k^2}{2}\left(C_S^2 + V_A^2\right) \pm \frac{k^2}{2}\sqrt{\left(C_S^2 + V_A^2\right)^2 - 4\frac{{k_z}^2 C_S^2 V_A^2}{k^2}}, \tag{2.17}$$

where the $\pm$ sign denotes the fast (upper sign) and slow (lower sign) magnetoacoustic modes. A more complete picture on the properties of magnetoacoustic modes can be obtained after introducing the phase and group speeds defined as $V_{ph} = \frac{\omega}{k}$ and $V_{gr} = \frac{d\omega}{k}$. After dividing equation (2.16) by k^4 we can write the dispersion relation to

$$V_{ph}^4 - V_{ph}^2\left(C_S^2 + V_A^2\right) + C_S^2 V_A^2\cos^2\theta = 0. \tag{2.18}$$

The solutions of the above equation can be best visualised in a polar diagram (also called Friedrich diagram). We consider that the equilibrium magnetic field is along the vertical axis, while the direction of propagation can vary with respect to this direction. The polar plot for the V_{ph} described by Eq. (2.18), as a function of θ is shown in Fig. (2.1) for three different values of the plasma-β parameter.

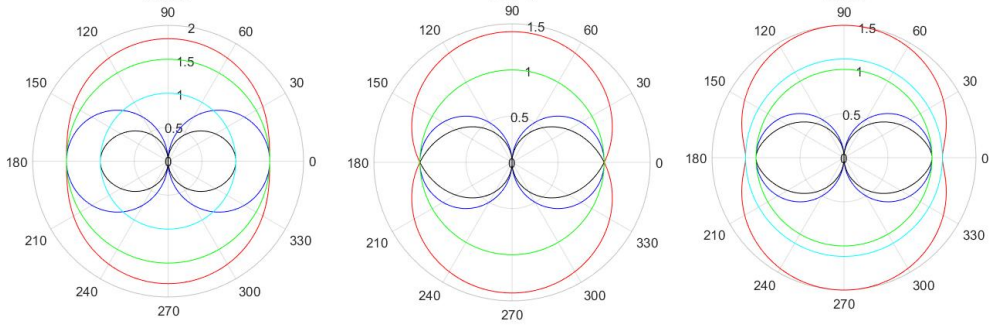

Figure 2.1: The Friedrich diagram showing the variation of the phase speeds, V_{ph} with respect to the propagation direction, for Alfvén, slow and fast magnetoacoustic waves (blue, black and red curves, respectively) in an unbounded homogeneous medium. The three panels correspond to the cases $\beta < 1$ (left panel), $\beta = 1$ (middle panel) and $\beta > 1$ (right panel). The values of the characteristic Alfvén and sound speeds are given in units of the sound speed for references.

The three panels of Fig. (2.1) display the variation in the phase speed of Alfvén, slow and fast magnetoacoustic waves with respect to the angle between the ambient magnetic field and the direction of wave propagation, when $\beta < 1$ (left panel), $\beta = 1$ (middle panel), and $\beta > 1$ (right panel). In each case, it is clear that slow and Alfvén waves cannot propagate in the perpendicular direction to the ambient magnetic field. Fast waves can propagate across the field, when they attain their maximum phase speeds $(V_A^2 + C_S^2)^{1/2}$. The same fast magnetoacoustic waves move at a speed close to the sound speed when they propagate in the same direction as the ambient field for $\beta \gg 1$, or the Alfvén speed for $\beta \ll 1$. For the slow mode, the phase speed ranges from $0 \ll V_{ph} \ll \min(C_S, V_A)$, while for the fast mode, the phase velocity ranges from $\max(C_S, V_A) \ll V_{ph} \ll (C_S^2 + V_A^2))^{1/2}$.

In reality, the plasma is neither unbounded nor homogeneous, therefore, it is natural to consider in what follows the situation where the plasma exhibits some sort of inhomogeneity via the simplest configuration represented by sharp interfaces separating homogeneous plasma regions. Inspired from results obtained for surface waves propagating in fluids, we expect that discontinuities will support the propagation of guided waves. The surface of discontinuity will separate two regions of different properties and in each of these regions the MHD equations will be solved. The properties of possible waves will be studied with the help of the dispersion relations that are obtained after matching the solutions of ideal and linearised MHD equations for the two regions

separated by the interface. This matching is obtained by imposing the dynamic and kinematic boundary conditions. In the case of a magnetic field parallel to the interface (tangential discontinuity), these conditions correspond to the continuity of the total pressure and the transversal component of the velocity perturbation. At the same time, since we aim to study waves propagating along the discontinuities we also require that far away from the location of these discontinuities the waves' amplitude vanishes, i.e. waves are evanescent.

2.2.2 MHD Waves in structured plasmas

The magnetic field in the solar atmosphere provides the ideal and natural structured environment for plasma and this structuring of the solar plasma is continuously observed in every wavelength. In reality one can expect that physical parameters that describe the state of the plasma are changing in every direction, however for the sake of modelling we would need to restrict our attention to a few cases that could highlight the properties of waves in structured and inhomogeneous plasmas. The cases we are going to survey ensure that analytical progress is made whose results allow us to determine the nature and properties of waves.

Let us consider a unidirectional magnetic field oriented in the z direction in the form $\mathbf{B}_0 = B_0\hat{z}$ in a Cartesian coordinate system. The equilibrium gas pressure, ρ_0, pressure p_0 and field magnitude B_0 may all vary in the direction perpendicular to the field. The effects of gravitational stratification are neglected. The condition of pressure balance requires that the total pressure perturbation is constant and in the equilibrium state this balance of forces can be written as

$$\frac{d}{dx}\left(p_0 + \frac{B_0^2}{2\mu_0}\right) = 0.$$

After linearising the MHD equations, we can split the velocity field into components parallel (z) and perpendicular ($\perp$) to the ambient magnetic field. The evolution of these velocity components are given by

$$\rho_0\left(\frac{\partial^2}{\partial t^2} - V_A^2\frac{\partial^2}{\partial z^2}\right)v_\perp + \nabla_\perp\left(\frac{\partial P_T}{\partial t}\right) = 0, \tag{2.19}$$

$$\rho_0\left(\frac{\partial^2}{\partial t^2} - C_T^2\frac{\partial^2}{\partial z^2}\right)v_z + \frac{C_S^2}{C_f^2}\frac{\partial}{\partial z}\left(\frac{\partial P_T}{\partial t}\right) = 0. \tag{2.20}$$

The temporal variation of the total pressure can be written as

$$\frac{\partial P_T}{\partial t} = \rho_0 V_A^2 \frac{\partial v_z}{\partial z} - \rho_0 C_f^2 \nabla \cdot \mathbf{v},$$

where $C_f^2 = C_S^2 + V_A^2$ and $\nabla_\perp$ denotes the component of the gradient operator perpendicular to the direction of the ambient magnetic field, i.e. perpendicular to the z-axis. Note that all characteristic speeds are functions of the x coordinate.

Considering that all perturbations are written in a spatial dependence of the form given by Eq. (2.15) allows us to combine Eqs. (2.19) and (2.20) into a single ordinary differential equation of the form (Roberts, 1981*b*)

$$\frac{d}{dx}\left\{\frac{\rho_0(x)(k_z^2 C_A^2(x) - \omega^2)}{m^2(x) + k_y^2}\frac{dv_x}{dx}\right\} = \rho_0(x)(k_z^2 V_A^2(x) - \omega^2)v_x, \tag{2.21}$$

where the quantity m^2 is defined as (often labelled as the *magnetoacoustic parameter*)

$$m^2(x) = \frac{(k_z^2 C_S^2(x) - \omega^2)(k_z^2 V_A^2(x) - \omega^2)}{(C_S^2(x) + V_A^2(x))(k_z^2 C_T^2(x) - \omega^2)}. \tag{2.22}$$

The last quantity plays a very important role in the classification of waves and, depending on the relative magnitude of the characteristic speeds, it can be a positive or negative quantity. In general, an analytical solution to Eq. (2.21) can be obtained only in some rather specific cases that correspond to specific inhomogeneities. One such special configuration is when the inhomogeneous character of the plasma is represented by sudden changes in the properties of the plasma, i.e. when we deal with changes of properties at an interface separating two, otherwise homogeneous, plasma regions. In this case the equations written for both regions become second order differential equations with constant coefficients. The requirement we have to impose to ensure that waves remain attached to the interface surface separating the two regions, is that far away from the interface waves are evanescent, i.e. $v_x(x \to \pm\infty) = 0$. The schematic profile of waves propagating at the interface can be seen in the first panel of Fig. (2.3). The properties of MHD waves propagating in such structured plasmas were first studied in great detail by Roberts (1981*b*). We are not going to detail the results obtained in the case of a single interface, however the ideas presented above will constitute the starting point in presenting the results obtained for wave propagation in magnetic configurations much more

relevant for the present Thesis.

2.2.2.1 Dispersion relation of MHD waves in magnetic slabs

A natural extension of the problem of waves at a single interface is the consideration of two magnetic interfaces that are parallel to the z-axis and are spaced apart by a constant distance, $2x_0$ forming a waveguide. Although a Cartesian geometry is not very realistic to describe waves in solar magnetic structures, it allows us a much simpler understanding of waves' properties that will be similar when we consider more realistic configurations. Describing the wave propagation in a Cartesian coordinate system also allows us to obtain dispersion relations in terms of functions that are relatively easy to handle.

The problem of waves in magnetic slabs has been extensively studied in the past. Parker (1974) described the appearance of surface waves for an incompressible medium in an isolated magnetic slab with no magnetic field surrounding the slab. Later, Roberts (1981*c*) studied the wave propagation for an isolated magnetic slab in a compressible medium. This model was extended by Edwin and Roberts (1982*a*) who investigated the effect of a magnetic field surrounding the slab by expanding the study by Roberts (1981*c*). These pioneering theoretical results were followed by a myriad of further studies that involved either observational evidence that was combined with theory, or extra additions to the original models such as flows, multi-layer slabs, etc. (Zsámberger et al., 2022; Markwick et al., 2024; Briard et al., 2024).

Let us consider the two semi-infinite plasma surfaces forming a slab infinitely extended in the y and z directions. These interfaces delimit an internal and external plasma region labelled by indices 0 and e, respectively. The sound and Alfvén speeds in the two regions are C_0, C_e, V_{A0}, and V_{Ae}. We consider the case of parallel propagation with negligible modification of the wave in the y direction ($\partial/\partial y = 0$) and the motion of the plasma is two-dimensional, i.e. $\mathbf{v} = (v_x, 0, v_z)$.

The uniform magnetic field (internal ($B_0\hat{z}$) and external ($B_e\hat{z}$)) is parallel to the interfaces making them a tangential discontinuity. The solutions of MHD equations inside and outside the slab are matched at the boundary of the regions by imposing the kinematic and dynamic boundary conditions, i.e. we impose the continuity of the transversal component of velocity (v_x), and the total pressure, P_T, at the boundaries situated at $x = \pm x_0$. Waves are assumed

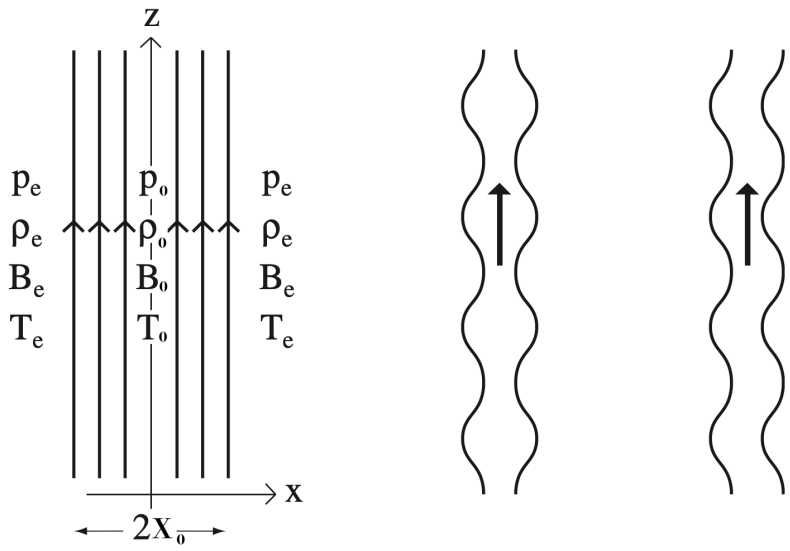

Figure 2.2: A sketch of a uniform magnetic slab of width $2x_0$, embedded in a uniform medium (left panel). The middle and right panels display schematically the form of sausage and the kink modes, respectively. Credit: Priest (2014*b*).

to propagate along the interface and be evanescent far from the waveguide. A schematic representation of the geometry used in this discussion together with the relevant physical parameters is shown in the left panel of Fig. (2.2).

The MHD equations can be reduced in both regions (inside and outside the slab) to a system similar to Eqs. (2.19)-(2.20), with constant characteristic speeds specific for each region. These equations can be reduced in each region to a second order ordinary differential equation for the component of the velocity that is normal to the interface separating the regions of the form

$$\frac{d^2 v_x}{dx^2} - m_0^2 v_x = 0, \quad x < |x_0|, \tag{2.23}$$

where the magnetoacoustic parameter m_0 was defined earlier by Eq. (2.22). A similar magnetoacoustic parameter can be obtained in the external region and will be denoted by m_e for $x > |x_0|$. As waves are assumed to be evanescent outside the slab, we require that $v_x \to 0$ as $x \to \pm\infty$. This condition translates in the requirement that $m_e^2 > 0$, so the amplitude of waves decays exponentially with distance. This condition implies that the frequency of waves must satisfy

the conditions

$$\frac{\omega}{k} < C_{Te}, \quad \text{or} \quad \min(C_{0e}, V_{Ae}) < \frac{\omega}{k} < \max(C_{0e}, V_{Ae})$$

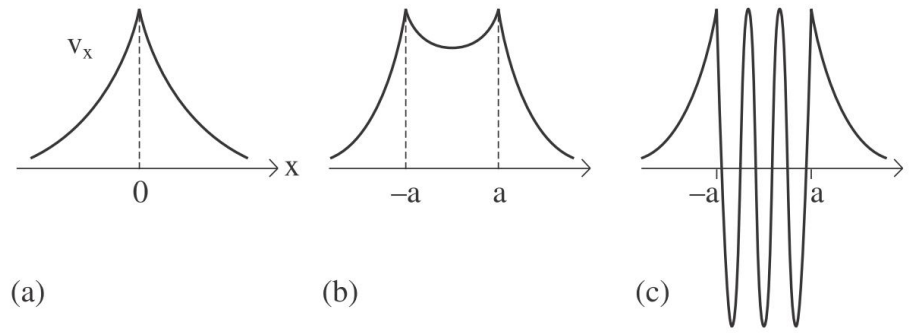

Figure 2.3: Schematic diagram of surface wave along an interface (a), magnetic slab (or flux tube) (b) and body waves propagating in a magnetic slab (or flux tube) (c). Here the boundaries of the waveguide are situated at $\pm a$.

After some straightforward calculations we obtain that the dispersion relation of MHD waves propagating along the magnetic slab waves is given by

$$\rho_0 \left(k^2 V_A^2 - \omega^2\right) m_{0e} + \rho_e \left(k^2 V_{Ae}^2 - \omega^2\right) m_{0i} \begin{pmatrix} \tanh \\ \coth \end{pmatrix} m_{0i} x_0 = 0, \qquad (2.24)$$

where the tanh / coth solutions describe the symmetrical and anti-symmetrical modes.

It is probably appropriate at this stage to define the terminology which is used here in the classification of modes of Eq. (2.24) and throughout this Thesis. Following Roberts (1981*a*), solutions of Eq. (2.24) with $m_0^2 > 0$ will be referred to as surface waves and those with $m_0^2 < 0$ as body waves (see the middle and right panels of Fig. 2.3). Thus the distinction pertains only to their spatial behaviour within the inhomogeneity. Surface waves have their maximum amplitude at the boundary of the waveguide and show an evanescent behaviour inside the slab (see the middle panel of Fig. 2.3), and body waves have an oscillatory behaviour inside the slab (see right panel of Fig. 2.3) and attain their minimum amplitude at the interface. Based on the form of the magnetoacoustic parameter, it is clear that surface waves will propagate as long as (for waves propagating in the positive direction, i.e. in the direction of

the background magnetic field)

$$\frac{\omega}{k} < C_T, \quad \text{or} \quad \min(C_0, V_A) < \frac{\omega}{k} < \max(C_0, V_A).$$

When waves have their phase speed that satisfies the first condition, they will be slow surface waves, while for the second condition, we have fast surface waves. In addition, body waves will propagate in a magnetic structure provided

$$C_T < \frac{\omega}{k} < \min(C_0, V_A) \quad \text{or} \quad \frac{\omega}{k} > \max(C_0, V_A).$$

Body waves propagating in the first domain will be the slow body waves, while fast waves will propagate in the second domain.

A further categorisation of modes arises from the consideration of oscillation symmetries of the interfaces forming the boundaries of the slab. Waves can oscillate such that the boundaries oscillate in phase (these modes are called the kink modes and correspond to the *coth* solution of Eq. 2.24). When boundaries oscillate in anti-phase, waves will be labelled as sausage modes and these are the modes given by the *tanh* solution of Eq. (2.24). The symmetry axis of the slab is oscillating the same way as the boundaries in the case of kink modes and does not have a motion in the case of sausage modes. A schematic representation of these two modes is shown by the middle and right panels of Fig. (2.2).

The full spectrum of solutions of the dispersion relation (2.24) are shown for photospheric ($V_{Ae} = 0.5C_0$, $C_e = 1.5C_0$ and $V_A = 2.0C_0$) and coronal conditions ($V_{Ae} = 5C_0$, $C_e = 0.5C_0$ and $V_A = 2.0C_0$) in Fig. 2.4. The two cases are distinguished by the ordering of phase speeds. Here we plot the phase speed of waves (ω/k) with respect to the dimensionless quantity kx_0 as in the study by Edwin and Roberts (1982*b*). In the solar photosphere, where $\beta \gg 1$, slow surface and body waves propagate with weak dispersion with speeds whose value is bounded by the internal sound and cusp speeds. In addition, fast surface sausage and kink modes propagate with speeds between the internal and external sound speeds and show a much more dispersive character than slow waves. In contrast, in the solar corona, where $\beta \ll 1$ no surface waves are able to propagate, and fast modes are very dispersive.

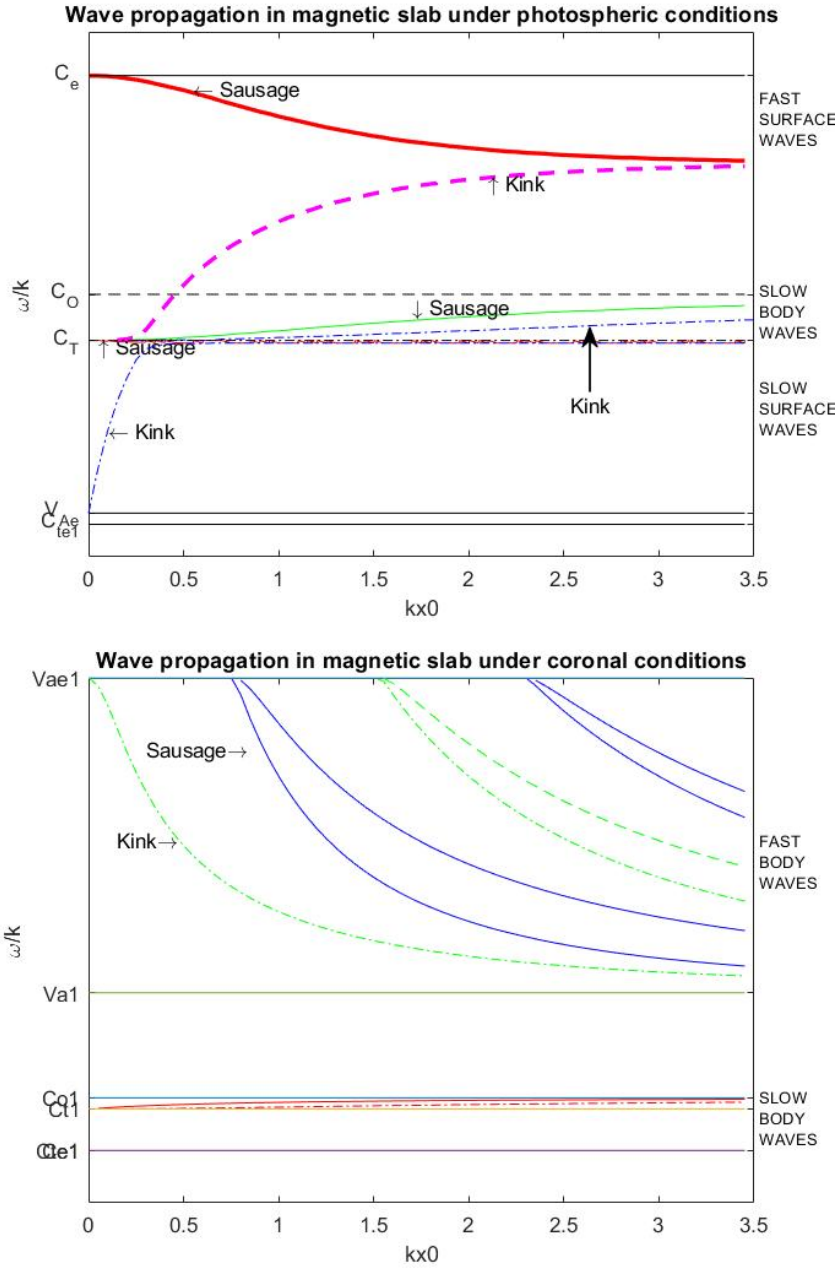

Figure 2.4: Dispersion curves of modes propagating along a magnetic slab under photospheric (top panel) and coronal conditions (bottom panel). Here the phase speed of waves (ω/k) is plotted with respect to the dimensionless quantity kx_0. Sausage and kink modes are represented by solid and dashed lines, respectively.

2.2.3 MHD waves in cylindrical magnetic flux tubes

In reality magnetic waveguides are not planar structures, instead their cross section often looks closer to the circle. The idea of using a Cartesian coordinate system to determine the properties of waves was very useful because it allows relatively simple mathematics, however for a more realistic description of possible waves and their nature, we would need to employ a geometry that allows the curvature of the boundary and the simplest case is the one when the waveguide is approximated by a cylindrical flux tube. A cylindrical geometry is the simplest geometry that still provides a high degree of symmetry. Here we closely follow the derivation of the dispersion relation and interpretation of solutions presented by the study by Edwin and Roberts (1983*c*). The study

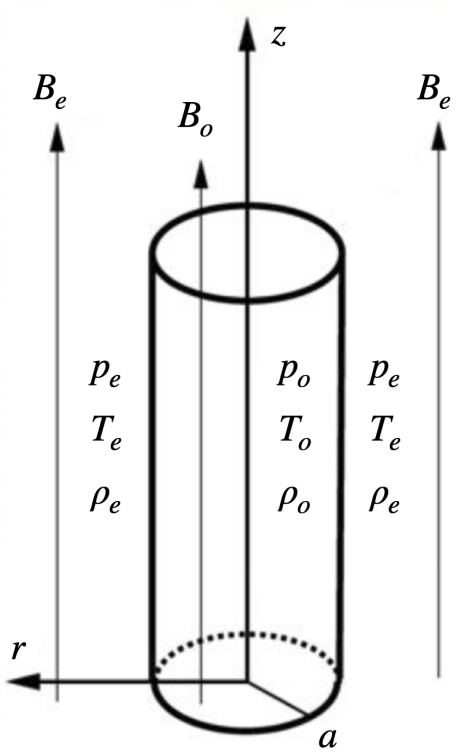

Figure 2.5: A schematic representation of a cylindrical magnetic flux tube with the associated physical quantities describing the plasma and magnetic field inside (index "0") and outside the flux tube. The flux tube has a constant radius a and it is oriented along the z axis.

of waves in a magnetic flux tube and the derivation of the dispersion relation of waves follow the same physical principles as in the case of waves in a magnetic slab, i.e. internal and external solutions have to be matched on the

boundary of the waveguide (done by imposing the continuity total pressure and radial velocity component). Similar to the previous cases, the waves will be localised to the waveguide in which they propagate, meaning that far away from the structure their amplitude decays exponentially. In addition to the magnetic slab case, here we impose that solutions are regular at $r = 0$, i.e. at the symmetry axis of the tube (this requirement has to be imposed to all models that have a central point of symmetry). Let us assume that a circular cross-section flux tube is permeated by a homogeneous straight magnetic field oriented along the longitudinal axis of the tube, $(B_0\hat{z})$ and it is embedded within an environment of uniform magnetic field $(B_e\hat{z})$, where $\hat{z}$ is the unit vector in the z direction, all variables inside the flux tube have index 0, while quantities outside the tube are denoted with index e. The equilibrium state is assumed to be homogeneous, static and stationary. The cylindrical geometry will be described by the coordinates r, θ, z. The MHD system of equations will be perturbed and we assume that the perturbations are small, therefore we can use the linearised version of this system. Perturbations can be Fourier analysed by considering them proportional to $\exp\big(i(\omega t + n\theta + kz)\big)$, where n, and k are the azimuthal and longitudinal wave numbers and ω is the (real) frequency of wave oscillations.

The linear perturbation about equilibrium configuration of variables in the MHD system of equations leads to Eq. (2.14), however now the Laplace operator in cylindrical geometry can be expressed as

$$\nabla^2 = \frac{\partial^2}{\partial r^2} + \frac{1}{r}\frac{\partial}{\partial r} + \frac{1}{r^2}\frac{\partial^2}{\partial \theta^2} + \frac{\partial^2}{\partial z^2}. \tag{2.25}$$

Similar to the magnetic slab case, we are going to consider that the compressibility, Δ, can be written as

$$\Delta = R(r)\exp(i(\omega t + n\theta + kz)), \tag{2.26}$$

where $R(r)$ denotes the amplitude of this quantity that can depend on the radial coordinate r. As a result, the governing equation for $R(r)$ can be written as

$$\frac{d^2R}{dr^2} + \frac{1}{r}\frac{dR}{dr} - \left(m_0^2 + \frac{n^2}{r^2}\right)R = 0, \tag{2.27}$$

which is a typical Bessel differential equation and

$$m_0^2 = -\frac{\left(\omega^2 - k^2 C_S^2\right)\left(\omega^2 - k^2 V_A^2\right)}{\left(C_S^2 + V_A^2\right)\left(\omega^2 - k^2 C_T^2\right)}. \tag{2.28}$$

Depending on the sign of m_0^2 (surface and body waves) this equation admits, as solution, the well-known Bessel functions, i.e. $c_1 I_n(m_0 r) + c_2 K_n(m_0 r)$ when $m_0^2 > 0$ and $c_1' J_n(m_0 r) + c_2' Y_n(m_0 r)$ when $m_0^2 < 0$. As we require that solutions are regular at $r = 0$, we choose $c_2 = c_2' = 0$. Here c_1, c_2, c_1', and c_2' are constants. By inserting Eq. (2.26) into Eqs. (2.1)-(2.5), the three components of the velocity perturbation in the cylindrical coordinate system can be explicitly expressed as (Spruit, 1982),

$$V_{ri} = A\frac{\omega^2 - k^2 C_S^2}{\omega^2 m_0^2}\frac{d}{dr}R_n, \quad V_{\theta i} = iA\frac{\omega^2 - k^2 C_S^2}{\omega^2 m_0^2}\frac{n}{r}R_n, \quad V_{zi} = -A\frac{ikC_S^2}{\omega^2}R_n, \tag{2.29}$$

where A denotes an arbitrary amplitude and R_n denotes a Bessel function of order n. In a similar way, for the external region the governing equation for $R(r)$ is obtained in a similar form as Eq. (2.27), but with m_e^2 replacing m_0^2. Since waves are expected to be evanescent in the external region, the characteristic Bessel function that will describe the variation of $R(r)$ will be proportional to $K_n(m_e r)$.

The dispersion relation is obtained by imposing the continuity of the radial component of velocity and total pressure at the boundary ($r = a$) of the magnetic flux tube. As a result, for the combination of characteristic speeds for by $m_0^2 > 0$, the dispersion relation for surface wave is given by (Edwin and Roberts, 1983*b*)

$$\rho_0(k^2 V_A^2 - \omega^2) m_e \frac{K_n^{'}(m_e a)}{K_n(m_e a)} = \rho_e(k^2 V_{Ae}^2 - \omega^2) m_0 \frac{I_n^{'}(m_0 a)}{I_n(m_0 a)}. \tag{2.30}$$

In contrast, when $m_0^2 = -n_0^2 < 0$, then the dispersion relation for body wave can be written as

$$\rho_0(k^2 V_A^2 - \omega^2) m_e \frac{K_n^{'}(m_e a)}{K_n(m_e a)} = \rho_e(k^2 V_{Ae}^2 - \omega^2) n_0 \frac{J_n^{'}(n_0 a)}{J_n(n_0 a)}, \tag{2.31}$$

where the dash denotes the derivatives of the Bessel functions with respect to the radial variable. In addition, thanks to the condition of continuity of the

equilibrium total pressure

$$p_0 + \frac{B_0^2}{2\mu_0} = p_e + \frac{B_e^2}{2\mu_0},$$

the relationship between the equilibrium densities can be written as

$$\frac{\rho_e}{\rho_0} = \frac{2C_0^2 + \gamma V_A^2}{2C_e^2 + \gamma V_{Ae}^2}.$$

MHD waves propagating in a magnetic flux tube can be classified according to the number of radial nodes (fundamental or overtone), the radial structure (surface or body), and the relative propagation speed (slow and fast magneto-acoustic modes, Alfvén or intermediate modes). Accordingly, waves that correspond to the azimuthal wavenumber $n = 0$ are the sausage modes and kink modes have $n = 1$ (see Figure 2.7). Waves for which $n \geq 2$ are called fluting modes. Within the waveguide, body waves have an oscillating pattern in the radial direction, and their lowest amplitude is found close to the waveguide's boundary. Surface waves, on the other hand, propagate in such a way that they are evanescent both inside and outside the magnetic flux tube and reach their largest amplitude at the waveguide's boundary. The dispersion curves, as solutions of the dispersion relations (2.30)-(2.31) are shown in Fig. (2.6), where we plot the phase speed of waves in terms of the dimensionless parameter ka under photospheric (top panel) and coronal conditions (bottom panel). In the solar photosphere slow surface waves are bounded by V_{Ae} and C_T and their phase speed slightly decreases with increasing wavenumber, or decreasing wavelength. The slow body waves are confined to the region between C_T and C_0 and their phase speed increases with the wavenumber. Since the values of the tube and sound speeds are so close to each other, the phase speed of slow waves shows a small variation with the wavenumber. Fast surface waves are located between C_0 and C_e. It is worth noting that the fast body waves do not appear under photospheric conditions. Figure (2.6, bottom panel), on the other hand, shows the phase speed of the sausage and kink slow and fast body waves under coronal conditions. Similar to waves in the photosphere, slow body waves are bounded by C_T and C_0. Fast body waves are confined to the regions between V_{Ae} and V_A. Under coronal conditions slow and fast surface waves do not appear. Thus, both panels show that the mean Alfvénic speed is the common phase speed for the kink fast surface wave under photo-

spheric conditions and for the kink fast body wave under coronal conditions. Finally, regions where no modes are shown are regions where waves are not propagating, i.e. they are leaky.

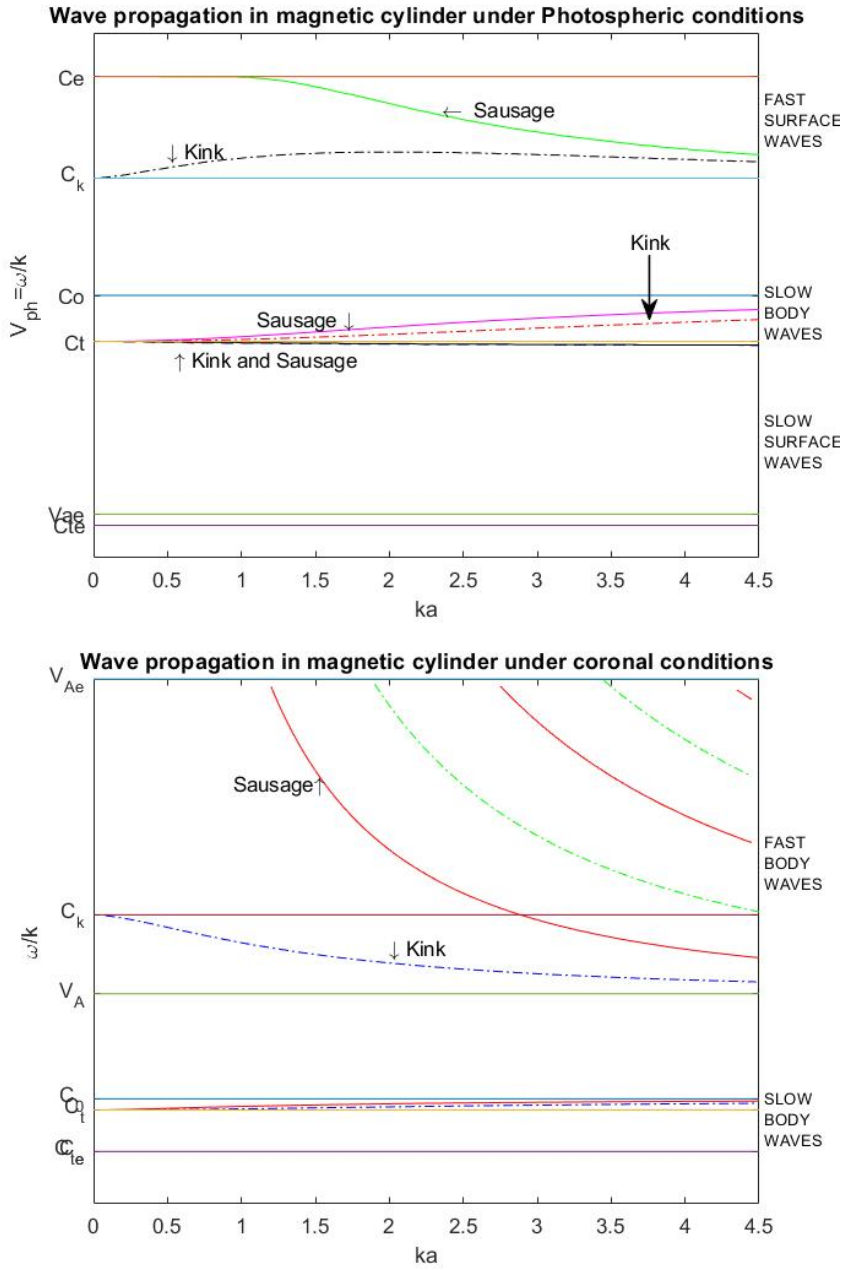

Figure 2.6: Dispersion curves of modes propagating in a magnetic cylinder under photospheric (top panel), and coronal conditions (bottom panel). Here we plot the phase speed of waves (ω/k) as a function of the dimensionless quantity ka. Sausage and kink modes are shown by solid and dashed lines, respectively.

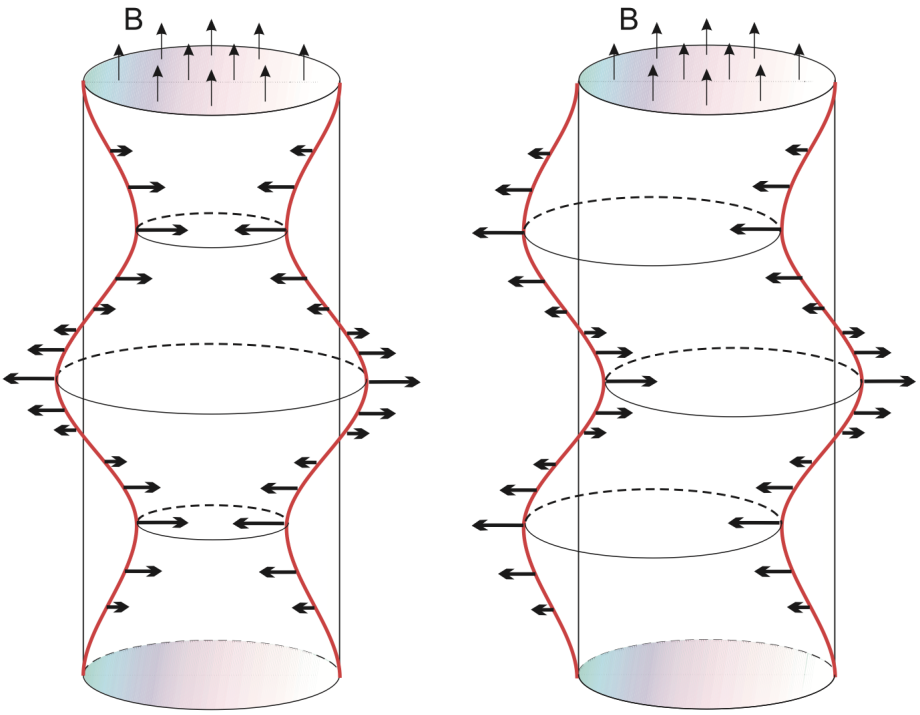

Figure 2.7: A cylindrical magnetic waveguide oscillates in the cases of a sausage mode (left panel) and a kink mode (left panel). The sausage mode involves squeezing and stretching the cylinder's edge, keeping the symmetry axis unperturbed. By contrast, the kink mode is shifting the symmetry axis. The thick side-way arrows show the velocity amplitudes, while the thin upward arrows point in the direction of the background magnetic field. Credit: Morton et al. (2012).

Since the Thesis concentrates on slow body modes in the solar photosphere, let us discuss in detail the value of the phase speed of waves in various limits. Using the standard formula for the derivatives of the Bessel functions we obtain that the dispersion relation for sausage body waves reduces to

$$\rho_0(k^2V_A^2-\omega^2)m_e\frac{K_1(m_ea)}{K_0(m_ea)}\frac{J_0(n_0a)}{J_1(n_0a)}=\rho_e(k^2V_{Ae}^2-\omega^2)n_0. \tag{2.32}$$

In the long wavelength limit (slender tube) we are going to look for a solution in the limit $ka\to 0$ as $n_0a\to 0$, $m_ea\to 0$. In this limit

$$K_0(m_ea)\sim -\ln(m_ea),\quad K_1(m_ea)\sim (m_ea)^{-1},\quad J_0(n_0a)\sim 1,\quad J_1(n_0a)\sim \frac{n_0a}{2}.$$

For visualisation purposes we have solved the dispersion relation numerically (using the bisection method to find the roots of the dispersion relation) and

displayed the value of density perturbation and radial component of the velocity for various types (sausage, kink and fluting modes) of fast and slow MHD waves propagating in a cylindrical flux tube propagating under coronal conditions. The values of density perturbations were normalised by their maximum value and the direction of the radial velocity is shown by black arrows. Figures (2.8) and (2.9) display the spatial distribution of density for fast body and surface modes, and the columns represent the three modes. Figures (2.10) and (2.11) display the same quantities relating to slow body and surface waves.

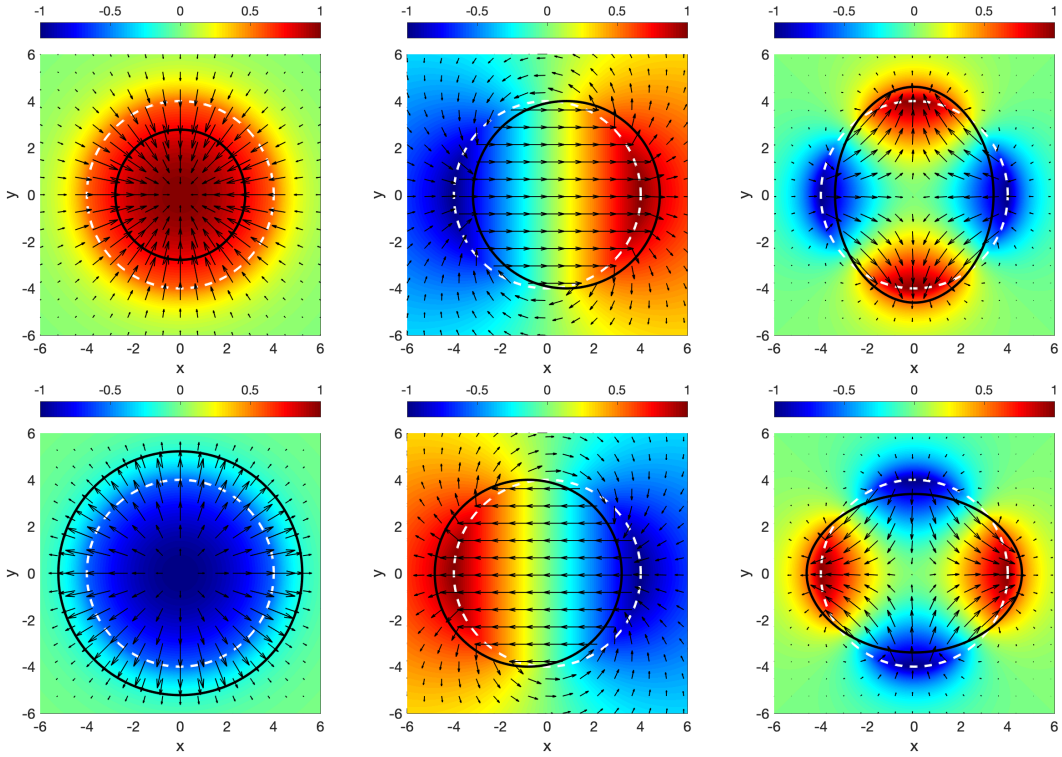

Figure 2.8: This figure displays the dimensionless density perturbation (colorbar) and the radial velocity perturbation (black arrows) for fast body modes propagating under coronal conditions. From left to right, the columns show the quantities for sausage ($n = 0$), kink ($n = 1$) and fluting ($n = 2$) modes. The boundary of the tube is indicated by the white dashed circle in the equilibrium state, and the black solid circle depicts the boundary's new position after the disturbance.

Figures (2.8)-(2.11) clearly demonstrate that, since the radial velocity in the case of fast waves are larger than in the case of slow waves, these waves (body or surface waves) have a greater impact on the tube boundary than slow waves, which have little to no noticeable impact on the boundary. This result can also be attributed to the fact that for fast waves the dominant

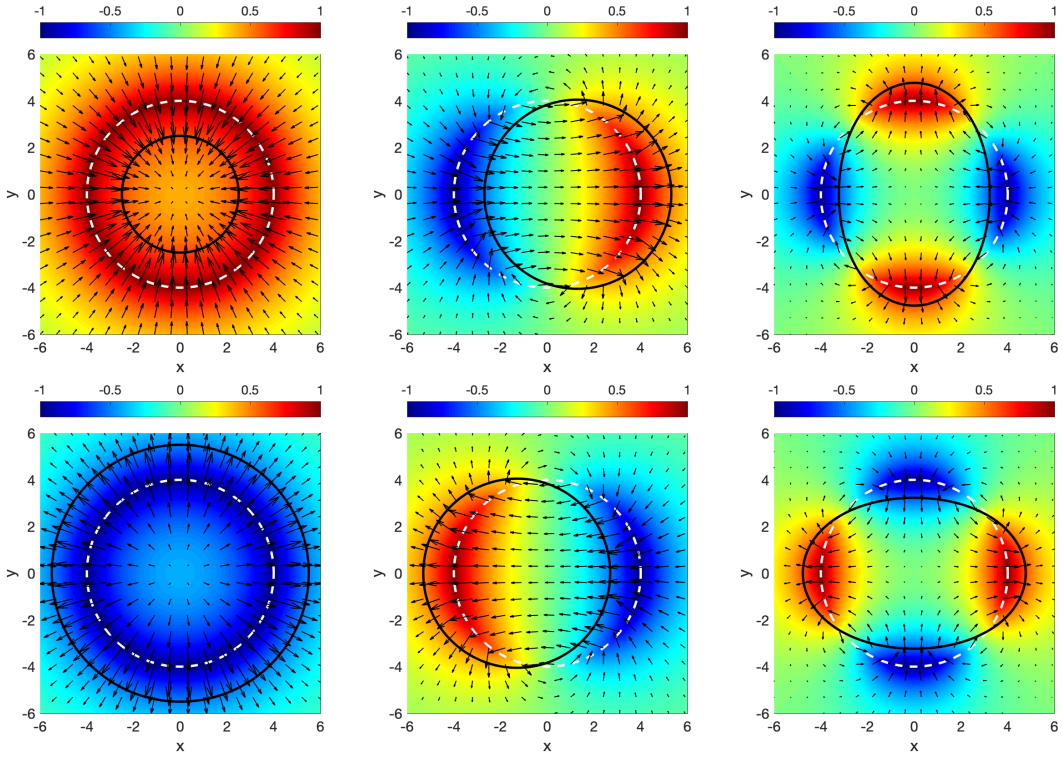

Figure 2.9: The same as in Fig. (2.8), but here we show the spatial structure of fast surface modes, however it appears only under photospheric conditions.

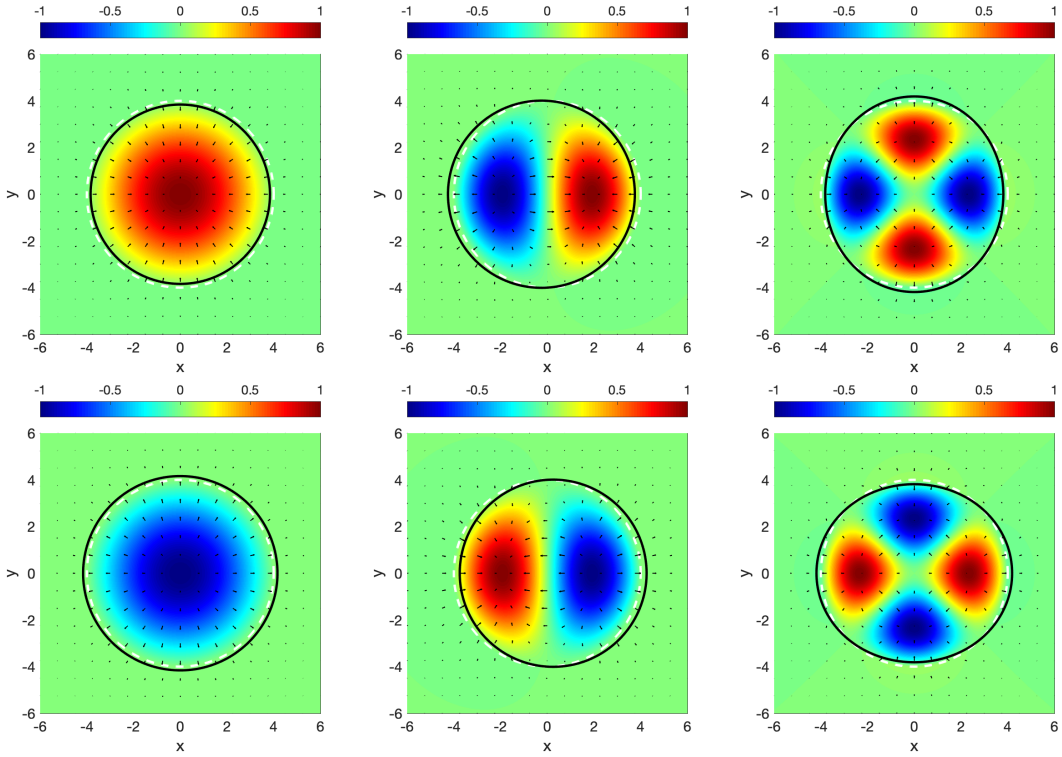

Figure 2.10: The same as in Fig. (2.8), but here we show the spatial structure for slow body modes.

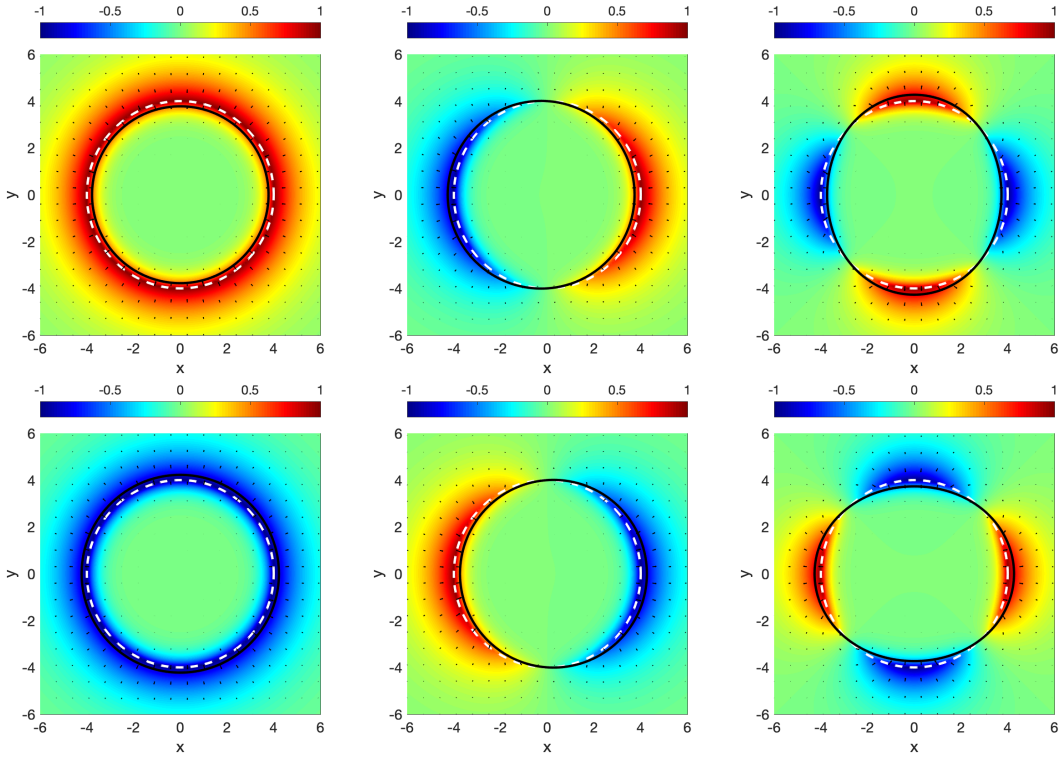

Figure 2.11: The same as in Fig. (2.8), but here we show the spatial structure of slow surface modes.

.

eigenfunction (say, velocity) is in the radial direction, while in the case of slow waves, this is in the longitudinal direction. As expected, the radial velocity and density perturbation amplitudes of the fast and slow surface waves are at their minimums near the tube's centre and maximums at its edge, respectively. The amplitude of the same quantities in the case of slow body waves is very small at the tube's boundary. The modes that we described and illustrated in these figures are the so-called fundamental modes since they only have one node in the radial direction. Overtones of modes can be recovered if more nodes in the radial direction are taken into account. For illustration the overtones in the case of slow body modes are shown in Fig. (2.12). Surface waves, on the other hand, lack overtones. This is clear from the dispersion diagram (see Fig. 2.6), which demonstrates that for a given value of ka, there is only one curve that corresponds to surface waves, however for body modes, there are multiple curves that are visible, each corresponding to a different set of radial nodes. Our conclusions are fully supported mathematically because surface waves are defined in terms of the Bessel function I_n, which exhibits a monotonic variation (rather than oscillatory behaviour). Body waves, in contrast, are characterised in terms of the oscillating Bessel function J_n.

Finally, an earlier investigation that is relevant for the research presented in this Thesis is the study by Aldhafeeri et al. (2022*a*). These authors investigated the accuracy of describing the properties of slow body waves by assuming a vanishing longitudinal velocity component (or total pressure) on the boundary of the photospheric waveguide and they compared their hypothesis to the full solution given by the study by Edwin and Roberts (1983*b*). This study showed that in the case of slow body waves in the solar photosphere, considering the total pressure perturbation or the longitudinal component of the velocity perturbation zero at the boundary of the waveguide produces errors in eigenvalues that are less than 1% from the values we would obtain by deriving the full dispersion relation, as shown in Fig. (2.13). This figure displays the dispersion curves of slow body kink and sausage modes obtained by solving the full dispersion relation (Eq. 2.31, solid lines) and the curves obtained by solving the approximative solution (dashed lines). As Fig. (2.13) shows, the difference in the solutions for the two cases is less than 1%.

To further evidence our modelling framework, we also show the variation of the longitudinal component of the velocity in a circular waveguide (see Fig. 2.14) as a result of solving the full dispersion relation (as given by the study

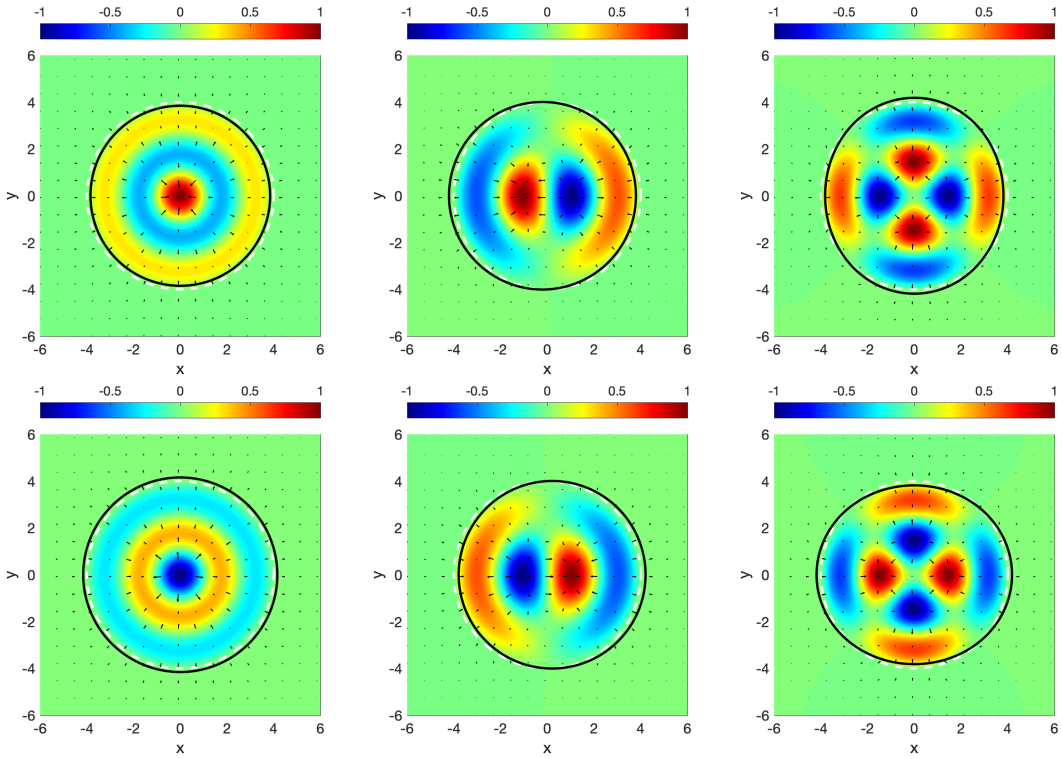

Figure 2.12: Similar to Fig. (2.8), except that here we display the spatial structure of slow body overtones, with different numbers of radial nodes.

by Edwin and Roberts (1983*b*)) for slow body sausage and kink modes modes (the left column). Here the normalised amplitude is shown with respect to the dimensionless wavenumber, ka. These figures clearly show that the amplitude of the longitudinal component of the velocity indeed attain their minimal value on the boundary, allowing us to treat these modes in the next chapters such that their amplitude is zero at the boundary, i.e. we will solve our governing differential equations such that we will impose a Dirichelt boundary condition, i.e. $V_z(r = a) = 0$. Given the relationship between this component of the velocity and total pressure, the same idea applies to the equations describing the spatial variation of the total pressure. In order to evidence the relative difference between the maximum of various body modes and the amplitude of V_z at the boundary the locations of these maximas are shown in the second column by blue and green dots for waves corresponding to different values of the radial wavenumber. These variations showed that the fundamental sausage and kink modes have the largest amplitude inside the cylinder, while higher overtones have smaller amplitude with increasing the radial wavenumber. The same pattern is followed by the amplitude of V_z at the boundary, where the

amplitude of various overtones are close to zero. The right column of Fig. (2.14) shows the absolute value of the ratio of the maximum amplitude of V_z measured at the boundary of the waveguide and the maximum value attained inside the waveguide. On the horizontal axis of the panels in the second and third column we denote the modes that correspond to different values of the radial wavenumber.

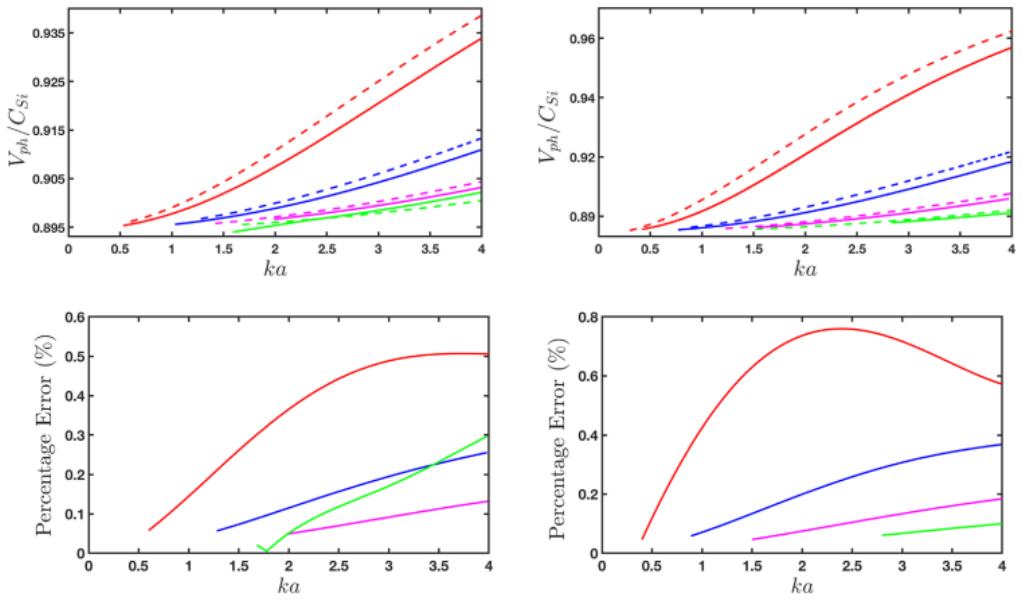

Figure 2.13: Dispersion curves in a photospheric flux tube for the kink (first row, left panel) and slow body sausage (first row, right panel) modes propagating in a magnetic cylinder, shown as the phase speed of waves in units of the internal sound speed (here denoted by C_{Si}). The dashed lines correspond to solutions of $V_{zi} = 0$ on the cylindrical waveguide boundary, where the expression of V_{zi} is given by Eq. (2.29). The solid lines correspond to the variation of the phase speed of waves in units of the internal sound speed obtained based on the dispersion relation Eq. (2.31). Here by red we show the fundamental modes, while the subsequent higher order modes are shown by blue, magenta. The percentage error in solving the dispersion relation and the solutions derived by presuming $V_{zi} = 0$ are displayed in (second row, left and right panels). Credit: Aldhafeeri et al. (2021).

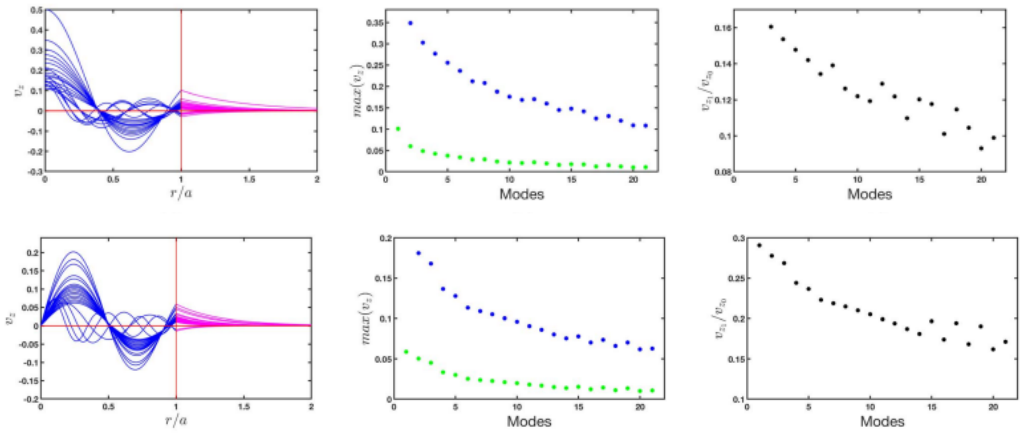

Figure 2.14: Variation of the z-component of the velocity perturbation over the cylindrical waveguide's boundary for slow sausage (first row) and slow body (second row) under photospheric settings for $an_0 > 4$. The left column illustrates the variation of the normalised amplitude of V_z with the radial distance (in waveguide radius units), inside (blue) and outside (magenta) of the tube. In the second column the green dots represent the maximum amplitude at the tube boundary, whereas the blue dots represent the maximum amplitude of V_z inside the flux tube for different modes. The right column displays the absolute value of the ratio between the maximum value obtained inside the waveguide and the maximum amplitude of V_z at the waveguide's boundary. Credit: Aldhafeeri et al. (2021).

2.2.4 Conclusions

The Chapter is based mainly on the theoretical framework of magnetohydrodynamics (MHD), which forms the mathematical foundation for describing wave behavior in plasma environments. Dispersion relations, key equations describing the relationship between wave frequency and wavevector, are derived to understand the properties of waves. These relations are obtained through analytical techniques and numerical methods, building upon earlier work by Roberts (1981*a*), Edwin and Roberts (1982*a*), Edwin and Roberts (1983*b*) and others. The dispersion relations are solved to obtain dispersion diagrams, illustrating waves' behavior in various geometries such as magnetic slabs and cylinders. These diagrams serve as fundamental tools for understanding wave propagation and guiding principles for the research presented in the Thesis.

In the recent investigation byAldhafeeri et al. (2022*a*), they examined the accuracy of describing slow body waves by assuming a vanishing longitudinal velocity component or total pressure at the boundary of the photospheric

waveguide. They compared this hypothesis to the full solution provided by Edwin and Roberts (1983*b*). Their study revealed that for slow body waves in the solar photosphere, assuming zero total pressure or longitudinal velocity perturbation at the boundary of the waveguide resulted in errors in eigenvalues of less than 1% compared to deriving the full dispersion relation. These findings were utilized in our investigation to further analyze the properties of waves and their identification in inhomogeneous wave guides.

Ultimately, these dispersion diagrams serve as invaluable tools for researchers, offering a roadmap for navigating the complex terrain of MHD wave dynamics. By elucidating the intricate interplay between magnetic fields, fluid motion, and wave propagation, the research contributes to a deeper understanding of plasma physics and paves the way for advancements in diverse fields such as astrophysics.

CHAPTER 3

Slow body MHD waves in photospheric flux tubes with circular cross-section in the presence of local equilibrium density inhomogeneity

3.1 Introduction

High resolution observations allow us to see waves and oscillations in almost every region of the solar atmosphere. While observations have their own limitations driven by the existing temporal and spatial resolution, waves helped to gain an understanding of various physical phenomena and to build up connectivity relationships between several important features in the solar atmosphere. At the same time most of the existing theoretical models operate with a high degree of idealisation. Waves propagating along the magnetic field are confined to magnetic structures that are modelled as straight and homogeneous structures with their cross-section being a regular shape (mostly circular). In reality observations show that magnetic waveguides are far from having a regular cross-section and being homogeneous either in the radial or longitudinal direction. Inhomogeneities in the plasma and magnetic field are known to strongly influence the properties of waves, leading to the modifications in the spectral properties of waves, wave amplification, mode conversion, etc. (e.g. De Pontieu et al. (2007); Morton et al. (2011*a*); Kwon and Bang (2018); Aldhafeeri et al. (2021); Stangalini et al. (2022); Albidah et al. (2022*b*); Skirvin et al. (2022*b*) to name a few).

Pores and sunspots are probably the most studied magnetic features in the solar atmosphere and they are the location of emerging large-scale magnetic field (of the order of a few kG). Observations nowadays can clearly observe the complex transversal shape of these structures, how they change, while intensity measurements give us observational evidence for the complicated and ran-

dom distribution of density inside them. Pores are located along the dividing lines between larger sunspots and smaller magnetic elements. The existence of waves and oscillations in sunspots has been extensively studied since Beckers and Tallant (1969)'s pioneering work demonstrated the oscillatory behavior of sunspots by measuring observed parameters of umbral flashes. Beckers and Schultz (1972) detected three-minute oscillations in Doppler velocity in the umbral area. Subsequent studies have shown that the most significant oscillation periods in sunspots and pores are 5 minutes at photospheric heights and 3 minutes at chromospheric heights, while the periods of global sunspot oscillations vary from hours to days (Nagashima et al., 2007; Stangalini et al., 2011; Jess et al., 2012, 2015; Grant et al., 2015; Khomenko and Collados, 2015). In addition, Stangalini et al. (2021) demonstrated that, in contrast to the anticipated 5 minutes, the dominant oscillations of a magnetic pore observed with the Interferometric BIdimensional Spectropolarimeter (IBIS) have periods of 3 minutes in the photosphere.

In the present Chapter we will focus on the modifications in the spatial structure and propagation speed of guided slow body MHD waves driven by an inhomogeneous equilibrium density distribution modelling the UDs in a sunspot. The background of our investigation is based on result presented in Chapter 2, as obtained by Aldhafeeri et al. (2022*a*), namely that slow body modes correspond to those perturbations for which the total pressure becomes almost zero near the boundary of the waveguide. According to their results slow body waves under photospheric conditions can be confidently described by solving a Helmholtz type partial differential equation with Dirichlet boundary condition, i.e. the total pressure perturbation vanishes at the boundary of the waveguide. The current analysis and the numerical recipe can be viewed as a starting point in the exploration of waves in realistic solar photospheric waveguides, where equilibrium density profile inhomogeneity generated from observations can be incorporated in the study of the property of slow body waves.

3.2 Governing equations

The dynamics of slow body waves will be discussed within the framework of ideal MHD and the equations that describe the spatial and temporal evolution of physical quantities are given by Eqs. (2.1)-(2.5). Although these equations

were reduced to a single equation in Chapter 2 (see Eq. 2.14), here we are going to have a slightly different approach, more relevant to the content of the Chapter. As before, we linearise the system of MHD equations and consider a straight magnetic cylinder with radius R and the dynamics will be described in cylindrical coordinates (r, θ, z).

The constant equilibrium magnetic field, $\mathbf{B}_0 = B_0\hat{z}$ is directed along the z-axis. The equilibrium plasma density profile inhomogeneity will be denoted by $\rho_0(r, \theta)$, the constant kinetic equilibrium plasma pressure by p_0 and the components of the velocity and magnetic field perturbations are $\mathbf{u} = (u_r, u_\theta, u_z)$ and $\mathbf{b} = (b_r, b_\theta, b_z)$. The perturbed quantities can be Fourier-decomposed with respect to the spatial coordinate z and time, t, by writing them proportional to $\exp\big(i(kz - \omega t)\big)$, where, as before, k is the longitudinal wave number and ω is the angular frequency. With these considerations the system of linearised MHD equations can be written as

$$-i\omega\rho + \rho_0\left[\frac{1}{r}\frac{\partial}{r}\left(ru_r\right) + \frac{1}{r}\frac{\partial u_\theta}{\partial\theta} + iku_z\right] + u_r\frac{\partial\rho_0}{\partial r} + u_\theta\frac{\partial\rho_0}{\partial\theta} = 0, \tag{3.1}$$

$$-i\rho_0\omega u_r = -\frac{\partial P_T}{\partial r} + ik\frac{B_0}{\mu}b_r, \tag{3.2}$$

$$-i\rho_0\omega u_\theta = -\frac{1}{r}\frac{\partial P_T}{\partial\theta} + ik\frac{B_0}{\mu}b_\theta, \tag{3.3}$$

$$\omega\rho_0 u_z = kP_T - k\frac{B_0}{\mu}b_z, \tag{3.4}$$

$$b_r = -B_0\frac{k}{\omega}u_r, \quad b_\theta = iB_0ku_\theta, \quad b_z = -iB_0\frac{1}{\omega r}\frac{\partial}{\partial r}(ru_r) - iB_0\frac{1}{\omega r}\frac{\partial u_\theta}{\partial\theta}, \tag{3.5}$$

$$p = -i\rho_0\frac{C_S^2}{\omega}\left[\frac{1}{r}\frac{\partial}{r}\left(ru_r\right) + \frac{1}{r}\frac{\partial u_\theta}{\partial\theta} + iku_z\right], \tag{3.6}$$

The above equations can be reduced to system of equations given only in terms of the components of the velocity and total pressure perturbations, as

$$\frac{\rho_0}{\omega}\left(\omega^2 - k^2V_A^2\right)u_r = -i\frac{\partial P_T}{\partial r}, \tag{3.7}$$

$$\frac{\rho_0}{\omega}\left(\omega^2 - k^2V_A^2\right)u_\theta = -i\frac{1}{r}\frac{\partial P_T}{\partial\theta}, \tag{3.8}$$

$$\omega\rho_0 u_z = kP_T + i\frac{kB_0^2}{\mu r\omega}\frac{\partial}{\partial r}\left(ru_r\right) + i\frac{kB_0^2}{\mu r\omega}\frac{\partial u_\theta}{\partial\theta}. \tag{3.9}$$

In addition, from the definition of the total pressure perturbation we have that

$$P_T = -i\frac{\rho_0(C_S^2+V_A^2)}{\omega}\left[\frac{1}{r}\frac{\partial}{\partial r}\left(ru_r\right)+\frac{1}{r}\frac{\partial u_\theta}{\partial\theta}\right]+\frac{\rho_0 k C_S^2}{\omega}u_z, \tag{3.10}$$

where now

$$C_S(r,\theta)=\sqrt{\frac{\gamma p_0}{\rho_0(r,\theta)}}, \quad V_A(r,\theta)=\frac{B_0}{\sqrt{\mu\rho_0(r,\theta)}},$$

are the adiabatic sound and Alfvén speeds. Using the expressions that connect velocity components with the total pressure perturbation given by Eqs. (3.7)-(3.10), we can derive a single equation for the total pressure perturbation as

$$\frac{\partial}{\partial r}\left[\frac{r}{\rho_0\left(\omega^2-k^2V_A^2\right)}\frac{\partial P_T}{\partial r}\right]+\frac{1}{r}\frac{\partial}{\partial\theta}\left[\frac{1}{\rho_0\left(\omega^2-k^2V_A^2\right)}\frac{\partial P_T}{\partial\theta}\right]-\frac{m_0^2 r}{\rho_0(\omega^2-k^2v_A^2)}P_T=0, \tag{3.11}$$

where the magnetoacoustic parameter, m_0^2, has been defined earlier (see Eq. 2.28). We should mention here that although the form of m_0^2 agrees with its counterpart in homogeneous plasma, here all phase speeds are functions of r and θ.

In an inhomogeneous plasma with a density varying in the radial and azimuthal direction the system of equations describing the evolution of perturbations (see, e.g. Eqs. 3.7-3.10) is prone to the appearance of singularities that can lead to the appearance of resonances. The phenomenon of resonant absorption has been used extensively as a mechanism to explain plasma heating by waves, scattering of p-modes by sunspots, and damping of kink oscillations of coronal loops, etc. Sakurai et al. (1991*a*); Keppens et al. (1994); Ballai et al. (2000); Ruderman and Roberts (2002). Indeed, Eq. (3.11) becomes singular at $\omega=\pm kV_A$. However, since we are dealing with waves in the short wavelength limit, where the propagation speed of slow body waves approaches the internal sound speed, the singularities will not appear.

In a homogeneous plasma, where ρ_0 is independent on r and θ, the total pressure perturbation has an azimuthal symmetry, i.e. proportional to $e^{im\theta}$, where m is the azimuthal wavenumber. As a consequence, the governing equation for the total pressure perturbation inside the cylinder simplifies to

$$\frac{d^2P_T}{dr^2}+\frac{1}{r}\frac{dP_T}{dr}-\left(m_0^2+\frac{m^2}{r^2}\right)P_T=0, \tag{3.12}$$

According to the study by Edwin and Roberts (1983*b*) the dispersion relation of MHD waves is obtained by matching the solutions obtained inside the magnetic flux tube (see Eq. 3.12) with the evanescent solutions obtained outside the flux tube using the continuity of the total pressure and the radial component of the velocity perturbations at the boundary of the tube. Among all possible modes predicted by the theory developed by Edwin and Roberts (1983*b*), the slow body modes analysed in the present Thesis are confined to the region between the tube speed, C_T, and the sound speed inside the tube, C_S. It is worth noting that the phase speed of slow body waves increases with increasing the wavenumber k, or decreasing wavelength. In the thick flux tube approximation the phase speed of slow body modes tends towards the internal sound speed, C_S, under photospheric conditions.

Let us return to the inhomogeneous flux tube case. Since we are interested in body waves, from now on we will use $n_0^2 = -m_0^2$ as our magnetoacoustic parameter. In addition, our analysis will be restricted to thick flux tube, where the wavelength of waves is much smaller than the radius of the tube, i.e. $kR \gg 1$. It is our assumption that in this limit the behaviour of slow body modes is similar to the one in a homogeneous waveguide, i.e. the phase speed of waves can be written as $\omega^2/k^2 \approx C_S^2(1-\nu)$, where ν is a small dimensionless positive quantity and $\nu = 1 - \omega^2/k^2C_S^2$.

Let us rewrite Eq. (3.11) for slow body modes into dimensionless form by introducing the new variable $\tilde{r} = r/R$, where R is the constant radius of the flux tube. From now on, for simplicity, we will drop the *tilde*. As a result, the dimensionless governing equation for the total pressure perturbation becomes

$$\frac{\partial}{\partial r}\left[\frac{r}{\rho_0(C_S^2-V_A^2)}\frac{\partial P_T}{\partial r}\right] + \frac{1}{r}\frac{\partial}{\partial \theta}\left[\frac{1}{\rho_0(C_S^2-V_A^2)}\frac{\partial P_T}{\partial \theta}\right] + \frac{n_0^2 r R^2}{\rho_0(C_S^2-V_A^2)}P_T = 0. \tag{3.13}$$

By taking into account that the equilibrium plasma pressure is a constant quantity (in the presence of homogeneous equilibrium magnetic field, this limit would correspond to the constant plasma-β limit), the coefficient function present in the terms of the above differential equation can be written as

$$\frac{1}{\rho_0(C_S^2-V_A^2)} = \frac{1}{\rho_0\left(\gamma p_0/\rho_0 - B_0^2/\mu\rho_0\right)} = \frac{1}{\left(\gamma p_0 - B_0^2/\mu_0\right)} = \frac{1}{B_0^2/\mu_0}\frac{1}{\left(\gamma\beta/2-1\right)}. \tag{3.14}$$

Here plasma-β is constant and $V_A^2/C_S^2 = 2/\gamma\beta$. Finally, after some algebra,

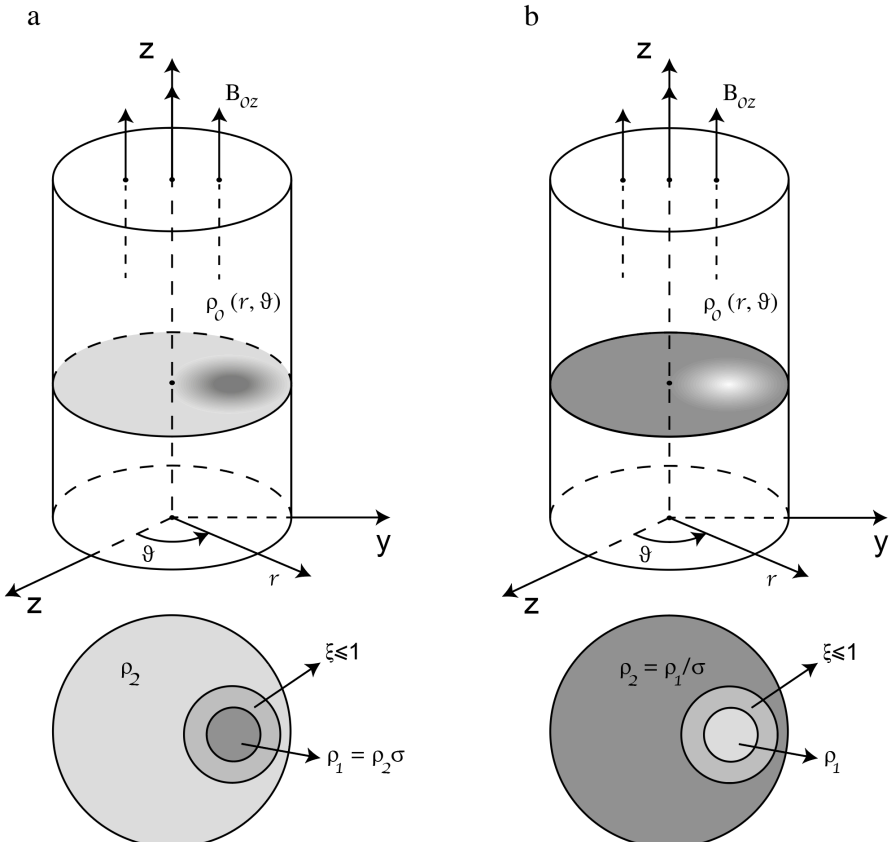

Figure 3.1: A schematic representation of the local equilibrium plasma density profile inhomogeneity inside the cylindrical waveguide in the case of a density enhancement (left column) and density depletion (right column). The top row show the 3D configuration of density, while the bottom row represents a horizontal cut in the density distribution. The plots show (for illustration) an eccentric distribution of density with $\epsilon_1 \neq 0$ and $\epsilon_2 = 0$. Credit: Asiri et al. (2024)

the governing equation for the total pressure becomes

$$\frac{\partial}{\partial r}\left(r\frac{\partial P_T}{\partial r}\right) + \frac{1}{r}\frac{\partial^2 P_T}{\partial \theta^2} - (kR)^2\left(1 - \frac{\omega^2}{k^2 C_S^2(r,\theta)}\right)\left(1 - \frac{2}{\gamma\beta}\right) r P_T = 0. \quad (3.15)$$

The only term that contains information about the inhomogeneous character of the plasma is via the sound speed that appears in the third term of the above equation.

3.2.1 Transverse density profile

The inhomogeneous equilibrium plasma density distribution will be represented as a local density enhancement or depression that depends on the variables r and θ in the form

$$\rho_0(r,\theta) = \rho_2 \chi(r,\theta), \tag{3.16}$$

where ρ_2 is the homogeneous density of the annulus surrounding the inhomogeneous density distribution and $\chi(r,\theta)$ is the dimensionless quantity

$$\chi(r,\theta) = \left\{ 1 + \frac{(\sigma-1)}{2} \left[1 - \tanh\left(\frac{\psi(r,\theta)-\tau}{\xi} \right) \right] \right\}.$$

Here $\sigma = \rho_1/\rho_2$ is the ratio of densities between the maximum value inside the inhomogeneous density region (ρ_1) and the homogeneous density in the annulus between the density enhancement/depletion and the circular waveguide. The function $\psi(r,\theta)$, that contains all the information regarding the inhomogeneous character of density is defined as

$$\psi(r,\theta) = \sqrt{(ar\cos(\theta) - \epsilon_1)^2 + (br\sin(\theta) - \epsilon_2)^2}, \tag{3.17}$$

where ϵ_1 and ϵ_2, describe the location of the center of the density enhancement/depletion, τ is the ratio of the radii of the density inhomogeneity and the circular magnetic flux tube with $0 < \tau < 1$, ξ is the width of the annulus where the change of density occurs, i.e. gradual transition of density between two regions, and a and b are two quantities that describe the dimensionless length of the major and minor axis of an ellipse. Although, in principle, we could discuss the effects of an inhomogeneous density distribution in the form of an ellipse (to which a circle is just a particular case), here we are going to restrict our attention to circular shapes for which $a = b = 1$. The case $\epsilon_1 = \epsilon_2 = 0$ corresponds to the concentric case, while for any other pair of values, we are dealing with so-called eccentric cases. Figure 3.1 shows a representative distribution of the inhomogeneous equilibrium plasma density profile in the case of a density enhancement (left panel) and density depletion (right panel).

The spatial structure of various slow body modes and the variation of the

dimensionless eigenvalues for slow body modes, $V_{ph} = \omega/kC_S$ with respect to the parameters of the inhomogeneous equilibrium plasma density distribution will be studied numerically employing a suitable numerical algorithm for such a problem. The recovered dimensionless eigenvalues of our problem could also be interpreted as a quantitative measure of the change in the frequency. Given the particular equilibrium plasma model mentioned above, the inhomogeneous character of the plasma appears through the last term of Eq. (3.15), that can be written with the help of Eq. (3.16) as

$$\frac{\omega^2}{k^2 C_S^2(r,\theta)} = \frac{\omega^2 \rho_0(r,\theta)}{k^2 \gamma p_0} = \frac{\omega^2 \rho_2}{k^2 \gamma p_0} \frac{\rho_0(r,\theta)}{\rho_2} = \frac{\omega^2}{k^2 \tilde{C}_S^2} \chi(r,\theta), \tag{3.18}$$

where $\tilde{C}_S^2$ denotes the constant sound speed in the homogeneous annulus of density ρ_2. As before, for simplicity, will drop the *tilde* symbol. As a result, the governing equation for the total pressure becomes

$$\frac{\partial}{\partial r}\left(r\frac{\partial P_T}{\partial r}\right) + \frac{1}{r}\frac{\partial^2 P_T}{\partial \theta^2} - (kR)^2 \left(1 - \frac{\omega^2}{k^2 C_S^2}\chi\right)\left(1 - \frac{2}{\gamma\beta}\right) r P_T = 0. \tag{3.19}$$

The above equation is a Sturm-Liouville eigenvalue equation and the eigenvalues as well as the corresponding eigenfunctions can be determined using a Dirichlet boundary condition, i.e. $P_T(r,\theta) = 0$ at the boundary of the tube corresponding to $r = 1$.

3.3 Numerical method

Given the particulars of the problem, the most suitable method to deal with such equation is the Fourier–Chebyshev spectral (FCS) collocation method over the Dirichlet boundary condition $P_T(r = 1, \theta) = 0$, as this method can capture the assumed inhomogeneity in the circular cross section more accurately. In order to implement the numerical algorithm, Eq. (3.19) can be written as

$$\frac{\partial}{\partial r}\left(r\frac{\partial P_T}{\partial r}\right) + \frac{1}{r}\frac{\partial^2 P_T}{\partial \theta^2} + \kappa_0^2 r P_T - \kappa_0^2 \chi V_{ph}^2 r P_T = 0, \tag{3.20}$$

where $\kappa_0^2 = -(kR)^2(1 - 2/\gamma\beta)$. To implement the FCS method and obtain the eigenvalues and the corresponding eigenfunctions of Eq. (3.20), we will write

this equation in a compact form as

$$\left(\frac{\partial^2}{\partial r^2}+\frac{1}{r}\frac{\partial}{\partial r}+\frac{1}{r^2}\frac{\partial^2}{\partial \theta^2}+\kappa_0^2-\kappa_0^2\chi V_{ph}^2\right)P_T=0. \tag{3.21}$$

Our numerical model is smoothly nonuniform, allows a gradual change in the density of the loaded regions and avoids abrupt changes. To capture the rapid variation in density, a larger number of grid points are required for the non-uniform configurations of magnetic flux tube in the radial direction. Spectral collocation methods appear to offer the greatest accuracy for the least computational expense for this class of problems (Trefethen, 2023). In general, a spectral collocation method performs the following operations: 1) collects the given discrete data on the grid points, 2) interpolates the data globally, 3) evaluates the derivative of the interpolant on the grid points.

The solution of the differential Eq. (3.21) is written as the sum of orthogonal basis functions whose coefficient must satisfy the differential equation. The discretisation of the domain can be done using uniform or non-uniform grids depending upon the problem type. In general, a mathematical problem can be periodic or non-periodic. For periodic problems equidistant or uniform grid points are of best use but for non-periodic problems the accuracy of using the regular or uniform grid points is very poor, especially near the boundaries. Because of this reason, non-periodic functions are generally discretized over irregular or non-uniform grid points such as Chebyshev grid points. The Chebyshev grid points discretize the radial direction in an irregular manner, bounded between 0 and 1. In this approach, the number of grid points are denser near the boundaries that results in better accuracy by better depicting the effect of change due to applied boundary conditions. Such an approach leads to higher accuracy and decreases the code's run time. In case of equidistant grid points, the discrete data on grid points can be interpolated globally using the trigonometric interpolant (Fourier Spectral method) and for non-uniform grid points this can be done using Lagrange polynomial interpolant (Chebyshev Spectral method). In the Fourier Spectral method, a grid function, v, is interpolated by computing the band-limited interpolation of the delta function (δ) that is used to expand v as a linear combination of translated δ functions.

Let the $P(x)$ be the band limited interpolation, where x is the discrete and

bounded physical space given by $x \in \{h, 2h, ..., 2\pi - h, 2\pi\}$ and let k be the discrete and bounded wanumber in Fourier space given by $k \in \{-\frac{N}{2}+1, -\frac{N}{2}+2, \ldots, \frac{N}{2}\}$, where N is an even number given by $N = 2\pi/h$. The Kronecker delta function, δ_j, is given by

$$\delta_j = \begin{cases} 1, & j = 0 \ \ (mod\ N), \\ 0, & j \neq 0 \ \ (mod\ N). \end{cases}$$

The discrete Fourier transform (DFT) of an arbitrary function $\hat{v}_k$ is given by

$$\hat{v}_k = h \sum_{j=1}^{N} \exp(-ikx_j) v(x_j),$$

and the inverse discrete Fourier transform is given by

$$v_j = \frac{1}{2\pi} \sum_{k=-N/2+1}^{N/2} \exp(ikx_j)\hat{v}_k, \tag{3.22}$$

where $j = 1, ..., N$

Evaluating Eq. (3.22) would give a term $e^{iNx/2}$ with derivative $(iN/2)e^{iNx/2}$. Since $e^{iNx/2}$ represents a real, sawtooth wave on the grid, its derivative should be zero at the grid points, and not a complex exponential! The problem arises because Eq. (3.22) treats the highest wavenumber asymmetrically and can be resolved by defining $\hat{v}_{-N/2} = \hat{v}_{N/2}$. Therefore, Eq. (3.22) becomes

$$v_j = \frac{1}{2\pi} \sum_{k=-N/2}^{(N/2)'} \exp(ikx_j)\hat{v}_k, \tag{3.23}$$

where the prime denotes that the terms $k = \pm N/2$ are multiplied by $1/2$. Using the above concepts, the band-limited interpolant of δ is given by

$$P_N(x) = \frac{1}{2\pi} \sum_{k=-N/2}^{N/2} \exp(ikx)\hat{v}_k, \tag{3.24}$$

where $x \in [-\pi/h, \pi/h]$.

Using the formula for the discrete Fourier transform (DFT) $\hat{v}_k$ of δ, we

obtain $\hat{\delta}_k = h$ for each k, and so, from (3.24), we obtain

$$P_N(x) = \frac{h}{2\pi} \sum_{k=-N/2}^{N/2} e^{ikx} = \frac{h}{2\pi} \left\{ \frac{1}{2} \sum_{k=\frac{-N}{2}}^{\frac{N}{2}-1} e^{ikx} + \frac{1}{2} \sum_{k=\frac{-N}{2}+1}^{\frac{N}{2}} e^{ikx} \right\}$$

$$= \frac{h}{2\pi} \cos\left(\frac{x}{2}\right) \frac{e^{i\left(\frac{-N}{2}+\frac{1}{2}\right)x} - e^{i\left(\frac{x}{2}+\frac{1}{2}\right)}}{e^{-i\left(\frac{x}{2}\right)} - e^{i\left(\frac{N}{2}\right)x}}$$

$$= \frac{h}{2\pi} \cos\left(\frac{x}{2}\right) \frac{e^{i\left(\frac{-N}{2}\right)x} - e^{i\left(\frac{x}{2}\right)}}{e^{-i\left(\frac{x}{2}\right)} - e^{i\left(\frac{N}{2}\right)x}}$$

$$= \frac{h}{2\pi} \cos\left(\frac{x}{2}\right) \sum_{k=\frac{-N}{2}+\frac{1}{2}}^{\frac{N}{2}-\frac{1}{2}} e^{ikx} = \frac{h}{2\pi} \cos\left(\frac{x}{2}\right) \frac{\sin\left(\frac{Nx}{2}\right)}{\sin\left(\frac{x}{2}\right)}.$$

Using the identity $\frac{\pi}{h} = \frac{N}{2}$, the equation for $P_N(x)$ becomes

$$S_N(x) = \frac{\sin(\pi x/h)}{(2\pi/h)\tan(x/2)}.$$

When x tends to zero, $tan(x/2) \approx x/2$, therefore $S_N(x)$ will turn into a *sinc* function, so the band-limited interpolant of the δ function is the periodic *sinc* function.

Considering a periodic delta function, the periodic grid function v_j takes the form

$$v_j = \sum_{m=1}^{N} v_m \delta_{j-m},$$

and the band-limited interpolant function is given by

$$P(x) = \sum_{m=1}^{N} v_m S_N(x - x_m).$$

In this case, the derivative of the periodic *sinc* function at a grid point is obtained as

$$S'_N = \begin{cases} 0, & j \equiv 0 \pmod{N}, \\ \frac{1}{2}(-1)^j \cot(jh/2), & j \not\equiv 0 \pmod{N}. \end{cases}$$

The series obtained from the above relation become the entries of the columns

for the first order of Fourier spectral differentiation matrix, $D_{\theta N}$, which on a finite grid point is given as

$$D_{\theta N} = \begin{pmatrix} 0 & & & -\frac{1}{2}\cot\frac{1h}{2} \\ -\frac{1}{2}\cot\frac{1h}{2} & \ddots & \ddots & \frac{1}{2}\cot\frac{2h}{2} \\ \frac{1}{2}\cot\frac{2h}{2} & \ddots & & -\frac{1}{2}\cot\frac{3h}{2} \\ -\frac{1}{2}\cot\frac{3h}{2} & & \ddots & \vdots \\ \vdots & \ddots & \ddots & \frac{1}{2}\cot\frac{1h}{2} \\ \frac{1}{2}\cot\frac{1h}{2} & & & 0 \end{pmatrix}. \tag{3.25}$$

Similarly, the higher derivative of the periodic *sinc* function and the corresponding second order Fourier spectral differentiation matrix, $D^{(2)}_{\theta N}$, on the grid points are obtained as

$$S''_N = \begin{cases} \frac{-\pi^2}{3h^2} - \frac{1}{6}, & j \equiv 0 \pmod N, \\ -\frac{(-1)^j}{2\sin^2(\frac{jh}{2})}, & j \equiv 0 \pmod N, \end{cases}$$

therefore

$$D^{(2)}_{\theta N} = \begin{pmatrix} \ddots & \vdots & \\ \ddots & -\frac{1}{2}\csc^2\left(\frac{2h}{2}\right) & \\ \ddots & \frac{1}{2}\csc^2\left(\frac{h}{2}\right) & \\ & -\frac{\pi^2}{3h^2} - \frac{1}{6} & \\ & \frac{1}{2}\csc^2\left(\frac{h}{2}\right) & \ddots \\ & -\frac{1}{2}\csc^2\left(\frac{2h}{2}\right) & \ddots \\ & \vdots & \ddots \end{pmatrix}.$$

The Chebyshev grid points are constructed in order to obtain Chebyshev differentiation matrices, which are used to determine the derivative of a function along the radial direction. Consider a grid function v that is defined on the Chebyshev points. Then a discrete derivative, q, can be obtained by defining a unique polynomial P of degree N such that $P(x_j) = v_j$, $0 \le j \le N$ and $q_j = P'(x_j)$. The operations defined here are linear and can be represented as an $(N+1) \times (N+1)$ matrix. We denote the above operation by D_{rN} : $q = D_{rN}v$.

The grid points are obtained by discretising the domain using the relation

$$x_j = \cos\frac{j\pi}{N}, \quad j = 0, 1, \ldots, N, \tag{3.26}$$

where N is the total number of nodes. For interpolation between nodes we can use Lagrange polynomials. To have an idea how the interpolation process works, let us take a look at the simple cases $N = 1$ and $N = 2$, as an example before proceeding to the general case. When $N = 1$ the interpolation points are $x_0 = 1$ and $x_1 = -1$, and the interpolating polynomial through data v_0 and v_1 can be written in Lagrange form as

$$P(x) = \frac{1}{2}(1 + x)v_0 + \frac{1}{2}(1 + x)v_1.$$

To solve differential equations, we need to calculate the first and second order derivatives. Let us start by finding the matrix D_{r1} as first derivative defined by $w_j = P'(x)$, that is

$$P'(x) = \frac{1}{2}v_0 + \frac{1}{2}v_1. \tag{3.27}$$

This formula implies that D_{r1} is the 2×2 matrix whose first column contains the constant entries $1/2$ and whose second column contains entries $-1/2$. Now we can define: $w = D_{r1}v$, where D_{r1} is square matrix and v and w are vectors. For two grids points, w becomes

$$\begin{bmatrix} w_1 \\ w_2 \end{bmatrix} = \begin{bmatrix} \frac{1}{2} & \frac{-1}{2} \\ \frac{1}{2} & \frac{-1}{2} \end{bmatrix} \begin{bmatrix} v_0 \\ v_1 \end{bmatrix}, \quad \text{where} \quad D_{r1} = \begin{bmatrix} \frac{1}{2} & \frac{-1}{2} \\ \frac{1}{2} & \frac{-1}{2} \end{bmatrix}. \tag{3.28}$$

For $N = 2$, the discretised points are $x_0 = 1$, $x_1 = 0$ and $x_2 = -1$. The corresponding interpolant polynomial is obtained as the quadratic function

$$P(x) = \frac{1}{2}x(1 + x)v_0 + (1 + x)(1 - x)v_1 + \frac{1}{2}x(x - 1)v_2,$$

whose derivative can be written as as the linear function in x

$$P'(x) = \left(x + \frac{1}{2}\right)v_0 - 2xv_1 + \left(x - \frac{1}{2}\right)v_2.$$

The j-th term samples of the above equation at $x = 1, 0$ and -1 becomes the

j-th column of the 3×3 differentiation matrix D_{r2} as

$$D_{r2} = \begin{bmatrix} \frac{3}{2} & -2 & \frac{1}{2} \\ \frac{1}{2} & 0 & -\frac{1}{2} \\ -\frac{1}{2} & 2 & -\frac{3}{2} \end{bmatrix}.$$

In the similar way, other Chebyshev differentiation matrices are constructed by interpolating the discrete data over the grid points globally using Lagrange polynomial. For each $N \geq 1$, let the rows and columns of the $(N+1) \times (N+1)$ Chebyshev spectral differentiation matrix D_{rN} be indexed from 0 to N. We calculate the first order of the Chebyshev spectral differentiation matrix D_{rN} by calculating the first derivative of the Lagrange interpolant polynomial function defined on the finite grids which can be written as

$$D_{rN} = \begin{array}{|c|c|c|} \hline \frac{2N^2+1}{6} & 2\frac{(-1)^j}{1-x_j} & \frac{1}{2}(-1)^N \\ \hline -\frac{1}{2}\frac{(-1)^i}{1-x_i} & \begin{array}{c} \frac{(-1)^{i+j}}{x_i-x_j} \\ \frac{-x_j}{2\left(1-x_j^2\right)} \\ \frac{(-1)^{i+j}}{x_i-x_j} \end{array} & \frac{1}{2}\frac{(-1)^{N+i}}{1-x_i} \\ \hline -\frac{1}{2}(-1)^N & -2\frac{(-1)^{N+j}}{1-x_j} & -\frac{2N^2+1}{6} \\ \hline \end{array}$$

This is equivalent to the subsequent form

$$(D_{rN})_{00} = \frac{2N^2+1}{6}, \quad (D_{rN})_{NN} = \frac{-2N^2+1}{6}, \tag{3.29}$$

$$(D_{rN})_{jj} = \frac{-x_j}{2(1-x_j^2)}, \quad j = 1, \ldots, N-1, \tag{3.30}$$

$$(D_{rN})_{ij} = \frac{c_i(-1)^{i+j}}{c_j(x_i - x_j)}, \quad i \neq j, \quad i, j = 1, \ldots, N-1, \tag{3.31}$$

where the constant c_i takes the values

$$c_i = \begin{cases} 2, & i = 0 \text{ or } N, \\ 1, & \text{otherwise.} \end{cases} \tag{3.32}$$

The j-th column of D_{rN} contains the derivative of the degree N of the polynomial interpolant to the delta function supported at x_j, sampled at the grid points x_i.

The Chebyshev differentiation matrices constructed this way are then used to obtain the derivative of the governing equation. Hence, we calculate the higher order Chebyshev differentiation matrix by multiplying the first order of the Chebyshev spectral differentiation matrix by itself multiple times according to the higher order number. For example, we calculate the second order Chebyshev differentiation matrix by calculating $D_{rN}^2 = D_{rN} \times D_{rN}$.

For polar coordinates, studies suggest that the Fourier expansion works best for angular coordinates while Chebyshev expansion is best suited for radial coordinates. Using this information, therefore we can develop the Fourier–Chebyshev spectral collocation method that will be used to numerically solve our eigenvalue problem.

The present study follows the method developed by Fornberg Trefethen (2000). For our study we select an odd number of grid points in the r direction, an even number of grid points in the θ direction. For a periodic function, $v(x)$, trigonometric functions are an appropriate set of spectral basis. Let the interpolation of the function $v(x)$ be carried out over N points given by $x_1, \ldots, x_N$, where each point is separated by distance h as prescribed by Eq. (3.24). The derivative of the spectral interpolant can be estimated from the values of $v(x_j)$ at the sample points using

$$\left(\frac{dv}{dx}\right)_{\text{sp}} = P_N'(x)\big|_{x_j}. \tag{3.33}$$

The set of points $v(x_j)$ represents a vector function with N components as,

$v = v_1, ..., v_N$. Similarly, the spectral derivative can also be represented as a vector function with N components and is obtained by matrix multiplication. Like the previous cases, here the derivative of the interpolant function $P_N(x)$ becomes the entries for the matrix. In order to replace the Laplacian operator from polar coordinate $\nabla^2 = \partial_r^2 + r^{-1}\partial_r + r^{-2}\partial_\theta^2$ into a matrix of Fourier-Chebyshev differentiation, it is important to construct the spectral interpolant and its derivative with generalized independent variables. This can be done by Kronecker products of the differentiation matrices with each of the independent variables. Therefore, the Laplacian operator becomes

$$L = (D_1 + RE_1) \otimes I_l + (D_2 + RE_2) \otimes I_r + R^2 \otimes D_{\theta N}^{(2)}. \tag{3.34}$$

where D_1 and D_2 are the matrices whose elements are extracted from the second order Chebyshev spectral differentiation matrix corresponding to the $\partial^2/\partial r^2$ operator shown in the middle panel of Table. 3.1. E_1 and E_2 are the matrices whose elements extract from the first order Chebyshev spectral differentiation matrix for $(1/r)\partial/\partial r$ shown in the right hand side panel of Table. 3.1. In the above relation $D_{\theta N}^{(2)}$ stands for the $(1/r^2)\partial^2/\partial\theta^2$ operator, $R^{'}$ is a diagonal matrix $R^{'} = diag(r_j^{-1})$, $1 \leq j \leq (N_r - 1)/2$, and I_l and I_r are the identity matrices given by

$$I_l = \begin{pmatrix} I & 0 \\ 0 & I \end{pmatrix}, \quad I_r = \begin{pmatrix} 0 & I \\ I & 0 \end{pmatrix}. \tag{3.35}$$

The matrices in Eq. (3.34) are representations of the partial derivatives and are defined on the grid for Chebyshev (N_r, odd) and Fourier (N_θ, even) collocation points. The reason why they have been extracted is because of that the original Chebyshev differential matrix has been constructed based on the Chebyshev grid points which are defined on the negative and positive radial direction, bounded between $r \in [-1, 1]$. Following the the algorithm suggested by Trefethen (2000), the mapping of coordinates from polar to Cartesian coordinate system is 2-to-1, that is each (x, y) point in Cartesian geometry corresponds to two distinct points (r, θ) in polar geometry. At the origin ($x = y = 0$), the mapping follows an ∞-to-1 rule and the problem can be rectified by taking an odd number of grid parameters, (N), in the r direction. Using the symmetry $u(r, \theta) = u(-r, (\theta + \pi)(mod 2\pi))$, the portions of the matrix arising from the regions III and IV, which correspond to the negative radial direction (shown

Table 3.1: Details of the matrices whose elements extract from the second order Chebyshev spectral differentiation matrix, $D^{(2)}_{rN}$, and the first order Chebyshev spectral differentiation matrix, D_{rN}.

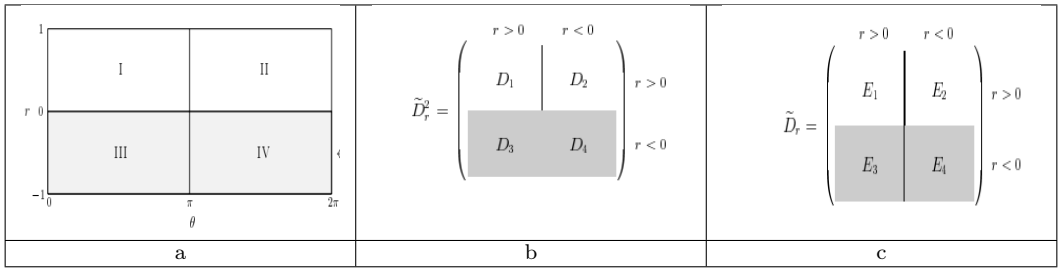

in the left hand side panel of Table. 3.1) can be discarded as these portions are redundant. The portions of the matrix that originate from the regions II and IV can also be discarded. However, the effect of these discarded portions of the matrix must be included into the Kronecker products.

Homogeneous Dirichlet boundary conditions for spectral collocation methods can be implemented by removing the first and/or last rows and columns of a spectral dimension matrix. After applying the above numerical concepts to the governing equation and performing some simplification, a matrix equation is obtained that can be used to solve the generalized eigenvalue problem written in matrix form

$$(L + \kappa_0^2)P_T - \kappa_0^2 \chi V_{ph}^2 P_T = 0. \tag{3.36}$$

In the present study, the eigenvalues and eigenvectors of the quadratic matrix polynomial are obtained using QZ factorization (also known as generalized Schur decomposition). The method is potentially capable of handling a variety of eigenvalue problems in the most efficient way. The code that calculates the eigenvalues and eigenfunctions uses the build-in MATLAB function '$polyeig(L + \kappa_0^2, -\kappa_0^2\chi)$', which is based on the QZ factorization. The code is tested against the well-known eigenvalues obtained for the case of the homogeneous and cylindrical flux tube. A similar study was conducted by Sathej and Adhikari (2009), who studied the oscillations of a drum modelled as a non-uniform membrane whose density smoothly changes between two predetermined values. They conducted a thorough analysis of the variance in the model's eigenvalues as a function of the model parameters using a Fourier-

Table 3.2: Values of the physical parameters used for the numerical modeling and analysis. Unless specified otherwise, for each case we consider $kR = 4$ and $\beta = 3 \times 10^{-3}$.

	σ	τ	ξ	ϵ_1	ϵ_2
C1: Uniform density	1				
C2: Non-uniform density enhancement					
C2.1: - concentric	2.5	0.3	9.1×10^{-2}	0	0
C2.2: - right eccentric	2.5	0.3	9.1×10^{-2}	0.25	0
C2.3: - upper right eccentric	2.5	0,3	9.1×10^{-2}	0.25	0.25
C3: Non-uniform density depletion					
C3.1: - concentric	0.5	0.7	9.1×10^{-2}	0	0
C3.2: - right eccentric	0.5	0.7	9.1×10^{-2}	0.25	0
C3.3: - upper right eccentric	0.5	0.7	9.1×10^{-2}	0.25	0.25
C4: Variation of V_{ph}					
C4.1: $2 \leq kR \leq 10$	2.5; 0.5	0.3; 0.7	9.1×10^{-2}	0; 0.35	0; 0.35
C4.2: $3 \times 10^{-6} \leq \beta \leq 3 \times 10^{-3}$	2.5; 0.5	0.3; 0.7	9.1×10^{-2}	0; 0.35	0; 0.35
C4.3.1: $2 \leq \sigma \leq 10$		0.3; 0.7	9.1×10^{-2}	0; 0.35	0; 0.35
C4.3.2: $0.45 \leq \sigma \leq 0.9$		0.3; 0.7	9.1×10^{-2}	0; 0.35	0; 0.35
C4.4: $0.3 \leq \tau \leq 0.7$	2.5; 0.5		9.1×10^{-2}	0; 0.35	0; 0.35
C4.5: $1.8 \times 10^{-5} \leq \xi \leq 0.1$	2.5; 0.5	0.3; 0.7		0; 0.35	0; 0.35
C4.6: $0.1 \leq \epsilon_1 \leq 0.5$	2.5; 0.5	0.3; 0.7	9.1×10^{-2}		0; 0.35

Chebyshev collocation method. Their code has also been benchmarked against the known eigenvalues of the uniform circular membrane, and they found a spectral convergence as the number of grid points increases. These authors determined the eigenvalues and the eigenvectors using a Cholesky decomposition algorithm.

In what follows we will analyze the effect of different physical parameters on the dimensionless phase speed ($V_{ph} = \omega/kC_S$) of slow body modes corresponding to the spatial structure of the total pressure perturbation under photospheric conditions. The parameters that could influence the characteristics of waves are connected to the waveguide and its plasma environment (plasma-β, dimensionless wavenumber, etc.), but also to the parameters that describe the local equilibrium density profile inhomogeneity. The solutions obtained for a homogeneous equilibrium plasma density distribution will be used as a reference benchmark for our comparisons.

3.4 Results

3.4.1 Slow body modes in the presence of a non-uniform density in the short wavelength limit

In this section, we will analyze the dependence of the phase speed of slow body modes and the spatial structure of the total pressure perturbation on the magnetic flux tube density inhomogeneity under solar photospheric conditions.

3.4.2 The spatial structure of slow body modes in the presence of a uniform density

The propagation of the MHD waves in a homogeneous cylindrical waveguide with uniform equilibrium density corresponds to case C1 (see Table 3.2), i.e. to the particular value of $\sigma = 1$ in Eq. (3.16) and previously this scenario was studied in detail by Edwin and Roberts (1983*a*). Fig. (3.2) shows the homogeneous distribution of normalized equilibrium density (left upper panel) and the spatial structure of the total pressure perturbation in the case of slow sausage fundamental body (SSFB, right upper panel), slow kink fundamental body (SKFB, left lower panel) and slow fluting fundamental body mode of order 2 (SF2FB, right lower panel). These results clearly show that in the homogeneous limit, slow body modes of different azimuthal order have global harmonic character. The color bar displays the magnitude of the dimensionless amplitude of the total pressure perturbation, P_T, with the red and blue shaded regions representing crests (maxima) and valleys (minima) of the amplitude.

3.4.3 The spatial structure of slow body modes in the presence of a non-uniform density

The changes in the spatial structure of slow body waves as well as the modification of the dimensionless phase speed in terms of the parameters of local equilibrium plasma density given by Eq. (3.16) will be discussed when the inhomogeneous density is represented as a local density enhancement ($\sigma > 1$) and density depletion ($\sigma < 1$). The modifications in the oscillatory patterns of waves are analyzed for three particular positions of the equilibrium density loading, e.g. concentric (case C2.1), right eccentric (case C2.2), and upper

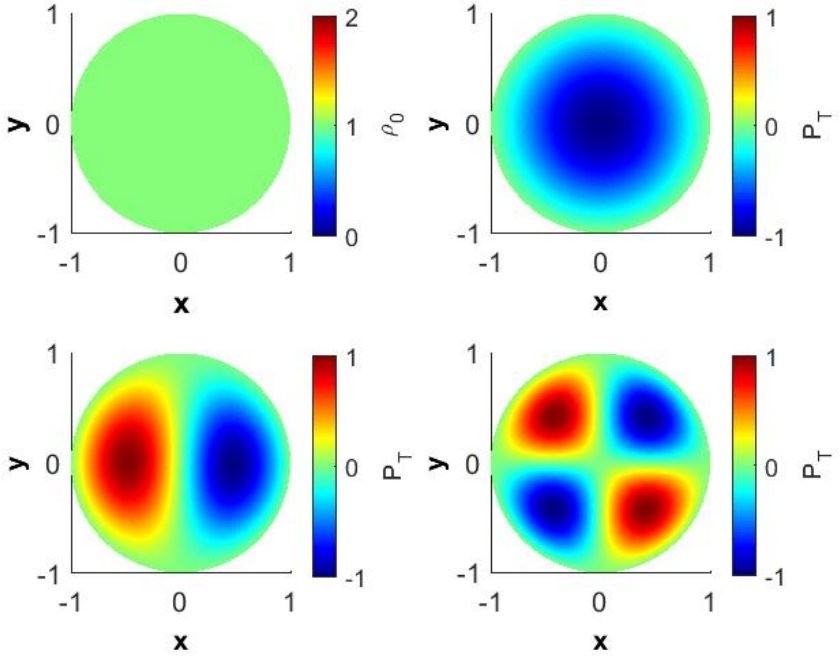

Figure 3.2: The density distribution (upper left panel) and the spatial structure of SSFB, SKFB, and SF2FB modes under photospheric conditions in a circular magnetic flux tube with uniform density ($\sigma = 1$). The color bars display the magnitude of the total pressure perturbation amplitude divided by its maximum value. The red and blue shaded regions represent crests (maxima) and valleys (minima) of amplitude variation of total pressure perturbation.

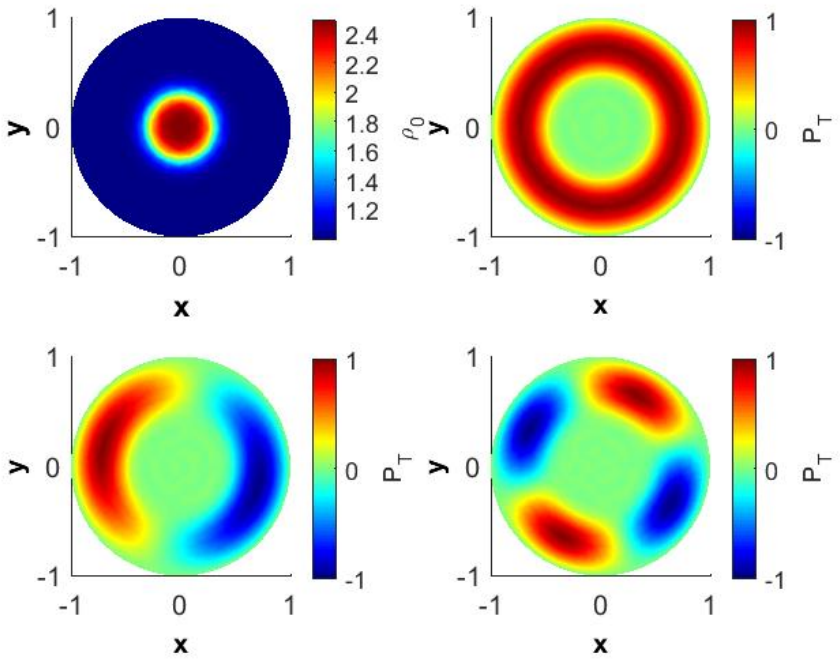

Figure 3.3: The same modes as in Fig. (3.2), but here we show the results in the presence of a concentric density enhancement. All characteristic values of parameters used in these numerical solutions correspond to the case C2.1 in Table (3.2).

right eccentric (case C2.3). The description of parameters related to these three cases is described in Table (3.2).

3.4.3.1 Slow body modes in the presence of concentric and eccentric density enhancements

Due to the changes in the values of the radial distribution of equilibrium density, it is expected that the dimensionless phase speed and the spatial structure of slow body waves will be modified. Let us first discuss the case C2.1. Figure (3.3) shows the radial distribution of the equilibrium density and the spatial distribution of the normalized value of the total pressure perturbation of SSFB, SKFB, and SF2FB modes. In the presence of concentric inhomogeneity the corresponding eigenmodes migrate towards the boundary of the waveguide, i.e. in the direction of lower density. By comparing Figs. (3.2) and (3.3) it is obvious that obtained MHD modes become more localized but, at the same time, maintain their symmetry with respect to the center of the flux tube. The regions where no oscillations are possible correspond to the combination of physical parameters that will make the value of n_0^2 in Eq. (3.19) change sign, so the governing equation does not describe the eigenfunction of a body mode. Surface waves cannot be cast in our description, as we had to impose a Dirichlet-type boundary condition that cannot be applied to surface waves. These regions simply show that here we have no slow body modes.

The enhanced eccentric equilibrium density distribution corresponds to a density loading whose position is shifted away from the origin (case C2.2) and the position of its center is controlled by the two parameters, ϵ_1 and ϵ_2. In reality, the position of the inhomogeneous density loading can be arbitrary, however, in the present study we discuss only cases that correspond to the shifted inhomogeneous density along the horizontal axis (Fig. 3.4, parameters given by case C2.2), and a position where both quantities describing the location of the density load are non-zero (Fig. 3.5, parameters given by case C2.3 in Table 3.2).

Figure (3.4) shows the radial distribution of the equilibrium density and the spatial structure of the normalized total pressure perturbation for the same slow body modes as before. Due to the considered density loading, the spatial extent of the eigenfunction shrinks and the global nature of these modes ceases. Comparing Figs. (3.2) and (3.4), it is evident that the oscillations are shifted,

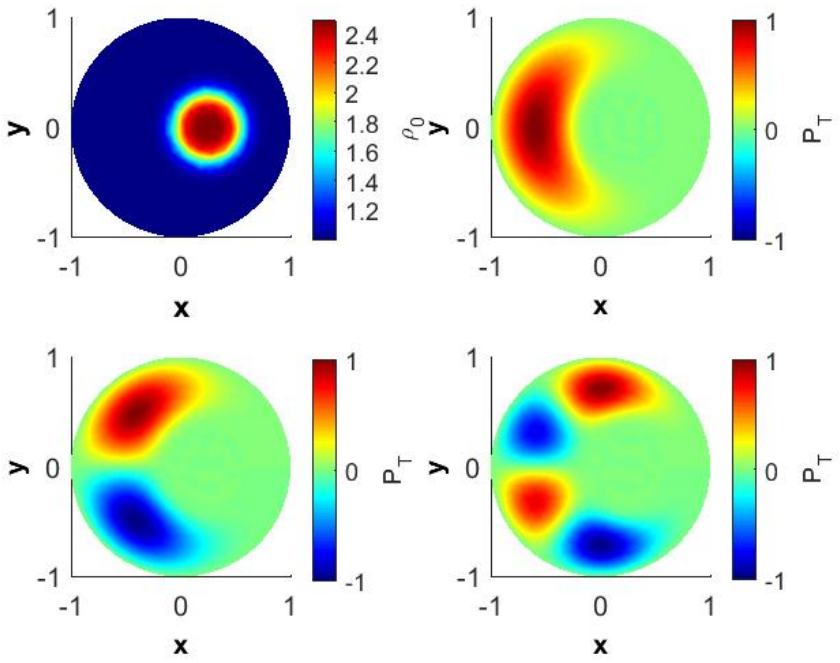

Figure 3.4: The same MHD modes as in Fig. (3.3), but here we show the results for an eccentric density loading, situated along the horizontal direction. The parameters used for this visualization are given as case C2.2 in Table (3.2).

again, towards regions of lower density, so they become more localized. When the density inhomogeneity is shifted along an arbitrary direction (along the first bisector as in Fig. (3.5)), the modification in the spatial structure of modes remains qualitatively the same.

3.4.3.2 Slow body modes in the presence of concentric and eccentric equilibrium density depletions

In the case of a depleted density inhomogeneity, the maximum value of density of the inhomogeneous region is less than the density of the homogeneous part of the waveguide, i.e. $\sigma < 1$. The values of parameters used for our numerical investigations are given in Table (3.2, case C3). Fig. (3.6, case C3.1) shows the spatial structure of the normalized total pressure perturbation corresponding to the same body modes as before in the case of concentric loading, while Figs. (3.7, case C3.2) and (3.8, case C3.3) show the spatial structure of the total pressure for an eccentric loading, when the density inhomogeneity is placed along the horizontal axis and in a position along the first bisector.

The results obtained for this case confirm the previous findings, namely

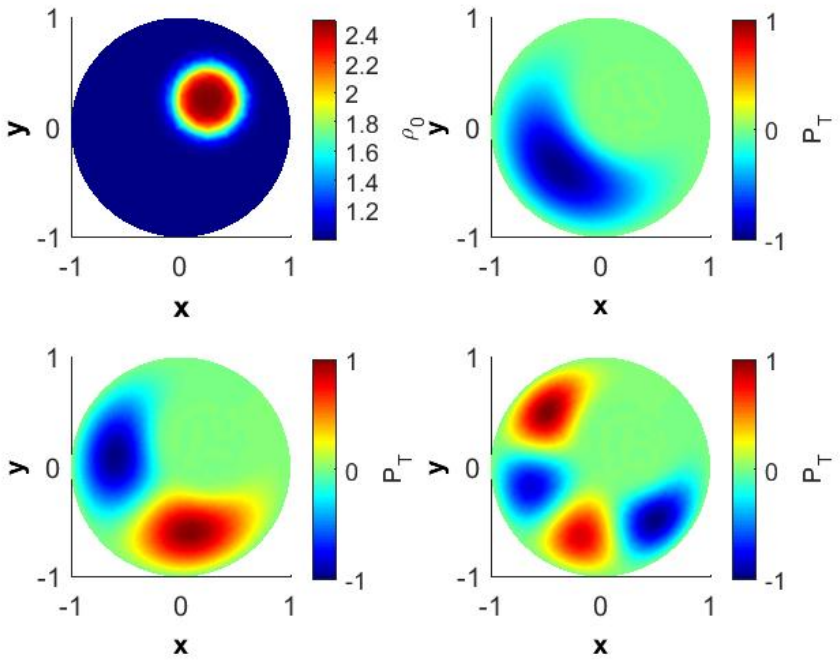

Figure 3.5: The same MHD modes as in Fig. (3.3), but here we show the results for an eccentric density loading, situated along the first bisector. The parameters used for this visualization are given as case C2.3 in Table (3.2).

that in the case of an inhomogeneous distribution of the equilibrium plasma density, the modes tend to lose their global character, instead they become localized in the region that corresponds to the lowest density. However, in contrast to the case C2 of density enhancement, in this case, the modes tend to be attached to the region of equilibrium density inhomogeneity. Moreover, unlike the distorted shape of modes found in case C2, the slow body modes in the depleted density case maintain their symmetric character. As before, the spatial structure of slow body modes does not change if the density loading is placed along the horizontal or vertical axes.

The migration of the location of modes in the presence of density inhomogeneity obtained for the density enhancement and depletion reveals one important consequence for observations. A localized wave observation in a sunspot could be a way to identify the location of a density inhomogeneity in the umbral region, even if this inhomogeneity cannot be seen in observations.

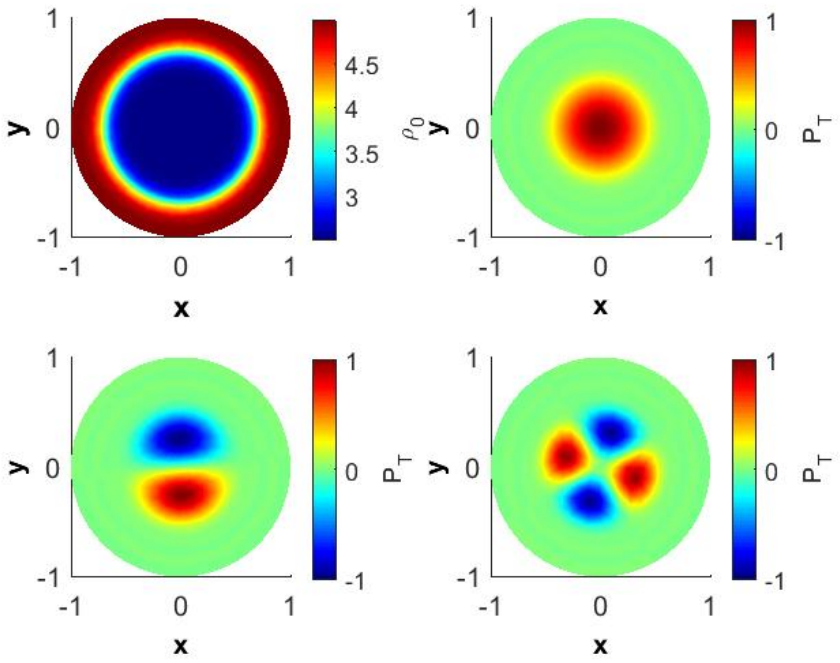

Figure 3.6: The same as in Fig. (3.3) but for the case of depleted concentric equilibrium density inhomogeneity. The parameters used for this visualization are given as Case C3.1 in Table (3.2).

3.4.4 Comparative study of the variation of the phase speed of slow body modes in the presence of an inhomogeneous density distribution

The results presented in the previous section show that the spatial structure of slow body modes propagating in a circular waveguide is influenced by a density inhomogeneity by the modifications in the location of these modes. However, due to the modification in the azimuthal symmetry, it is natural to expect that these modes are affected by changes in the phase speed of waves or their frequency. To address this problem in this section we carry out a comparative study of the variation of the dimensionless phase speed of body waves (or their dimensionless frequency) in terms of the parameters related to the plasma environment in which these waves propagate and wave characteristics (dimensionless wavenumber, kR, plasma-β), but also in terms of the parameters describing the inhomogeneous density (σ, τ, ξ and the values of the ϵ parameters). The details of the parameters used are summarized in Table (3.2, Case C4). The first two parameters (kR and β) are parameters that

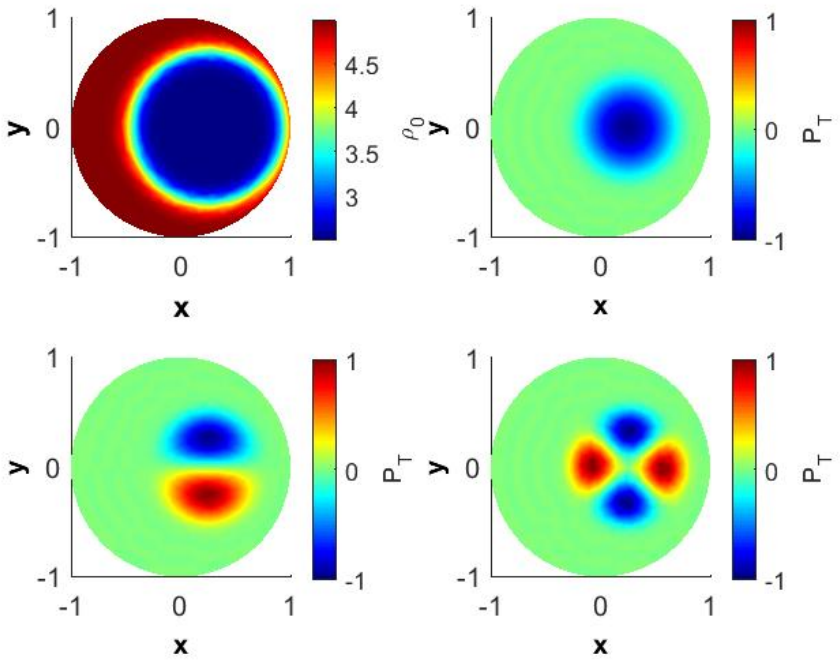

Figure 3.7: The same as in Fig. (3.6), but here the depleted density region is situated in an eccentric position along the horizontal axis. The parameters used for this visualization are given as Case 3.2 in Table (3.2).

influence the solution through the Eq. (3.19). The study will be performed considering the homogeneous density case as a benchmark value.

As the mathematical model described earlier refers to the short wavelength limit (wide flux tube), first we investigate the variation of the dimensionless phase speed of waves with the dimensionless wavenumber of body waves (for a constant tube radius the variation of the kR parameter is, in fact, describing the variation of the wavenumber, with increasing kR corresponding to a decrease in the wavelength of waves). Figure (3.9) (upper left panel) shows the variation of dimensionless phase speed for the three slow body modes with respect to kR in the case of uniform density: SSFB (solid line), SKFB (dash line) and SF2FB (dotted line). The three waves show a distinctive dispersive character for lower values of kR, while their dimensionless phase speed becomes practically independent of the wavelength of waves for higher values of kR, the dimensional speed of each wave tending to the sound speed, C_S. Since waves propagate faster for smaller wavelengths, these waves are known to have a positive dispersion. The behaviour of modes obtained here is similar to the variation of the phase speed determined by Edwin and Roberts (1983*a*).

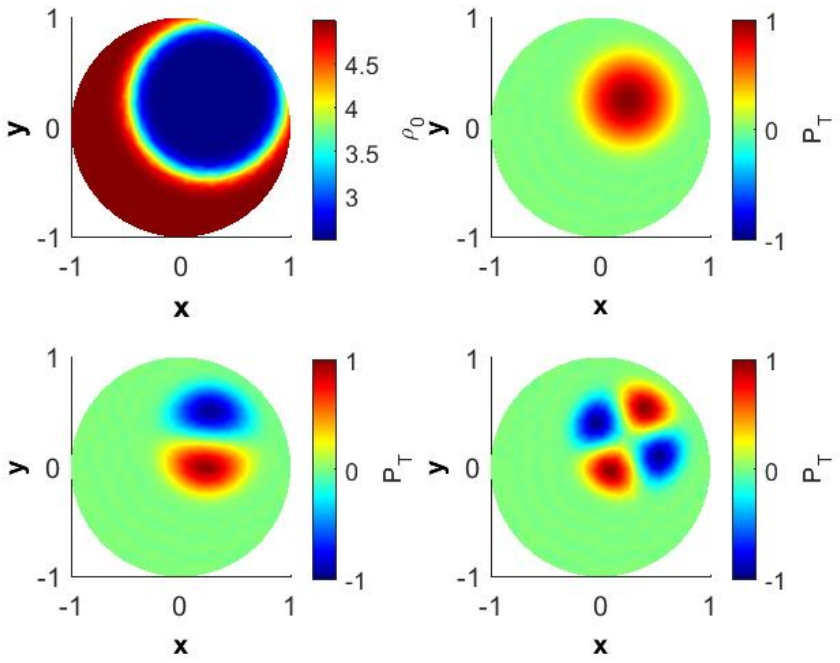

Figure 3.8: The same as in Fig. (3.6) but here the depleted density inhomogeneity is placed along the first bisector. The parameters used for this visualization are given as Case 3.3 in Table (3.2).

This result also proves our initial assumption according to which the Dirichlet boundary condition imposed in our case would not modify qualitatively or quantitatively the solution of dispersion relation obtained in the case of body modes (in line with the recent findings by Aldhafeeri et al. (2022*b*)). For a particular wavenumber, it is clear that the fluting mode is the most sensitive to the variation in size of the waveguide, confirming the results by Albidah et al. (2022*a*).

The upper right and lower panels of Fig. (3.9) shows the variation of dimensionless phase speed for the same slow body modes with respect to kR in the case of density enhancement and depletion, respectively. The three positions of the density inhomogeneity are shown by different colours: concentric (red) and two eccentric cases (green and blue). Similar to the case of uniform plasma, in the enhanced and depleted density distribution we observe the same dispersive character for smaller values of kR and the dimensionless phase speed becoming practically independent of the wavelength of waves for the higher values of kR. Comparing the values of the dimensionless phase speed in the three cases, it is evident that the density enhancement leaves

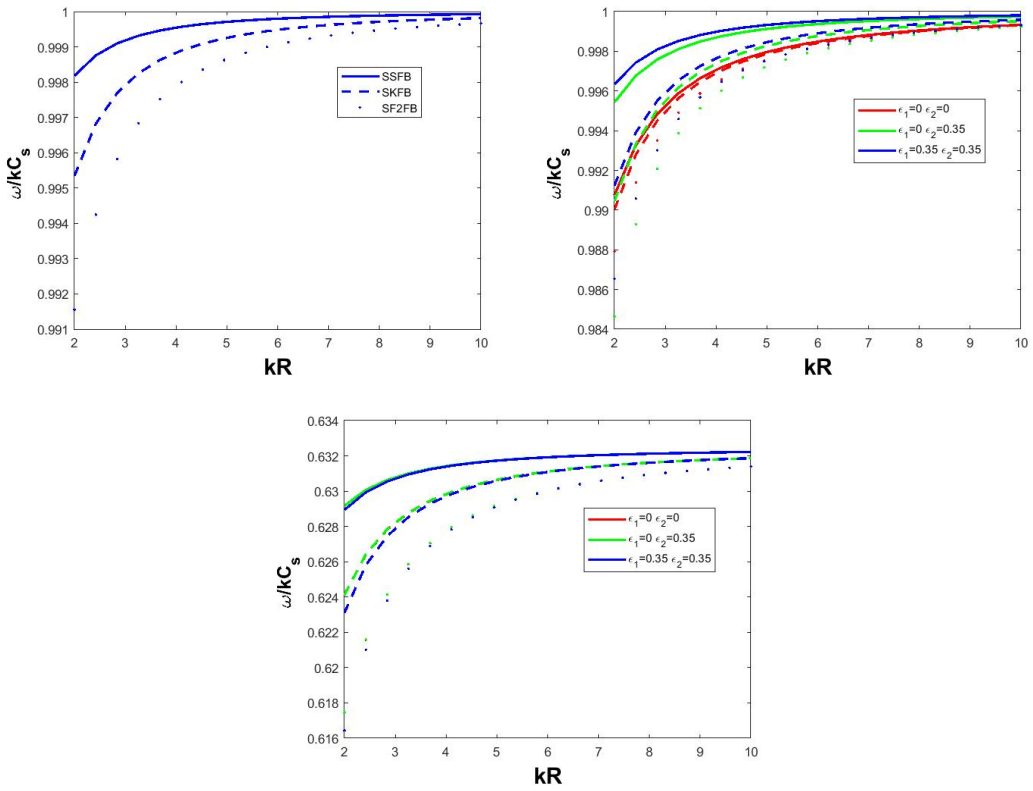

Figure 3.9: The variation of the dimensionless phase speed of slow body waves with the dimensionless wavenumber kR for a uniform loading with $\sigma = 1$ (upper left panel) for the three slow body modes (SSFB, solid blue curve), SKFB (dashed blue curve), SF2FB (dotted blue curve. Upper right panel: the variation of the same quantity in the case of an inhomogeneous density enhancement at three different positions (shown in the legend). Lower panel: the variation of the same quantity for a depleted density inhomogeneity for the same three positions. The values of parameters used in these plots are given as Case 4.1 in Table (3.2).

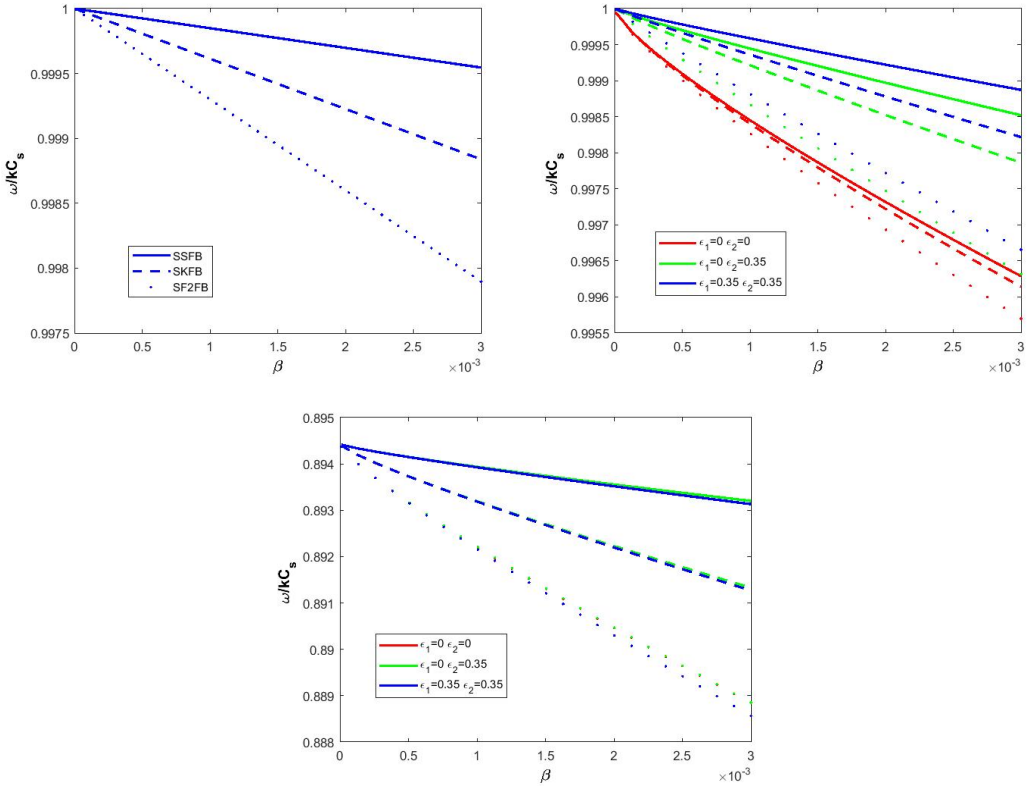

Figure 3.10: The same as in Fig. (3.9), but here we investigate the variation of the dimensionless phase speed with respect to plasma-β. The values of parameters used in these plots are given as Case 4.2 in Table (3.2).

practically the dimensionless phase speed unchanged, while the density depletion brings a more significant reduction in the dimensionless phase speed (of nearly 40%) compared to the homogeneous case. In the case of density enhancement, the concentric distribution of density leads to a much more differentiated behaviour of the dimensionless phase speed, especially in the case of sausage modes. Interestingly, in the depleted density distribution the modes show a larger variation with respect to the position of the density inhomogeneity, however, the distinction of waves' phase speed with regards to the position of the inhomogeneity vanishes. These plots show that once a density inhomogeneity is taken into account, the phase speeds of particular waves become much closer, making them rather difficult to distinguish from one another.

Another important parameter that plays a crucial role in the propagating characteristic of waves is the plasma-β. In the solar photosphere the intensive magnetic field in sunspots or pores makes this parameter very small. Eq (3.19) confirms that the eigenvalues determined for the studied slow waves will also

depend on the plasma-β. Figure (3.10) (upper left panel) shows the variation of the slow waves' dimensionless phase speed with the plasma-β parameter for a homogeneous density ($\sigma = 1$). Clearly, for very low plasma β, the value of ω/kC_S is approximately 1 for all three eigenmodes and corresponds to the value of the phase speed in an unbounded plasma. With the increase of plasma-β, the value of ω/kC_S decreases fairly linearly for all the three eigenmodes, however, these changes are rather small and the most affected mode is the fluting mode of order 2. The upper right and lower panels of Fig. (3.10) show the variation of phase speed for the same slow body modes with respect to the same parameter in the case of density enhancement ($\sigma > 1$) and depletion ($\sigma < 1$). The locations of density inhomogeneity (and the colours used to represent these) are identical to the ones used in Fig. (3.9). Similar to the case of uniform plasma, the variation of the dimensionless phase speed shows the same decreasing pattern with the increase of plasma-β. Similar to the results shown in Fig. (3.9) the density enhancement does not lead to significant changes in the variation of the phase speed, while these changes are more significant in the case of depleted density inhomogeneity. While in the case of density enhancement, there is a clear dependence of the phase speed in terms of the location of the inhomogeneity (the concentric case showing the lowest values), the differentiation of the same mode for the three different locations ceases, practically they are independent on the location of the density inhomogeneity.

Let us now discuss the variation of the dimensionless phase speed of slow waves of different azimuthal order in terms of the parameters describing the density inhomogeneity (cases C4.3.1-C4.6 in Table 3.2). The left panel of Fig. (3.11) shows the variation of ω/kC_S for the three slow body modes in terms of the parameter σ in the case of a density enhancement, with the value of $\sigma = 1$ corresponding to the homogeneous density. As before, the different line styles and colours show different slow body modes and three different positions of density inhomogeneity. With the increase in the value of σ the dimensionless phase speed decreases for all three eigenmodes. This decrease is more pronounced near $\sigma = 1$ and becomes fairly linear for larger values of σ. From the Fig (and all subsequent cases discussed in this study) it is obvious that the fundamental slow sausage mode has the highest propagation speed. For a particular value of σ the differences in the propagation speed of these three waves are very small. The largest modification in the phase

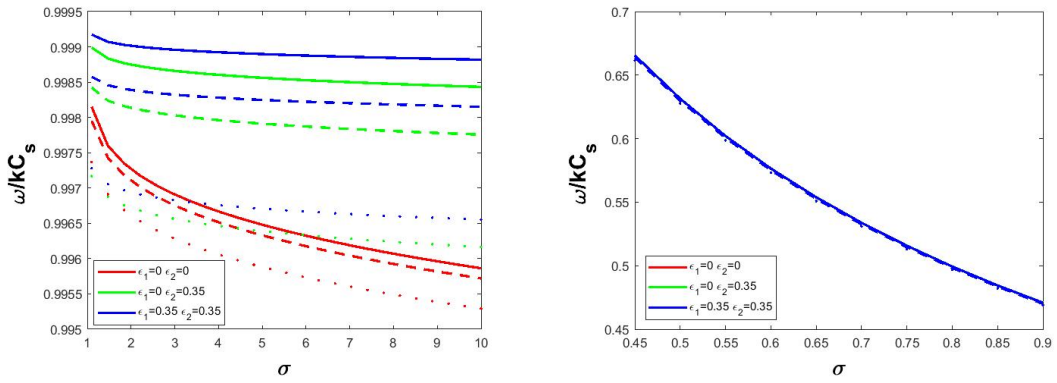

Figure 3.11: The same as in Fig. (3.9), but here we show the variation of the dimensionless phase speed with respect to the parameter σ in the case of a density enhancement (left panel) and density depletion (right panel). The values of parameters used in these plots are given as case C4.3.1 (for the left panel) and case C4.3.2 (right panel) in Table (3.2).

speed of waves occurs in the case of concentric loading, and the changes of this quantity with the strength of inhomogeneity for any eccentric position have little variation.

The right panel of Fig. (3.11) shows the variation of ω/kC_S of slow body modes for a depleted density loading with respect to σ. In contrast to the case of an enhanced density, the dimensionless phase speed of the investigated slow waves shows a much stronger dependence on the value of the density inhomogeneity, however, waves propagate with the same phase speed, regardless of the position of the density depletion, meaning that observationally it would be impossible to distinguish between these waves if we restrict our mode identification based on the propagation speed. The propagation speeds of waves in this case are also independent of the type of waves, all body waves (regardless of their radial order) tend to propagate with the same phase speed.

The variation of the dimensionless phase speed of selected slow body modes with respect to the parameter τ (case C4.4 in Table 3.2), denoting the ratio of the radii of the density inhomogeneity to the radius of the tube, in the case of a density enhancement and depletion, is shown in the two panels of Fig. (3.12). The meaning of different line styles and colours is identical to previous cases. In the case of density enhancement, with the increase in the size of the inhomogeneity, the dimensionless phase speeds decrease very little for eccentric density loading, while the variation of the phase speed in the

case of concentric loading shows the most accentuated variation, however, the distinction of the type of waves ceases. These conclusions are similar to the findings on the variation of the modes' phase speed with the parameter σ. Figure (3.12, right panel) shows the variation of ω/kC_S for the same three slow

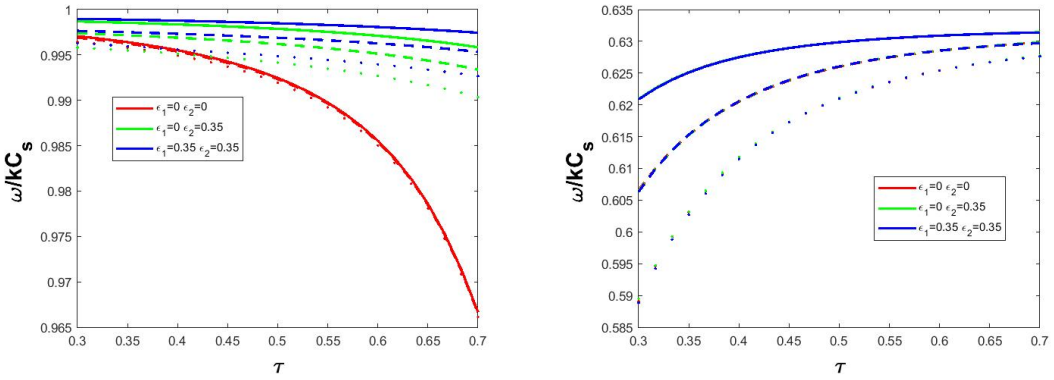

Figure 3.12: The same as in Fig. (3.9), but here we plot the variation of the dimensionless phase speed of different slow body waves in terms of the parameter τ in the case of density enhancement (left panel) and depletion (right panel). The values of parameters used in these plots are given as case C4.4 in Table (3.2).

body modes with respect to the parameter τ when the density inhomogeneity takes a depleted value (see case C4.4 in Table 3.2). With the increase in the size of the inhomogeneous region, the value of ω/kC_S increases, and the variation of the dimensionless phase speed is practically independent of the location of the inhomogeneity. This result has interesting implications, as the location of the inhomogeneous region can be chosen, for modelling purposes, in a position that is most suitable for modelling. In the depleted density case the fundamental sausage mode displays the smallest variation with the ratio of radia, τ. Comparing the two panels of Fig. (3.12) it is obvious that the phase speeds corresponding to a depleted case show a much enhanced variation with τ.

The variation of the dimensionless phase speed of the investigated slow body waves with respect to the smoothness parameter, ξ (see case C4.5 in Table 3.2), is shown in Fig. (3.13) for an inhomogeneous equilibrium density enhancement (left panel) and density depletion (right panel), respectively. In the case of a density enhancement the values of the phase speed decrease for all three modes with the increase in the value of ξ. This decrease is fairly

linear except for sausage modes for concentric loading. As before, for a particular value of ξ, the sausage mode has the highest propagation speed. The phase speed of waves for a concentric density distribution shows the largest variability. On the other hand, in the case of depleted density, the phase speed of waves is much reduced compared to the case of density enhancement and the variation of the dimensionless phase speed for the three modes shows a great degree of independence on the location of the inhomogeneity. The most affected mode remains the fluting and sausage modes. They are practically independent of the change of the smoothness parameter in the case of depleted density.

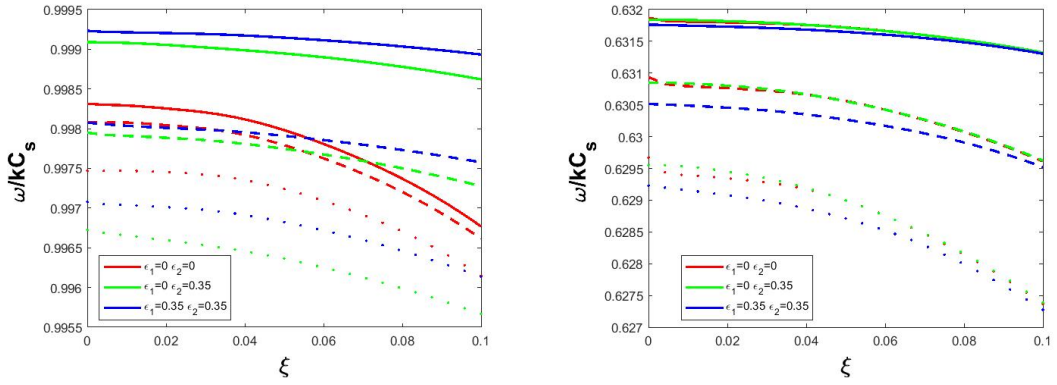

Figure 3.13: The same as in Fig. (3.9), but here we display the variation of the dimensionless phase speed of slow body waves in terms of the smoothness parameter, ξ (see case C4.5 in Table 3.2), in the case of an equilibrium density enhancement (left panel) and depletion (right panel). The values of parameters used in these plots are given as case C4.5 in Table (3.2).

Finally, in Fig. (3.14) we investigate the variation of the dimensionless phase speed for the three investigated slow body modes in terms of the position of the centre of the density inhomogeneity. For this parametric analysis, we let the value of the parameter ϵ_1 (see case C4.6 in Table 3.2) vary in a given interval and choose two particular values of ϵ_2: $\epsilon_2 = 0$ (red curves) and $\epsilon_2 = 0.35$ (green curves). The two panels of Fig. (3.14) represent the cases of density enhancement and depletion, respectively. With the increase in the value of the parameter ϵ_1, the dimensionless phase speed of investigated slow body modes corresponding to a density enhancement increases with the departure from the concentric case, but the difference between the phase speed corresponding to the two particular values of ϵ_2 diminishes with the increase of ϵ_1. It is also

clear that the increase with ϵ_1 is nearly linear when the density inhomogeneity is not along the horizontal axis. For a given value of ϵ_1, the fundamental sausage modes have the highest propagation speed. In the case of depleted density, the dimensionless phase speed of slow body waves shows practically no (or little) variation with the location of the density inhomogeneity, meaning that when modelling the effect of density inhomogeneity on the propagation characteristics of waves we can choose the most convenient location.

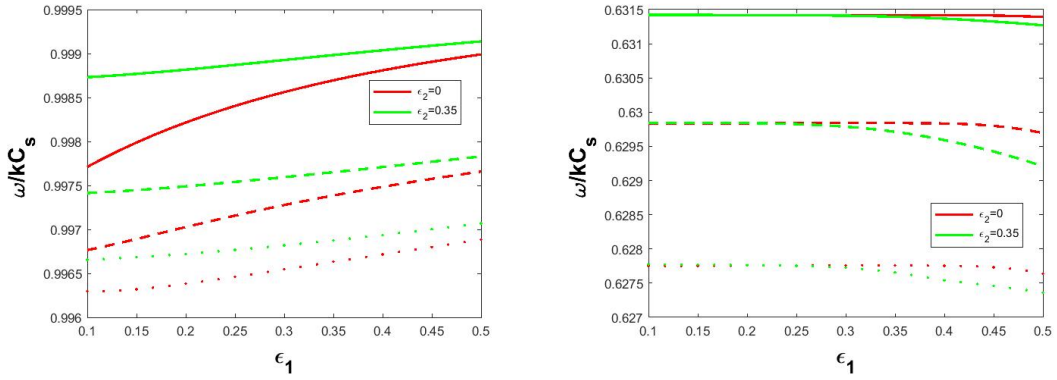

Figure 3.14: The variation of the dimensionless phase speed of slow body waves in terms of the parameter ϵ_1 for two particular values of ϵ_2. The cases of density enhancement and depletion are shown in the right and left panels, respectively. The values of parameters used in these plots are given as case C4.6 in Table (3.2).

It is fairly straightforward to check why slow body modes in the presence of density inhomogeneity become localised. Slow body modes appear as long as the coefficient of the last term of Eq. (3.19) is positive. When this term turns negative, normally we would have surface (evanescent) solutions, however in our case the surface wave solution cannot be applied since we use Dirichlet boundary conditions b.c., i.e. the amplitude of perturbations is expected to be zero at the boundary. For particular combinations of density parameters, there are regions where the coefficient of the last term of Eq. (3.19) turns negative (evanescent solutions). Hence, we will not have an oscillatory solution, as shown in the Fig. (3.15).

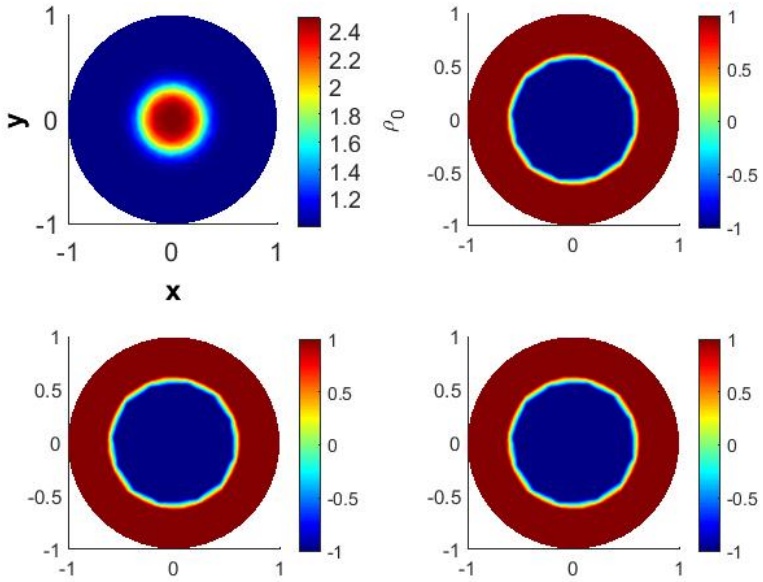

Figure 3.15: The sign of the last term in Eq. (3.19) corresponding to a concentric density enhancement (upper left panel). Solutions of the Sturm-Liouville equation are considered only when the sign of this term is positive. Here we show the value of this term in the case of the three investigated modes.

3.5 Slow body waves in the long wavelength limit

The modification of the properties of waves and their spatial structure can also be investigated in the other limit, corresponding to the long wavelength case, i.e. when the wavelength of waves is much larger than the radius of the waveguide. According to the results by Edwin and Roberts (1983*b*) slow body modes in the long wavelength limit ($kR \ll 1$) propagate with a phase speed close to the internal tube speed, C_T. Using the same technique of reducing the governing equation (3.11), with $m_0^2 = -n_0^2 < 0$ as before, we assume that the phase speed of waves can be written as $\omega^2 = k^2 C_T^2 (1+\nu)$, where ν is a small positive constant, so $\nu = \omega^2/(k^2 C_T^2) - 1$. Following the same procedure as presented in the limit of short wavelengths the governing equation for the total pressure perturbation becomes

$$\frac{\partial}{\partial r}\left(r\frac{\partial P_T}{\partial r}\right) + \frac{1}{r}\frac{\partial^2 P_T}{\partial \theta^2} + (kR)^2 \frac{2\gamma\beta}{(\gamma\beta+2)^2\left(\frac{\omega^2\chi}{k^2C_T^2}-1\right)} r P_T = 0, \qquad (3.37)$$

where $\chi(r,\theta)$ has been defined earlier in Eq. (3.16) and the quantity $\omega/kC_T = V_{ph} = \lambda$ is the dimensionless phase speed of waves and constitutes the eigenvalue of this problem.

To obtain the eigenvalues associated with this equation, we would rearrange the equation as

$$(\lambda^2\chi)\left[\frac{\partial}{\partial r}\left(r\frac{\partial P_T}{\partial r}\right)+\frac{1}{r}\frac{\partial^2 P_T}{\partial\theta^2}\right]-\left[\frac{\partial}{\partial r}\left(r\frac{\partial P_T}{\partial r}\right)+\frac{1}{r}\frac{\partial^2 P_T}{\partial\theta^2}\right]+D_1 r P_T=0, \tag{3.38}$$

where we introduced the notation $D_1 = (kR)^2\frac{2\gamma\beta}{(\gamma\beta+2)^2}$.

3.5.1 Description of the numerical method

The particular form of the governing equation (3.38) requires a different numerical approach to determine the eigenvectors and associated eigenvalues. For our governing equation we are going to employ the Galerkin FEM method with Dirichlet boundary condition, i.e. $P_T = 0$ at $r = 1$. Most of the necessary MATLAB algorithms use Cartesian coordinates, therefore, it is more convenient to transform the governing equation (3.38) into Cartesian coordinates using the standard connection between the Cartesian coordinates (x, y) and the polar coordinates (r, θ). After some straightforward calculations, the governing equation for the total pressure (3.38) can be rearranged into a more suitable form

$$\left[\lambda^2\chi\left(\frac{\partial^2}{\partial x^2}+\frac{\partial^2}{\partial y^2}\right)-\left(\frac{\partial^2}{\partial x^2}+\frac{\partial^2}{\partial y^2}\right)+D_1\right]u=0, \tag{3.39}$$

where the eigenfunction u denotes total pressure perturbation, P_T. Comparing this equation with the governing equation (3.38), it is easy to see the link between the ways we write the derivatives for the two equations.

The computational domain is discretized using linear combinations of the small triangular finite elements. Each element is connected to another through nodes. In general, the number of nodes present in an element depends on the polynomial approximation used for the element. For linear and quadratic approximations, the triangular element has 3 and 6 numbers of nodes, respectively, as shown in Fig. 3.16. For the present study we use small triangular

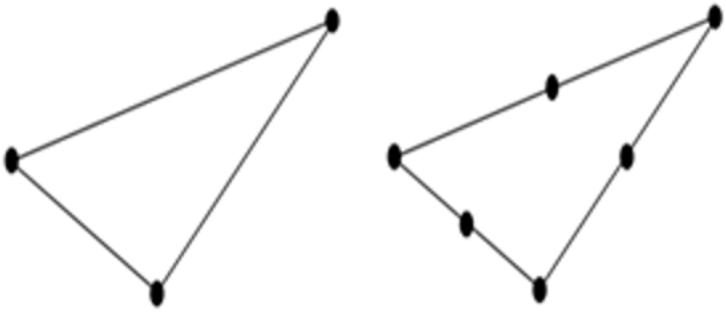

Figure 3.16: The triangular elements used to discretise the numerical domain: 2D linear triangular element (left panel) and 2D quadratic triangular element (right panel).

elements which contain three nodes at the vertices of the triangle and the interpolation variable (our eigenfunction), u, within the element is linear in x and y. Equation (3.39) needs to be solved for each and every node of the computational domain.

The eigenfunction, u, is written as the sum of orthogonal piecewise polynomial basis functions whose coefficient must satisfy the differential equation. Let us assume that the unknown function, u, can be written as

$$u = a_1 + a_2 x + a_3 y = \begin{bmatrix} 1 & x & y \end{bmatrix} \begin{bmatrix} a_1 \\ a_2 \\ a_3 \end{bmatrix}, \tag{3.40}$$

where the generalized coefficients a_i $(i = 1, 2, 3)$ are the constants to be determined. The above interpolation function should be represented in terms of the nodal variables (u_1, u_2, u_3) at the three nodal points having the coordinates $(x_1, y_1), (x_2, y_2), (x_3, y_3)$. Therefore, substituting them into Eq. (3.40), yields

$$\begin{bmatrix} u_1 \\ u_2 \\ u_3 \end{bmatrix} = \begin{bmatrix} 1 & x_1 & y_1 \\ 1 & x_2 & y_2 \\ 1 & x_3 & y_3 \end{bmatrix} \begin{bmatrix} a_1 \\ a_2 \\ a_3 \end{bmatrix}. \tag{3.41}$$

As we would like to determine the values of the generalized coefficients, these

are given by inverting the coefficient matrix to obtain

$$\begin{bmatrix} a_1 \\ a_2 \\ a_3 \end{bmatrix} = \frac{1}{2A} \begin{bmatrix} x_2y_3 - x_3y_2 & x_3y_1 - x_1y_3 & x_1y_2 - x_2y_1 \\ y_2 - y_3 & y_3 - y_1 & y_1 - y_2 \\ x_3 - x_2 & x_1 - x_3 & x_2 - x_1 \end{bmatrix} \begin{bmatrix} u_1 \\ u_2 \\ u_3 \end{bmatrix}, \tag{3.42}$$

where

$$A = \frac{1}{2} det \begin{bmatrix} 1 & x_1 & y_1 \\ 1 & x_2 & y_2 \\ 1 & x_3 & y_3 \end{bmatrix}.$$

Substitution of Eq. (3.42) back into Eq. (3.41) allows us to express the unknown trial function in terms of nodal variables u_1, u_2 and u_3 instead of a_1, a_2 and a_3. The linear triangular element approximations need to be related with the differential equation using some suitable function. These functions are called shape functions (denoted by H), basis functions or interpolation functions. The shape function depends on the type of element as well as the polynomial approximation used for the element. As a result, we can write

$$u = \begin{bmatrix} H_1 & H_2 & H_3 \end{bmatrix} \begin{bmatrix} u_1 \\ u_2 \\ u_3 \end{bmatrix}. \tag{3.43}$$

For each node of an element the equation for shape function is different. For the linear triangular elements with three nodes, the shape functions for each nodes are given by

$$\begin{aligned} H_1 &= \frac{1}{2A} \left((x_2y_3 - x_3y_2) + (y_2 - y_3)\, x + (x_3 - x_2)\, y \right), \\ H_2 &= \frac{1}{2A} \left((x_3y_1 - x_1y_3) + (y_3 - y_1)\, x + (x_1 - x_3)\, y \right), \\ H_3 &= \frac{1}{2A} \left((x_1y_2 - x_2y_1) + (y_1 - y_2)\, x + (x_2 - x_1)\, y \right). \end{aligned} \tag{3.44}$$

To obtain the complete solution over the whole domain, all the finite elements need to be integrated for the given differential equation. The shape functions also satisfy the conditions $H_i(x_j, y_j) = \delta_{i,j}$ and $\sum_{i=1}^{3} H_i = 1$, where $\delta_{i,j}$ is the Kronecker delta symbol and x_i and y_i are the coordinate values at the i^{th} node and u_i is the nodal variable.

Equation (3.39) needs to be solved for each and every node of the computa-

tional domain. Applying the finite element method, the first step is to convert the original governing differential (strong) form of the Partial differential equation into an integral (weak) form by multiplying with a test (weight) function denoted by w and integrating over the circular domain (Ω) that reflects the circular sunspot (more details can be found in Kwon and Bang (2018)).

$$\int_{\Omega} -w\frac{\partial^2 u}{\partial x^2}\partial\Omega + \int_{\Omega} -w\frac{\partial^2 u}{\partial y^2}\partial\Omega + \int_{\Omega} wD_1 u\partial\Omega + \int_{\Omega} w\chi\lambda^2\left(\frac{\partial^2 u}{\partial x^2} + \frac{\partial^2 u}{\partial y^2}\right)\partial\Omega = 0. \tag{3.45}$$

In Eq. (3.45), D_1 is a constant and the elements of the domain are such that in each domain (Ω^e) the value of χ can be considered constant, so these quantities can be taken out of the integral (since they are known and calculated numerically based on the discretization of the domain). Using an integration by part over the domain of triangular elements, Ω^e, and taking into account that on the boundary the eigenfunction vanishes, consequently the boundary integral is zero. Hence, the integral equation (3.45) transforms into

$$\int_{\Omega^e} \frac{\partial w}{\partial x}\frac{\partial u}{\partial x}\partial\Omega^e + \int_{\Omega^e} \frac{\partial w}{\partial y}\frac{\partial u}{\partial y}\partial\Omega^e + D_1\int_{\Omega^e} wu\partial\Omega^e$$

$$-C_1\lambda^2\left(\int_{\Omega^e} \frac{\partial w}{\partial x}\frac{\partial u}{\partial x}\partial\Omega^e + \int_{\Omega^e} \frac{\partial w}{\partial y}\frac{\partial u}{\partial y}\partial\Omega^e\right) = 0. \tag{3.46}$$

where C_1 is χ. We have considered the test functions (w) as shape functions of the trial function and, thus, the test functions for Galerkin's method are $w_i = H_i$. Substitution of these shape functions back into Eq. (3.46) with element discretisation results in an element matrix which is given by

$$(1-C_1\lambda^2)\left[\int_{\Omega^e} \mathbf{H}_x\mathbf{H}_x^T d\Omega^e + \int_{\Omega^e} \mathbf{H}_y\mathbf{H}_y^T d\Omega^e\right]\mathbf{u} + D_1\int_{\Omega^e} \mathbf{H}\mathbf{H}^T d\Omega^e\mathbf{u} = 0, \tag{3.47}$$

where

$$\mathbf{H} = \begin{bmatrix} H_1 \\ H_2 \\ H_3 \end{bmatrix}, \quad \mathbf{u} = \begin{bmatrix} u_1 \\ u_2 \\ u_3 \end{bmatrix}, \quad \mathbf{H}_x = \begin{bmatrix} \frac{dH_1}{dx} \\ \frac{dH_2}{dx} \\ \frac{dH_3}{dx} \end{bmatrix}, \quad \mathbf{H}_y = \begin{bmatrix} \frac{dH_1}{dy} \\ \frac{dH_2}{dy} \\ \frac{dH_3}{dy}, \end{bmatrix},$$

and the superscript T denotes the transpose. Using the particular shapes of

the elements, the first derivatives of the shape functions can be calculated as

$$\begin{bmatrix} \frac{dH_1}{dx} \\ \frac{dH_2}{dx} \\ \frac{dH_3}{dx} \end{bmatrix} = \begin{bmatrix} y_2 - y_3 \\ y_3 - y_1 \\ y_1 - y_2 \end{bmatrix}, \qquad \begin{bmatrix} \frac{dH_1}{dy} \\ \frac{dH_2}{dy} \\ \frac{dH_3}{dy} \end{bmatrix} = \begin{bmatrix} x_3 - x_2 \\ x_1 - x_3 \\ x_2 - x_1 \end{bmatrix}. \tag{3.48}$$

Since the first order derivatives of the shape functions are constants, they can be taken out from the integral in Eq. (3.47). Our relation can be further simplified using the well-known relation

$$M^e = \int_{\Omega^e} \mathbf{H}\mathbf{H}^T d\Omega^e = \frac{A}{12} \begin{bmatrix} 2 & 1 & 1 \\ 1 & 2 & 1 \\ 1 & 1 & 2 \end{bmatrix}. \tag{3.49}$$

After substituting Eq. (3.49) back into Eq. (3.47), we obtain

$$\mathbf{H}_x\mathbf{H}_x^T A\mathbf{u} + \mathbf{H}_y\mathbf{H}_y^T A\mathbf{u} + D_1 M^e\mathbf{u} - C_1\lambda^2\mathbf{H}_x\mathbf{H}_x^T A\mathbf{u} - C_1\lambda^2\mathbf{H}_y\mathbf{H}_y^T A\mathbf{u} = 0$$

$$(a_1)_{3*3}\mathbf{u} + (a_2)_{3*3}\lambda^2\mathbf{u} = 0 \tag{3.50}$$

where $(a_1)_{3*3}$ and $(a_2)_{3*3}$ represent the local stiffness matrices for each element and they are given as

$$(a_1)_{3*3} = \mathbf{H}_x\mathbf{H}_x^T A + \mathbf{H}_y\mathbf{H}_y^T A + D_1 M^e, \quad (a_2)_{3*3} = -C_1\lambda^2\mathbf{H}_x\mathbf{H}_x^T A - C_1\lambda^2\mathbf{H}_y\mathbf{H}_y^T A. \tag{3.51}$$

Each local stiffness matrix contains an equation for each node in the element, the so-called local equation. The global stiffness matrices are obtained by assembling all of the local stiffness matrices or by organising all of the local equations for each node as

$$(A_2)_{N*N}\lambda^2 \begin{bmatrix} u_1 \\ \vdots \\ u_N \end{bmatrix} + (A_1)_{N*N} \begin{bmatrix} u_1 \\ \vdots \\ u_N \end{bmatrix} = 0, \tag{3.52}$$

therefore we have that $A_1 u + A_2\lambda^2 u = 0$.

In the present study a new algorithm is developed to obtain the eigenvalues and eigenvectors of a quadratic matrix polynomial using Galerkin FEM and QZ factorization. The method is potentially capable of handling a variety of

eigenvalue problems in the most efficient way. The built-in MATLAB function '$polyeig(A_1, A_2)$' (based on the QZ factorization) is used to obtain the generalized quadratic eigenvalues and eigenvectors. The code is tested against the eigenvalues obtained for the uniform circular cross sectional magnetic flux tubes.

3.5.2 Results

As we are dealing with slow body waves in the long wavelength limit, the phase speed of waves will be normalised by the tube speed, C_T, while the radial variation of the density is described by Eq. (3.16). The spatial distribution of the eigenfunction for the three investigated modes in the case of a homogeneous plasma equilibrium density ($\sigma = 1$) is identical to the one shown in Fig. (3.2), however, given the particularity of the limit we are using, the dimensionless phase speed of modes will be slightly larger than 1. In our analysis we use the constant value of plasma-$\beta = 3 \times 10^{-3}$, and dimensionless wavenumber $kR = 0.5$. The characteristic values of the parameters used for obtaining the numerical solutions are provided in Table (3.3). As before, the colour bar represents the relative magnitude of the dimensionless amplitude of the total pressure perturbation so that red and blue shaded regions correspond to the crests (maxima) and valleys (minima) of the amplitude of P_T. The dimensionless phase speeds of slow body modes exhibit a very little variation with the density parameters and their variation is phenomenologically identical with the solutions we obtained in the short wavelength limit. As before, the fluting mode has the highest sensitivity to the density parameters. Similar to the short wavelength limit, the equilibrium density inhomogeneity (enhancement and depletion) will be placed in a concentric and eccentric location and the results are displayed in Figs. (3.17)-(3.20).

In the case of slow body waves propagating in an inhomogeneous cylindrical flux tube in the long wavelength limit the most remarkable change occurs in the morphology (the spatial structure) of modes. When the equilibrium density appears as a localised concentric enhancement Fig. (3.17) the fundamental sausage clearly maintains its global character and the spatial structure of these modes appears similar to the one we obtained in the homogeneous density case, therefore fundamental sausage modes are very weakly affected both in propagation speed (or frequency) and the spatial structure of waves.

Table 3.3: Details of the physical parameters used for the numerical modeling and analysis of slow body MHD modes in a circular flux tube, assuming a model with constant plasma-$\beta = 3 \times 10^{-3}$, in the long wavelength limit ($kR = 0.5$).

	σ	τ	ξ	ϵ_1	ϵ_2
C1: Non-uniform density enhancement					
C1.1: - concentric	2.5	0.3	4.1×10^{-2}	0	0
C1.2: - right eccentric	-	-	-	0.5	0
C2: Non-uniform density depletion					
C2.1: - concentric	0.5	0.7	-	0	0
C2.2: - right eccentric	-	-	-	-	0.5

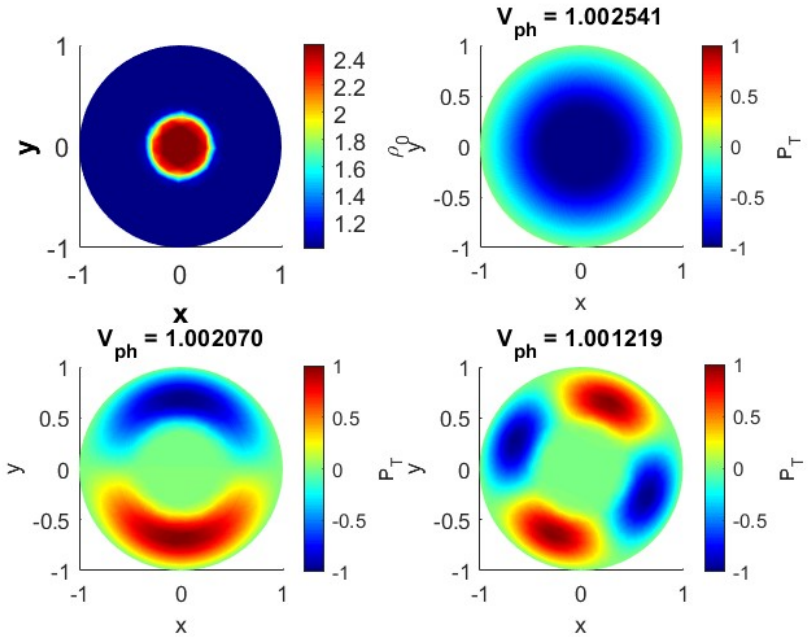

Figure 3.17: The spatial structure of SSFB, SKFB, and SF2FB modes under photospheric conditions in a circular magnetic flux tube with concentric density enhancement in the long wavelength limit. The colour bars display the magnitude of the total pressure perturbation amplitude divided by its maximum value. The red and blue shaded regions represent crests (maxima) and valleys (minima) of amplitude variation of total pressure perturbation. The density distribution is shown in the upper left panel and the radial variation of the density is given by Eq. (3.16). All characteristic values of parameters used in these numerical solutions are given in Table (3.3), case C1.1.

This clearly contrasts the results obtained in the case of slow body modes in the short wavelength limit Fig. (3.3). While the spatial structure of fundamental kink modes in the long and short wavelength limit behave the same, the fluting mode has a peculiar behaviour as the regions that correspond to the enhanced density show an oscillatory motion with suppressed amplitude and the maximum amplitude in the eigenfunction appears to be the regions in the homogeneous annulus surrounding the density inhomogeneity. That means that these modes appear to remain global modes, however the weight of different regions to the global oscillating mode is changing.

The spatial structure of the same three slow body modes in the case of an eccentric density enhancement is shown in Fig. (3.18) while the values of the physical parameters describing the inhomogeneous density (placed along the horizontal direction) are given by case C1.2 in Table (3.3). When compared to the results obtained in the short wavelength limit (Fig. 3.4), the investigated slow body modes show a completely different behaviour. Although the symmetry of the modes is distorted, waves remain global in the sense that the whole cross-section of the flux tube oscillates. As before, the amplitudes in the total pressure are higher in regions of lower (homogeneous) density.

These results may allow us to conclude that slow body modes propagating with larger wavelengths than the radius of the flux tube under photospheric conditions in the presence of an eccentrically placed density inhomogeneity maintain their global character, however they lose their symmetry.

When the equilibrium density appears as a region of depleted density, the behaviour of long wavelength slow body modes investigated by us appear to have the same symmetry and the same character as waves in the short wavelength limit and that is evidenced by the spatial structure of waves shown in Figs. (3.19) and (3.20) that cover the cases of a concentric and eccentric density loading. As before, the extent of the spatial domain where modes are present is smaller than the spatial extent of the density inhomogeneity.

Finally we should mention that the spatial structure of the investigated modes when the density inhomogeneity is placed along the first bisector is identical with the cases shown above.

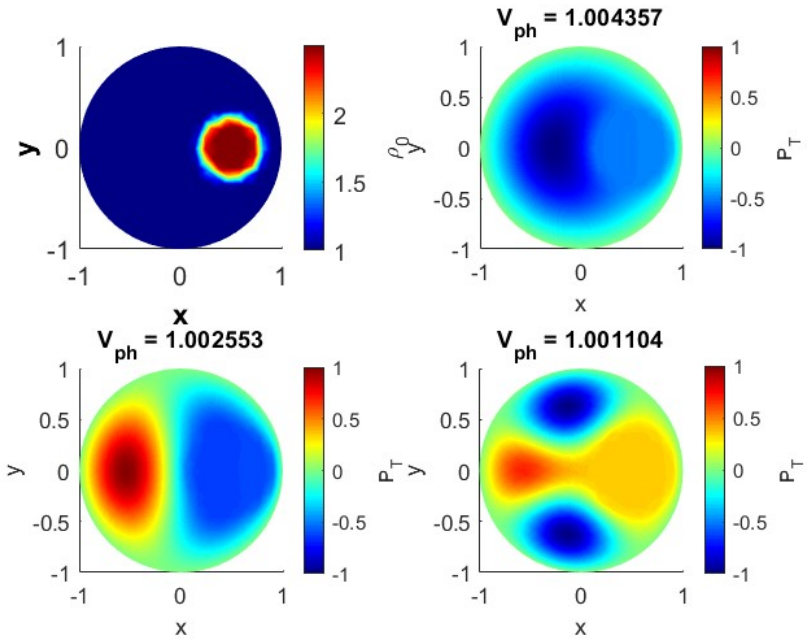

Figure 3.18: The same modes as in Fig. (3.17), but here the density loading is eccentric, and is situated along the horizontal direction. The values of the parameters used in this case are given in Table (3.2), case C1.2.

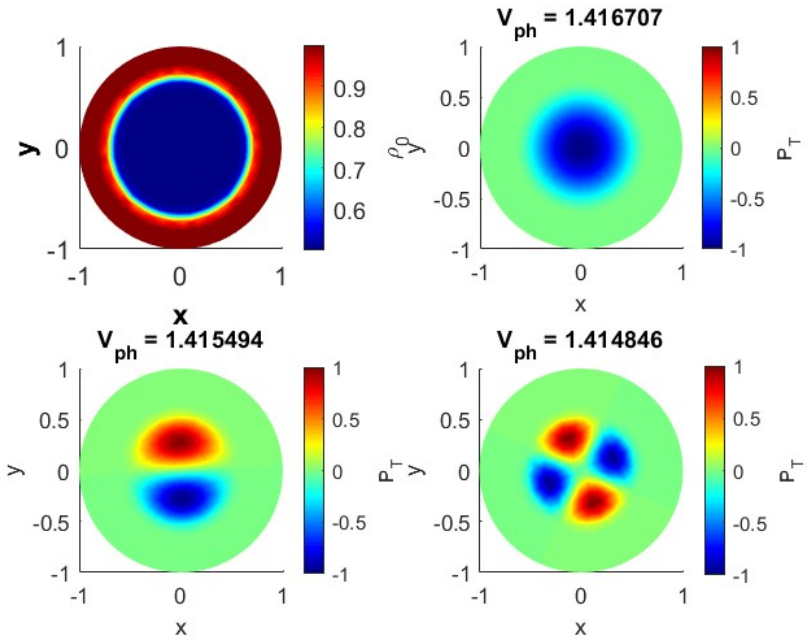

Figure 3.19: The same as in Fig. (3.17) but in the case of depleted concentric equilibrium density inhomogeneity. The values of the parameters used in this case are given in Table (3.2), case C2.1.

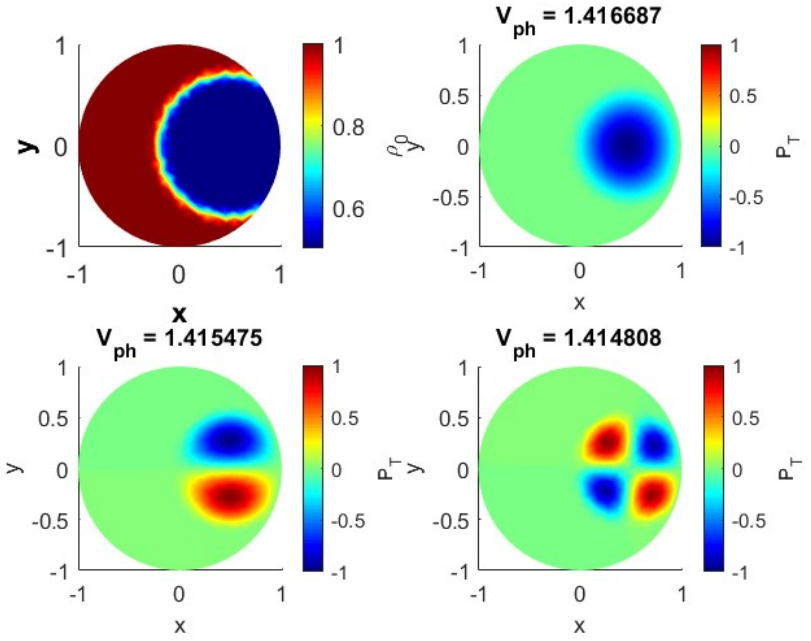

Figure 3.20: The same as in Fig. (3.17), but here the depleted density region is situated in an eccentric position along the horizontal axis. The values of the parameters used in this case are given in Table (3.2), case C2.2.

3.6 Conclusions

Intense magnetic waveguides in the solar photosphere, such as pores and sunspots are ideal environments for the propagation of guided waves. The theory developed by Edwin and Roberts (1983*a*) predicts the qualitative behaviour of different waves in such environments assuming an ideal case when the plasma is homogeneous, without background flows, and unbounded along the symmetry axis of the magnetic flux tube. High-resolution observations show that these restrictions are not realistic and the theory of guided MHD waves must be expanded to account for the presence of, e.g. density inhomogeneity.

High resolution magnetic and intensity observations (e.g. SoHo/MDI, SDO/HMI, etc.) showed that sunspots and pores are inhomogeneous both in magnetic field and density. These inhomogeneities can alter the frequency of waves and their propagation speed leading to a real challenge to identify the nature of waves and their properties. The study summarised in this Chapter investigates the modification of the properties of waves (their spatial structure, phase speed

or frequency, in particular) in the presence of a symmetric and geometrically well-defined inhomogeneity.

In order to tackle the problem mathematically we employed results previously obtained by Aldhafeeri et al. (2022*b*), who showed that in the case of slow body waves under photospheric conditions the dispersive character of waves and their properties can be confidently described by solving a Helmholtz equation with Dirichlet boundary condition. In addition, we assumed particular situations when the wavelength of waves is much smaller (or much longer) than the radius of the tube (short/long wavelength limit). The eigenfrequency as well as the eigenfunction of waves were studied as a Sturm-Liouville eigenvalue problem and the governing equation with non-constant coefficients was solved numerically using the Fourier-Chebyshev spectral, and Galerkin FEM methods, respectively.

The inhomogeneous equilibrium plasma density considered here was described with the help of a series of parameters that defined the shape, location, size and strength of the inhomogeneity. In our study we conducted a parametric analysis to highlight what effects these parameters have on the characteristics of waves. The advantage of the density profile given by Eq. (3.16) is its versatility for modeling purposes. In order to provide a general approach, we have considered both cases of an enhanced and depleted equilibrium plasma density. Since our model assumed a photospheric waveguide where the equilibrium plasma pressure is constant, these equilibrium density enhancements and depletions would appear as cooler (darker) and hotter (brighter) regions inside a magnetic waveguide.

First, we analysed the case of short wavelength limit, i.e. when the wavelength of slow body waves under photospheric conditions is much smaller than the radius of the tube (wide tube). In this limit we expect (inspired from the results by Edwin and Roberts (1983*b*)) that the phase speed of waves is slightly less than the sound speed. Our results indicate that a significant change driven by the inhomogeneous equilibrium plasma density is the modification in the spatial structure of waves. A direct consequence of the particular density distribution is that slow body waves in cylindrical waveguides lose their global character, instead, they become more localized and always tend to appear in the regions that correspond to a lower density. This property might help identify locations of density inhomogeneity when these are not visible in intensity spectral lines.

The parameters that describe the equilibrium plasma density modification (strength, location, size, smoothness of the transition to a homogeneous density) affect the modes in different ways. In general, the eigenfrequencies of fluting modes are more sensitive to the modifications of the equilibrium plasma density parameters. In the case of depleted density, the modifications in the phase speed of waves is more important (nearly 40% decrease) and the differentiation between different modes according to the size of the inhomogeneity or its location very often is very small, meaning that for modeling purposes one can choose the most convenient location for equilibrium plasma density inhomogeneity.

In the long wavelength limit (when the phase speed of slow waves approaches the internal tube speed, slender tube) the changes in the phase speed of waves is small, similar to the changes we had in the short wavelength limit. However, in this limit the most important change is in the modifications in the spatial structure of modes. In this limit (for an enhanced density inhomogeneity) waves remain global in nature, however they lose their symmetry. These findings can lead us to conclude that, in contrast to the short-wavelength limit, the spatial structure of the slow-body modes in the long-wavelength limit exhibits less alterations because of the variations in the phase velocity of the slow-body modes vary slightly over the long wavelength limit. When the inhomogeneous equilibrium density presents itself as a depleted region, the spatial structure of waves is similar to the results found in the short wavelength limit.

The analysis and the numerical recipe in this study can be considered as a starting point in the investigation of waves in realistic solar photospheric waveguides, where the equilibrium plasma density inhomogeneity derived from observations or realistic sunspot simulations can be incorporated in the study of the properties of slow body waves. The present analysis can be considered as a tool for diagnosing the inhomogeneous character of sunspots or pores, however this diagnosis is rather qualitative, rather than quantitative. The choice of a waveguide of high symmetry is not entirely realistic, however it allows us to use a fairly simple mathematical approach and the obtained results show the modifications of the properties of waves due solely to the density inhomogeneity. It is known (see, e.g. Albidah et al., 2021*b*, 2022*b*) that the irregular shape of the waveguides has very strong effects on the spatial structure of waves, especially in the case of higher order modes. The constant plasma-β limit considered here is also a rather crude approximation. Observations show

(see, e.g. Gary, 2001; Grant et al., 2018) that the plasma-β changes over small spatial scales, and around the density inhomogeneities this quantity may exhibit a sharp gradient that could influence the property of waves studied in this Thesis.

CHAPTER 4

Slow body MHD waves in photospheric flux tubes in the presence of local density, pressure and magnetic field inhomogeneity

4.1 Introduction

The magnetic field that permeates plasma actually has a major role in structuring the plasma in the solar environment. Possible magnetic waveguides where MHD waves can propagate are created by these regions of inhomogeneities. Inhomogeneities in the plasma and magnetic field are known to strongly influence the properties of waves, leading to the modifications in the spectral properties of waves, wave amplification, mode conversion, etc. (e.g. De Pontieu et al. (2022),Morton et al. (2011*b*), Stangalini et al. (2022), Aldhafeeri et al. (2022*b*), Skirvin et al. (2022*b*) to name but a few). For the purpose of moving mass and energy from the lower layers of the solar atmosphere to the top layers, these waveguides offer a natural pathway. Sunspots, pores, spicules, prominences, and coronal loops are a few examples of magnetic waveguides that are frequently seen in the solar atmosphere. Most of the time, a boundary can be found in the magnetic field strength or in intensity data that are somehow connected to a jump in the plasma density. Inhomogeneities in the magnetic field or density pose a serious challenge when describing the properties of waves, because the equations that one has to solve, will have inhomogeneous (i.e. coordinate-dependent) coefficients. On the other hand, traversal inhomogeneities are necessary requirements to describe the plasma heating by waves, i.e. the effectiveness of transferring waves' kinetic energy into heat requires strong inhomogeneities (see the very large number of studies on phase mixing, resonant absorption or turbulence).

The problem of MHD wave propagation in inhomogeneous plasmas was examined in details by many authors. The most simplistic and natural inhomogeneity is the one conferred by the gravitational stratification that, in the case of an isothermal plasma, leads to an evolutionary equation of slow MHD waves described by a Klein-Gordon differential equation (see, e.g. Rae and Roberts, 1982; Kalkofen et al., 1994; Sutmann et al., 1998; Ballai et al., 2006; Goedbloed et al., 2010, 2019; Roberts, 2019). This sort of inhomogeneity is known to modify the properties of waves in many ways, for instance the appearance of cut-off frequencies (the stratified atmosphere plays the role of a low-frequency filter), the increase in the amplitudes of waves due to the decay of density and their evolution into shocks that could heat the non-magnetic atmosphere, etc. When the inhomogeneity is present in the transversal direction (e.g. the radial direction of a flux tube) the nature of waves' spectrum is modified in the sense that the spectrum of slow and Alfvén waves becomes continuous, while the spectrum of fast waves remain a discrete one. When the frequency of an externally impinging wave matches one of the frequencies in the continuum spectrum, resonant absorption or phase mixing is taking place that are very efficient ways to damp waves' energy. In this case the governing equations become singular and the values of eigenfunction can be determined by using, e.g. Frobenius series (see, e.g. Sakurai et al., 1991*b*; Goossens et al., 1992; Soler et al., 2017; Pagano et al., 2020). More recently resonant absorption was proposed as the mechanism responsible for damping of kink oscillations of coronal loops when the global standing kink waves are resonantly coupled with local Alfvén waves (Ruderman and Roberts, 2002; Tomczyk et al., 2007; Van Doorsselaere et al., 2008; Morton et al., 2015, 2019).

It is commonly recognised that the magnetic fields that permeate the whole solar atmosphere and its structures are the primary cause of the atmosphere's extreme non-uniformity (e.g. Williams et al., 2020). The plasma and field inhomogeneities have a significant impact on how MHD waves propagate and are observed. The study by Skirvin et al. (2021, 2022*a*) demonstrated that the eigenvalues for trapped wave modes vary depending on the scale of inhomogeneity in an inhomogeneous plasma equilibrium. The permissible bands within which MHD waves can travel get smaller if the plasma is substantially non-uniform, whereas the continuum areas, where physical damping processes might occur, span a larger range of phase speeds. The spatial distributions of observable eigenfunctions generated by MHD wave propagation can also be

impacted by the non-uniform equilibrium. Large density inhomogeneities were shown to have a greater impact on slow body modes in coronal slab structures. This also holds true for body modes in photospheric structures.

Very often, in order to perform a mathematical analysis of wave propagation and solve the governing equation, the inhomogeneous equilibrium has to be rather specific so that the complexity is reduced. One typical example was used earlier in Chapter 3 where we assumed that the plasma-β is constant. A similar approach will be applied in this chapter, too, where we will assume that the inhomogeneity in all the equilibrium physical quantities (magnetic field, pressure, density) is such that the plasma remains isothermal, i.e. the plasma pressure and density vary following the same dependence on coordinates.

The current analysis and the numerical recipe that is developed and used to solve the governing equation can be viewed as a follow-up attempt in the exploration of waves in realistic solar photospheric waveguides, where equilibrium density profile inhomogeneity generated from observations can be incorporated in the study of the property of slow body waves.

4.2 Equilibrium magnetic field

Our analysis will focus on the modifications in the spatial structure and propagation speed of guided slow body MHD waves in a circular magnetic flux tube when all equilibrium parameters (density, pressure, magnetic field) have radial and azimuthal dependence, i.e. they depend on the r and θ coordinates. As before, our investigation will make use of the result that slow body modes correspond to those perturbations for which the total pressure becomes almost zero near the boundary of the waveguide, as shown by Aldhafeeri et al. (2022*a*). In this case the slow body waves under photospheric conditions, the dispersive character of waves and their properties can be confidently described by solving a Helmholtz type partial differential equation with Dirichlet boundary condition, i.e. the total pressure perturbation vanishes at the boundary of the waveguide. For the specific inhomogeneity we consider here the sound speed is going to be a constant quantity, i.e. we are dealing with an isothermal magnetic flux tube.

Let us consider that the equilibrium plasma density has a dependence of the form given by Eq. (3.16), therefore the equilibrium plasma pressure inhomogeneity will be represented by a localised enhanced or depleted region and

it can be written as

$$p_0(r,\theta) = p_2\chi(r,\theta), \tag{4.1}$$

where ρ_2 and p_2 represent the density and the pressure outside the inhomogeneous region, respectively and the constant sound speed will be $C_S = \sqrt{\gamma p_2/\rho_2}$.

We consider an equilibrium magnetic field oriented along the z-axis (the longitudinal symmetry axis of the cylindrical waveguide, i.e. $\mathbf{B_0} = (0, 0, B_0(r,\theta))$, where $B_0(r,\theta)$ is an unknown function that can be determined using the radial and azimuthal components of the equilibrium momentum equation. Indeed, taking into account the inhomogeneous nature of the equilibrium pressure and magnetic field, these two equation can be written as

$$\begin{cases} \frac{\partial p_0}{\partial r} + \frac{1}{2\mu}\frac{\partial B_0^2}{\partial r} = 0, \\ \frac{\partial p_0}{\partial \theta} + \frac{1}{2\mu}\frac{\partial B_0^2}{\partial \theta} = 0, \end{cases} \tag{4.2}$$

where $B_0 = B_0(r,\theta)$. Let us integrate the first equation with respect to the radial coordinate r, that leads to $p_0(r,t)+B_0^2(r,\theta)/2\mu = C(\theta)$, where $C(\theta)$ is an integration constant that depends on the variable θ. Combining this relation with the other equilibrium equation in the system (4.2) leads to $dC(\theta)/d\theta = 0$, i.e. C is a genuine constant, which we will denote by a. As a result we have

$$B_0^2(r,\theta) = 2\mu a - 2\mu p_0(r,\theta). \tag{4.3}$$

In order to determine the constant quantity a, let us consider the particular case when the inhomogeneity is placed in the center of the waveguide, i.e. we are dealing with a concentric case that corresponds to $\varepsilon_1 = \varepsilon_2 = 0$ in Eq. (3.16). The equilibrium pressure at $r = \theta = 0$ can be written as

$$p_0(0,0) = p_2\left\{1 + \frac{(\sigma-1)}{2}\left[1 + \tanh\left(\frac{\tau}{\xi}\right)\right]\right\}.$$

Combining this result with Eq. (4.3), the constant quantity a can be expressed as

$$a = \frac{B_0^2(0,0)}{2\mu} + p_2\left\{1 + \frac{(\sigma-1)}{2}\left[1 + \tanh\left(\frac{\tau}{\xi}\right)\right]\right\},$$

where $B(0,0) = B_0(r=0,\theta=0)$. With this, Eq. (4.3) becomes

$$B_0^2(r,\theta) = B_0^2(0,0)\left\{1 + \frac{p_2}{B_0^2(0,0)/2\mu}\frac{\sigma-1}{2}\left[\tanh\left(\frac{\tau}{\xi}\right) + \tanh\left(\frac{\psi(r,\theta)-\tau}{\xi}\right)\right]\right\}. \tag{4.4}$$

In what follows we are going to denote the dimensionless quantity $p_2/[B_0^2(0,0)/(2\mu)] = \beta_1$, that is defined like a plasma-beta parameter, however this is just apparent, as it involves the ratio of kinetic pressure from the homogeneous annulus (p_2) and the value of the magnetic field at the centre (inside the inhomogeneous region). As a result, the equilibrium magnetic field can be written as

$$B_0(r,\theta) = B_0(0,0)\left\{1 + \beta_1\frac{\sigma-1}{2}\left[\tanh\left(\frac{\tau}{\xi}\right) + \tanh\left(\frac{\psi(r,\theta)-\tau}{\xi}\right)\right]\right\}^{1/2}. \tag{4.5}$$

The above result can be generalised in a straightforward way for an arbitrary position of the position of the inhomogeneity. Let us consider that in the eccentric case the inhomogeneity is centered in a position where $\hat{r} = (\epsilon_1^2 + \epsilon_2^2)^{1/2}$ and $\hat{\theta} = \tan^{-1}\left(\epsilon_2/\epsilon_1\right)$. In this case the profile of the inhomogeneous equilibrium magnetic field is given as

$$B_0(r,\theta) = B_0(\hat{r},\hat{\theta})\chi_B, \tag{4.6}$$

where

$$\chi_B = \left\{1 + \hat{\beta}\frac{\sigma-1}{2}\left[\tanh\left(\frac{\psi(r,t)-\tau}{\xi}\right) - \tanh\left(\frac{\hat{\psi}-\tau}{\xi}\right)\right]\right\}^{1/2}, \tag{4.7}$$

and

$$\hat{\psi} = \sqrt{(a\hat{r}\cos\hat{\theta} - \epsilon_1)^2 + (b\hat{r}\sin\hat{\theta} - \epsilon_2)^2},$$

and the meaning of the quantities a, b, τ and ξ is identical with the ones introduced in Chapter (3). Here the quantity β_2 is defined as $\hat{\beta} = p_2/[B_0^2(\hat{r},\hat{\theta})/(2\mu)]$. As before in Chapter (3), here we are going to concentrate on inhomogeneous regions of circular shape, so we choose $a = b = 1$.

4.3 Governing equation

We consider a straight magnetic cylinder with constant radius R and the dynamics will be described in cylindrical coordinates (r, θ, z). The inhomogeneous equilibrium magnetic field, $\mathbf{B}_0 = B_0(r,\theta)\hat{z}$ is directed along the z-axis. The equilibrium plasma density profile inhomogeneity is denoted by $\rho_0(r,\theta)$ and the components of the velocity and magnetic field perturbations are $\mathbf{u} = (u_r, u_\theta, u_z)$ and $\mathbf{b} = (b_r, b_\theta, b_z)$. The perturbed quantities can be Fourier decomposed with respect to the coordinate z and time, t, by writing them proportional to $e^{i(kz-\omega t)}$, where k is the longitudinal wave number.

In this case the linearised and ideal MHD equations transform into

$$\begin{aligned} -i\omega\rho(r,\theta)+\rho_0(r,\theta)&\left[\frac{1}{r}\frac{\partial}{\partial r}\left(ru_r(r,\theta)\right)+\frac{1}{r}\frac{\partial u_\theta(r,\theta)}{\partial\theta}+iku_z(r,\theta)\right] \\ &+u_r(r,\theta)\frac{\partial\rho_0(r,\theta)}{\partial r}+\frac{u_\theta(r,\theta)}{r}\frac{\partial\rho_0(r,\theta)}{\partial\theta}=0, \end{aligned} \tag{4.8}$$

$$\begin{aligned} i\omega\rho_0(r,\theta)u_r(r,\theta) =&\frac{\partial p(r,\theta)}{\partial r}-\frac{B_0(r,\theta)}{\mu}\left(ikb_r(r,\theta)-\frac{\partial b_z(r,\theta)}{\partial r}\right) \\ &+\frac{b_z(r,\theta)}{\mu}\frac{\partial B_0(r,\theta)}{\partial r}, \end{aligned} \tag{4.9}$$

$$\begin{aligned} i\omega\rho_0(r,\theta)u_\theta(r,\theta) =&\frac{1}{r}\frac{\partial p(r,\theta)}{\partial\theta}+\frac{B_0(r,\theta)}{\mu}\left(\frac{1}{r}\frac{\partial b_z(r,\theta)}{\partial\theta}-ikb_\theta(r,\theta)\right) \\ &+\frac{b_z(r,\theta)}{\mu r}\frac{\partial B_0(r,\theta)}{\partial\theta}, \end{aligned} \tag{4.10}$$

$$i\omega\rho_0(r,\theta)u_z(r,\theta) = ikp(r,\theta)-\frac{1}{\mu}\frac{b_\theta(r,\theta)}{r}\frac{\partial B_0(r,\theta)}{\partial\theta}-\frac{b_r(r,\theta)}{\mu}\frac{\partial B_0(r,\theta)}{\partial r}, \tag{4.11}$$

$$b_r(r,\theta) = \frac{-k}{\omega}B_0(r,\theta)u_r(r,\theta), \tag{4.12}$$

$$b_\theta(r,\theta) = \frac{-k}{\omega}B_0(r,\theta)u_\theta(r,\theta), \tag{4.13}$$

$$\begin{aligned} b_z(r,\theta) =& -\frac{iB_0(r,\theta)}{\omega r}\frac{\partial}{\partial r}\left(ru_r(r,\theta)\right)-\frac{iu_r(r,\theta)}{\omega}\frac{\partial B_0(r,\theta)}{\partial r} \\ &-\frac{iB_0(r,\theta)}{\omega r}\frac{\partial u_\theta(r,\theta)}{\partial\theta}-\frac{iu_\theta(r,\theta)}{\omega r}\frac{\partial B_0(r,\theta)}{\partial\theta}. \end{aligned} \tag{4.14}$$

The above equations can be combined into the expression of the total pressure

perturbation, (P_T) is given by

$$P_T = p + \frac{1}{\mu} B_0(r,\theta) b_z(r,\theta), \tag{4.15}$$

and the governing differential equation for the total pressure becomes

$$\frac{\partial}{\partial r}\left[\frac{r}{\rho_0\left(\omega^2 - k^2 V_A^2\right)}\frac{\partial P_T}{\partial r}\right] + \frac{1}{r}\frac{\partial}{\partial \theta}\left[\frac{1}{\rho_0\left(\omega^2 - k^2 V_A^2\right)}\frac{\partial P_T}{\partial \theta}\right] + \frac{n_0^2 r}{\rho_0(\omega^2 - k^2 v_A^2)} P_T = 0, \tag{4.16}$$

where the magnetoacoustic parameter, $n_0^2 = -m_0^2$ has been defined earlier (see Eq. 2.28) and it is going to be used in the following calculations as we are concentrating on body waves. We should mention here that although the form of n_0^2 agrees with its counterpart in homogeneous plasma, here all phase speeds are functions of r and θ. In our analysis we will restrict ourselves to the thick flux tube limit, i.e. we consider that the wavelength of waves is much smaller than the radius of the tube ($kR \gg 1$). Furthermore, we assume that in this limit the behaviour of slow body modes is similar to the one in a homogeneous waveguide, therefore the phase speed of waves can be written as $\omega^2/k^2 \approx C_S^2(1-\nu)$, where ν is a small dimensionless positive quantity and $\nu = 1 - \omega^2/k^2 C_S^2$.

Let us rewrite Eq. (4.16) for slow body modes into dimensionless form by introducing the new variable $\tilde{r} = r/R$. From now on, for simplicity, we will drop the *tilde*. In addition, the magnetoacoustic parameter becomes

$$n_0^2 = -k^2\left(1 - \frac{\omega^2}{k^2 C_S^2}\right)\left(1 - \frac{\gamma\hat{\beta}\chi}{2\chi_B^2}\right), \tag{4.17}$$

where the quantities χ and χ_B contain the information on the dependence of the equilibrium pressure and magnetic field on the coordinates r and θ. Furthermore, the coefficient functions of governing equation contain the expression $\rho_0(C_S^2 - V_A^2)$ that can be written as

$$\rho_0(C_S^2 - V_A^2) = \frac{B_0^2(\hat{r},\hat{\theta})}{\mu}\left(\frac{\gamma\hat{\beta}\chi}{2} - \chi_B^2\right) = \frac{B_0^2(\hat{r},\hat{\theta})}{\mu} F^{-1}(r,\theta). \tag{4.18}$$

As a result, the dimensionless governing equation for the total pressure

perturbation given by (4.16) becomes

$$\frac{\partial}{\partial r}\left(rF(r,\theta)\frac{\partial P_T}{\partial r}\right)+\frac{1}{r}\frac{\partial}{\partial \theta}\left(F(r,\theta)\frac{\partial P_T}{\partial \theta}\right)-(kR)^2\left(1-\frac{\omega^2}{k^2C_S^2}\right)\frac{2}{\gamma\hat{\beta}\chi}rP_T=0. \tag{4.19}$$

The above equation is a Sturm-Liouville eigenvalue equation and the eigenvalues as well as the corresponding eigenfunctions can be determined using a numerical approach for particular inhomogeneous density distribution assuming that $P_T(r,\theta)=0$ at the boundary of the tube corresponding to $r=1$.

4.4 Details of the numerical setup

Equation (4.19) will be solved numerically using the Galerkin FEM method subject to the usual Dirichlet boundary condition $P_T=0$ at $r=1$. As before, the eigenvalue of our problem will be the dimensionless phase speed of waves defined as $V_{ph}=\omega/kC_S$.

Given the particular form of the governing equation, similar to our approach presented in Chapter (3), we are going to use Cartesian coordinates to solve numerically the governing equation. For simplicity we also introduce the notation $g=2(kR)^2/(\hat{\beta}\gamma\chi(x,y))$. As a result, the governing equation becomes

$$F\frac{\partial P_T^2}{\partial x^2}+\frac{\partial F}{\partial x}\frac{\partial P_T}{\partial x}+F\frac{\partial P_T^2}{\partial y^2}+\frac{\partial F}{\partial y}\frac{\partial P_T}{\partial y}+gP_T-gV_{ph}^2P_T=0. \tag{4.20}$$

Since the coefficient function F depends on x and y, the terms $\partial F/\partial x$ and $\partial F/\partial y$ are approximated using Finite Difference Method (FDM) as

$$\frac{\partial F}{\partial x}=\frac{F(x+dx,y)-F(x-dx,y)}{2dx},\quad \frac{\partial F}{\partial y}=\frac{F(x,y+dy)-F(x,y-dy)}{2dy}.$$

The computational domain is discretized using linear combination of the small linear triangular finite elements. Each element is connected to another through nodes (more details can be found in subsection 3.5.1). Equation (4.20) needs to be solved for each and every node of the computational domain. For the present study, the solution of the differential equation, P_T, is written as the sum of orthogonal piecewise polynomial basis functions whose coefficients must satisfy the differential equation (4.20). The linear triangular element approximations need to be related with the differential equation using the shape functions

(denoted by H), often called basis functions or interpolation functions. The shape function depends on the type of element, as well as the polynomial approximation used for the element. As a result, we can write

$$u = \begin{bmatrix} H_1 & H_2 & H_3 \end{bmatrix} \begin{bmatrix} u_1 \\ u_2 \\ u_3 \end{bmatrix}, \tag{4.21}$$

where u_1, u_2 and u_3 are nodal variables that are unknown coefficients to be determined. For the linear triangular elements with three nodes, the shape functions for each node are given by an equation similar to Eq. (3.44).

Applying the finite element method, the first step is to convert the original governing differential (strong) form of the PDE into an integral (weak) form by multiplying with a test (weight) function denoted by w and integrating over the circular domain (Ω) that reflects the circular sunspot (more details can be found in Kwon and Bang (2018) and also in Chapter 3). Using an integration by part over the domain of triangular elements, Ω^e, and taking into account that on the boundary the eigenfunction vanishes, the integral equation transforms into

$$-F \int_{\Omega^e} \frac{dw}{dx}\frac{du}{dx} d\Omega^e = 0, \quad -F \int_{\Omega^e} \frac{dw}{dy}\frac{du}{dy} d\Omega^e = 0, \tag{4.22}$$

$$\frac{\partial F}{\partial x} \int_{\Omega^e} \frac{du}{dx} d\Omega^e = 0, \quad \frac{\partial F}{\partial y} \int_{\Omega^e} w\frac{du}{dy} d\Omega^e = 0, \tag{4.23}$$

$$g \int_{\Omega^e} wu d\Omega^e = 0, \quad -gV_{ph}^2 \int_{\Omega^e} wu d\Omega^e = 0. \tag{4.24}$$

For the Galerkin's method, we consider the test functions (w) as the shape function of the trial function P_T, so we write $w = H_i$. Substitution of these shape functions back into the weak solution Eqs. (4.22) - (4.24) with element discretization, results in element matrix which is given by the series of equations

$$\left[-F \int_{\Omega^e} \mathbf{H}_x \mathbf{H}_x^T d\Omega^e - F \int_{\Omega^e} \mathbf{H}_y \mathbf{H}_y^T d\Omega^e \right] \mathbf{u} = 0, \tag{4.25}$$

$$\left[\frac{\partial F}{\partial x} \int_{\Omega^e} \mathbf{H}\mathbf{H}_x^T d\Omega^e + \frac{\partial F}{\partial y} \int_{\Omega^e} \mathbf{H}\mathbf{H}_y^T d\Omega^e \right] \mathbf{u} = 0, \tag{4.26}$$

$$\left[g\int_{\Omega^e}\mathbf{H}\mathbf{H}^T d\Omega^e - gV_{ph}^2\int_{\Omega^e}\mathbf{H}\mathbf{H}^T d\Omega^e\right]\mathbf{u}=0, \tag{4.27}$$

where

$$\mathbf{H}=\begin{bmatrix}H_1\\H_2\\H_3\end{bmatrix},\quad \mathbf{u}=\begin{bmatrix}u_1\\u_2\\u_3\end{bmatrix},\quad \mathbf{H}_x=\begin{bmatrix}\frac{dH_1}{dx}\\\frac{dH_2}{dx}\\\frac{dH_3}{dx}\end{bmatrix},\quad \mathbf{H}_y=\begin{bmatrix}\frac{dH_1}{dy}\\\frac{dH_2}{dy}\\\frac{dH_3}{dy},\end{bmatrix},$$

and the superscript T denotes the transpose. Using the particular shapes of the elements, the first derivatives of the shape functions can be calculated as

$$\begin{bmatrix}\frac{dH_1}{dx}\\\frac{dH_2}{dx}\\\frac{dH_3}{dx}\end{bmatrix}=\begin{bmatrix}y_2-y_3\\y_3-y_1\\y_1-y_2\end{bmatrix},\qquad \begin{bmatrix}\frac{dH_1}{dy}\\\frac{dH_2}{dy}\\\frac{dH_3}{dy}\end{bmatrix}=\begin{bmatrix}x_3-x_2\\x_1-x_3\\x_2-x_1\end{bmatrix}. \tag{4.28}$$

Since the first order derivatives of the shape functions are constants, they can be taken out from the integral in Eqs. (4.25)- (4.27) so that

$$\left[-F\mathbf{H}_x\mathbf{H}_x^T\int_{\Omega^e}d\Omega^e - F\mathbf{H}_y\mathbf{H}_y^T\int_{\Omega^e}d\Omega^e\right]\mathbf{u}=0, \tag{4.29}$$

$$\left[\frac{\partial F}{\partial x}\int_{\Omega^e}\mathbf{H}d\Omega^e\mathbf{H}_x^T+\frac{\partial F}{\partial y}\int_{\Omega^e}\mathbf{H}d\Omega^e\mathbf{H}_y^T\right]\mathbf{u}=0, \tag{4.30}$$

$$\left[g\int_{\Omega^e}\mathbf{H}\mathbf{H}^T d\Omega^e - gV_{ph}^2\int_{\Omega^e}\mathbf{H}\mathbf{H}^T d\Omega^e\right]\mathbf{u}=0. \tag{4.31}$$

Our relation can be further simplified using the well-known relations

$$M^e=\int_{\Omega^e}\mathbf{H}\mathbf{H}^T d\Omega^e=\frac{A}{12}\begin{bmatrix}2&1&1\\1&2&1\\1&1&2\end{bmatrix}, \tag{4.32}$$

$$C^e=\int_{\Omega^e}\mathbf{H}d\Omega^e=\frac{A}{3}\begin{bmatrix}1\\1\\1\end{bmatrix}. \tag{4.33}$$

After substituting Eqs. (4.32) and (4.33) in Eqs. (4.29- 4.30), we obtain

$$\frac{\partial F}{\partial x}C^e\mathbf{H}_x^T\mathbf{u}+\frac{\partial F}{\partial y}C^e\mathbf{H}_y^T\mathbf{u}=0, \tag{4.34}$$

$$gM^e\mathbf{u} - gV_{ph}^2 M^e\mathbf{u} = 0, \tag{4.35}$$

The above equations can be simplified as

$$-F\mathbf{H}_x\mathbf{H}_x^T A\mathbf{u} - F\mathbf{H}_y\mathbf{H}_y^T A\mathbf{u} + \frac{\partial F}{\partial x}C^e\mathbf{H}_x^T\mathbf{u} + \frac{\partial F}{\partial y}C^e\mathbf{H}_y^T\mathbf{u} + gM^e\mathbf{u} - gV_{ph}^2 M^e\mathbf{u} =$$

$$(a_1)_{3*3}\mathbf{u} + (a_2)_{3*3}V_{ph}^2\mathbf{u} = 0, \tag{4.36}$$

where

$$(a_2)_{3*3} = -gM^e,$$

$$(a_1)_{3*3} = -F\mathbf{H}_x\mathbf{H}_x^T A - F\mathbf{H}_y\mathbf{H}_y^T A + \frac{\partial F}{\partial x}C^e\mathbf{H}_x^T + \frac{\partial F}{\partial y}C^e\mathbf{H}_y^T + gM^e,$$

represent the local stiffness matrices for each element. Each local stiffness matrix contains an equation for each node in the element, the so-called local equation. The global stiffness matrices are obtained by assembling all of the local stiffness matrices or by organising all of the local equations for each node as

$$(A_2)_{N*N}{V_{ph}}^2\begin{bmatrix} u_1 \\ \vdots \\ u_N \end{bmatrix} + (A_1)_{N*N}{V_{ph}}^0\begin{bmatrix} u_1 \\ \vdots \\ u_N \end{bmatrix} = 0, \tag{4.37}$$

therefore we have that $A_2{V_{ph}}^2\mathbf{U} + A_1{V_{ph}}^0\mathbf{U} = 0$.

In the present study a new algorithm is developed to obtain the eigenvalues and eigenvectors of a quadratic matrix polynomial using Galerkin FEM and QZ factorization. The method is potentially capable of handling a variety of eigenvalue problems in the most efficient way. In the code, the built-in MATLAB function '$(polyeig(A_1, A_2))$' (based on the QZ factorization) is used to obtain the generalized quadratic eigenvalues and eigenvectors. The code is tested against the eigenvalues obtained for the uniform circular cross sectional magnetic flux tubes.

Table 4.1: Values of the physical parameters used for the numerical modeling and analysis. Unless specified otherwise, for each case we consider $kR = 4$ and $\hat{\beta} = 3 \times 10^{-3}$.

	σ	τ	ξ	ϵ_1	ϵ_2
C1: Uniform density	1				
C2: Density enhancement					
C2.1: - concentric	2.5	0.5	9.1×10^{-2}	0	0
C2.2: - right eccentric	2.5	0.5	9.1×10^{-2}	0.5	0
C2.3: - upper right eccentric	2.5	0.5	9.1×10^{-2}	0.3	0.3
C3: Density depletion					
C3.1: - concentric	0.5	0.5	9.1×10^{-2}	0	0
C3.2: - right eccentric	0.5	0.5	9.1×10^{-2}	0.5	0
C3.3: - upper right eccentric	0.5	0.5	9.1×10^{-2}	0.3	0.3

4.5 Slow body modes in the presence of inhomogeneous equilibrium density, pressure and magnetic field

In this section, we will analyze the modification of the spatial structure of the total pressure perturbation corresponding to slow body modes propagating in a cylindrical waveguide in the presence of inhomogeneous equilibrium under photospheric conditions, assuming a short wavelength limit and an isothermal plasma. The values of the parameters used in our simulations are shown in Table (4.1).

As a benchmark for our study that allows us to discern the alterations in wave properties resulting from a non-uniform plasma and field equilibrium, first we show the results we obtain in the case of homogeneous equilibrium, i.e. when the value of the parameter σ is equal to one. These results cover the earlier findings by Edwin and Roberts (1983*a*). The results presented in Chapter (3) suggest that the effect of inhomogeneity is more pronounced for higher order modes, therefore, here we consider the results not only for the three modes studied earlier in Chapter (3), but also for several higher order modes.

Figure (4.1) displays the dimensionless phase speeds and the spatial structure of slow body modes of various radial and azimuthal order in the case of a homogeneous equilibrium, i.e. when $\sigma = 1$. The equilibrium density and mag-

netic field distribution are shown in the first two panels of the upper row and they have a constant value, expected from a homogeneous density and magnetic field distribution. The remaining panels stand for the spatial structure of fundamental slow body sausage mode (third panel), the two orthogonally polarised fundamental slow kink modes (last panel of the first row and first panel of the second row), the pair of the fluting mode of order $n = 2$ (second and third panels of the second row), slow sausage overtone (fourth panel, second row), the pair of fluting mode of order $n = 3$ (first two panels of the third row), the pair of slow body kink overtone (last two panels of the third row), the pair of the slow body fluting mode of order $n = 4$ (first two panels of the fourth row), and the pair of the fluting overtone mode of order $n = 2$ (last two panels of the fourth row). Although the pair (n, m) is strictly applicable for the homogeneous case, remnants of the symmetry described by these numbers can be recovered even in the inhomogeneous case. In addition, we chose to represent the corresponding orthogonal companion of particular waves (kink, fluting). In a homogeneous plasma these modes would appear identical with their counterpart, however shifted by a 90 degree rotation. In an inhomogeneous plasma, the inhomogeneity will influence these modes differently, depending on the direction of their polarisation.

Since we are dealing with the case of short wavelength limit, all dimensionless speeds (shown on the top of each panel) are converging to one, i.e. the constant sound speed. The obtained results provide clear evidence that, under the assumption of a homogeneous equilibrium, the eigenmodes exhibit global harmonic oscillations and possess well-known symmetrical characteristics along their respective axes. As before, the color bars represent the amplitude of the total pressure perturbation divided by its maximum value for each mode. The regions that are shaded in red and blue correspond to the crests (maxima) and valleys (minima) of amplitude variation in the total pressure perturbation. This result also proves our initial assumption according to which the Dirichlet boundary condition imposed in our case would not modify qualitatively or quantitatively the solution of dispersion relation obtained in the case of body modes (in line with the findings by Aldhafeeri et al. (2022*b*)). The modes are listed in the descending order of their phase speed in units of the constant sound speed.

The changes in the spatial structure of slow body waves as well as the modification of the dimensionless phase speed in terms of the parameters of

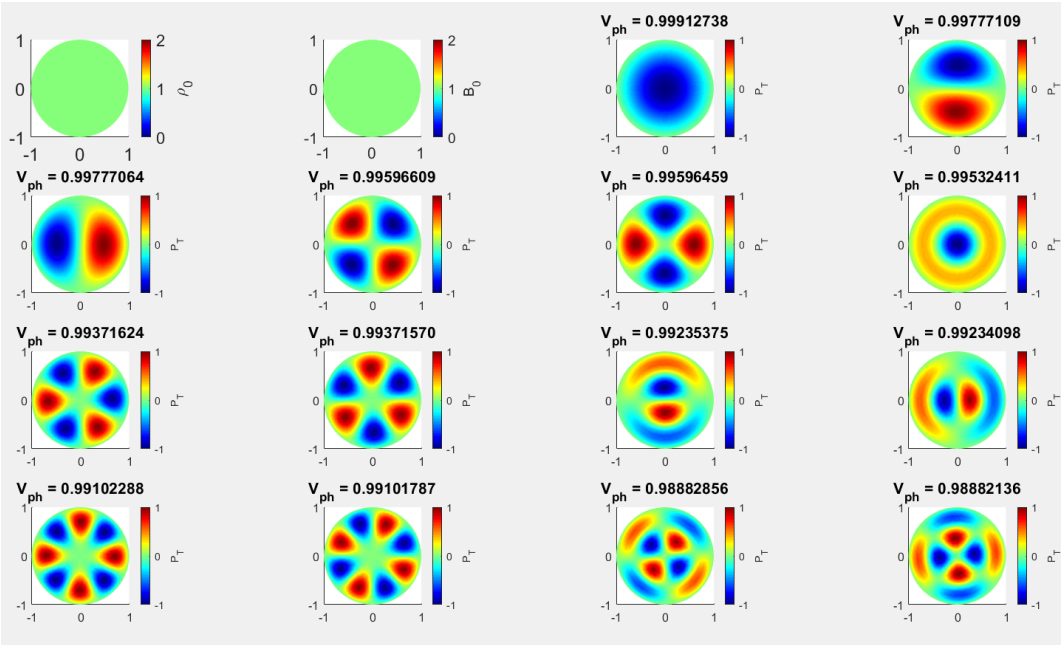

Figure 4.1: The spatial structure of slow body waves in a homogeneous ($\sigma = 1$) cylindrical waveguide under photospheric conditions together with the density and magnetic field distribution (first two panels in the first row). The remaining panels show the spatial structure of slow body modes sausage (top row, third panel), followed by kink and its corresponding orthogonal mode. The second row contains the two orthogonally polarised fluting mode of order $n = 2$ (second and third panel), followed by slow sausage overtone, the fluting modes of order $n = 3$ (first two panels in the third row) and the pair of slow body kink overtones, the pair of slow body fluting modes of order $n = 4$ (the first two panels of the fourth row, and the pair of fluting overtone of order $n = 2$. The color bars display the magnitude of the total pressure perturbation amplitude divided by its maximum value. The red and blue shaded regions represent crests (maxima) and valleys (minima) of amplitude variation of total pressure perturbation.

local equilibrium plasma density given by Eq. (3.16) and magnetic field (Eq. 4.7) will be discussed in the specific situations when the inhomogeneity is represented as a local density enhancement ($\sigma > 1$) and density depletion ($\sigma < 1$). We should note here that due to the requirement of the conservation of the equilibrium total pressure, an enhancement in density (or pressure) would mean that the magnetic field will be depleted. The modifications in the oscillatory patterns of waves are analyzed for three particular positions of the equilibrium inhomogeneity loading, e.g. concentric (case C2.1), right eccentric (case C2.2), and upper right eccentric (case C2.3). The particular values of parameters chosen for these three cases are given in Table (4.1).

4.5.1 Slow body modes in the presence of concentric and eccentric equilibrium density (pressure) enhancements

The modification in the values of the radial distribution of equilibrium density, pressure and magnetic field will result in modifications to the dimensionless phase speed and the spatial structure of slow body modes represented by the changes in the total pressure perturbation. Let us first discuss the case of a concentric loading (Fig 4.2), for which the parameters used in finding numerically solutions to Eq. (4.19) are given by case C2.1 in Table (4.1). The panels in Fig. (4.2) show the equilibrium density and magnetic field distributions (first two panels in the upper row), the spatial structure of the fundamental slow body sausage mode (third panel) and the two orthogonal fundamental slow body kink modes (last panel of the upper row and first panel of the second row), the two orthogonal fluting mode of order $n = 2$ (second and third panel of the second row) the two orthogonal fluting modes of order $n = 3$ (last panel of second row and first panel of the third row), the sausage overtone (second panel of the third row), the two orthogonal fluting modes $n = 4$ (the last two panels of the third row), the pair of kink overtone (first two panels of the fourth row) and the pair of $n = 5$ fluting mode (the last two panels of the fourth row). As before, in all panels the amplitude of the total pressure was normalised by the maximum value of this quantity .

First of all, it is evident that the eigenvalues of the studied waves exhibited a very small decrease in comparison to the uniform case. Comparing Figs. (4.1) and (4.2), it becomes apparent that the modes exhibit symmetry in relation

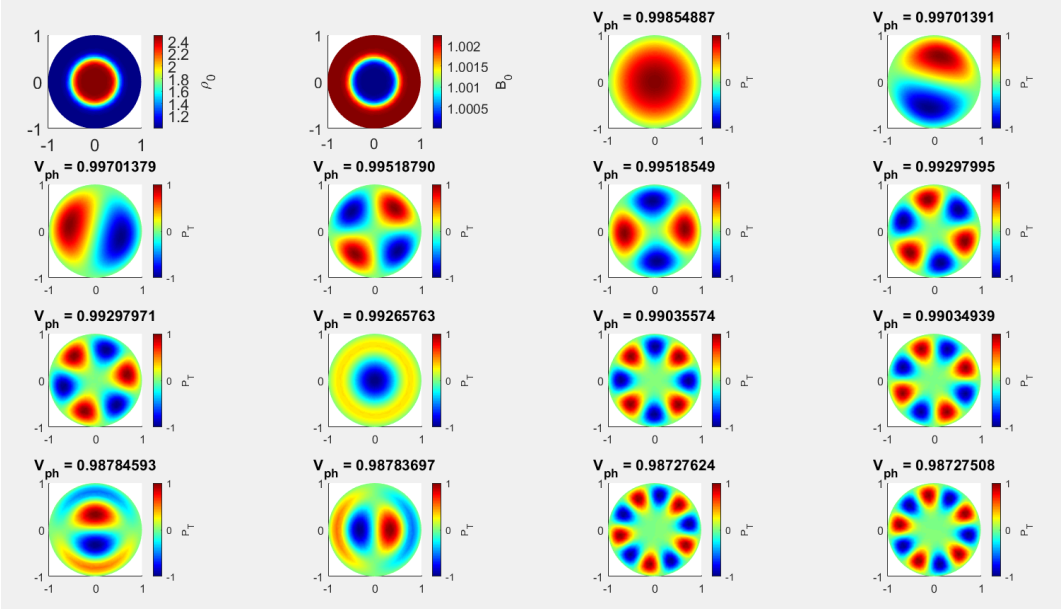

Figure 4.2: The same modes as in Fig. (4.1), but here we show the results in the presence of a concentric density (and magnetic field) enhancement. All characteristic values of parameters used in these numerical solutions correspond to the case C2.1 in Table (4.1).

to the central axis of the circular waveguide. The aforementioned findings indicate that the presence of a concentric inhomogeneous equilibrium density enhancement leads to an incremental decrease in the eigenvalues of modes, however the oscillating modes have global harmonic oscillations character, as compared to the scenario where the density enhancement is uniform. The most affected modes appear to be the kink overtone and the fluting overtone of order $n = 2$ shown in the last row of Fig. (4.2). When comparing the concentric density enhancement case to the uniform case, it is evident that the phase speed of the sausage overtone decreases and becomes less than the phase speed of the fluting mode of order $n = 3$. Furthermore, the kink overtone's phase speed decreases relative to the order $n = 4$ fluting mode's phase speed. Remarkably, in the first eighteen low order slow body modes, the concentric density enhancement case does not exhibit the sausage overtone of order $n = 2$, and the overtone fluting of order $n = 2$ drops below the phase speed of the fluting mode of order $n = 6$.

The enhanced eccentric equilibrium inhomogeneity distribution in density and magnetic field corresponds to an inhomogeneity loading whose position is shifted away from the origin and the position of its center is controlled by the

two parameters, ϵ_1 and ϵ_2. In reality, the position of the inhomogeneous density loading can be arbitrary, however, in the present study we discuss only cases that correspond to the inhomogeneous density shifted along the horizontal axis (see Fig. 4.3), with parameters given by case C2.2, and a position where both quantities describing the location of the density load are non-zero (Fig. 4.4, with parameters given by case C2.3 in Table 4.1). All the figures we are going to present display the spatial structure of the normalised total pressure of the same slow body modes as before.

The interplay between the effects of inhomogeneous density and magnetic field leads to some interesting patterns in the spatial structure of waves. Compared with the spatial structures of modes we obtained when only the equilibrium density was considered inhomogeneous (Figs 3.4 and 3.5), the difference in the oscillatory patterns of the studied modes highlights the effect of the magnetic field homogeneity. While for the results shown in Chapter 3 the conclusion on the behaviour of modes was clear, for the case presented in this chapter, a unified conclusion on the behaviour of waves is difficult to draw. The presence of magnetic field inhomogeneity affects the studied modes in a differential way, clearly the higher order modes are the most affected. In contrast to the results obtain in the case of only the density inhomogeneity, the modes do not migrate towards lower density regions (as the regions where body wave solutions were allowed shrunk), here the magnetic field inhomogeneity compensates the effect of inhomogeneous density enhancement, extending the size of the regions where modes are possible. Equally, the effect of all considered inhomogeneities results in a different effect on waves depending whether the polarisation direction of waves coincides with the radial direction along which the inhomogeneous regions are shifted. As a result, the symmetry of the modes is distorted and a categorisation of certain higher order modes based on a simple visual inspection is no longer possible.

For the case when the inhomogeneous region is shifted along the horizontal axis, compared to the concentric density enhancement case, it is evident that the phase speed of the sausage overtone decreases and becomes less than the phase speed of the fluting mode of order $n = 3$. Furthermore, the kink overtone's phase speed decreases relative to the order $n = 4$ fluting mode's phase speed. Remarkably, in the first eighteen low order slow body modes, the concentric density enhancement case does not exhibit the sausage overtone of order $n = 2$, and the overtone fluting of order $n = 2$ drops below the phase

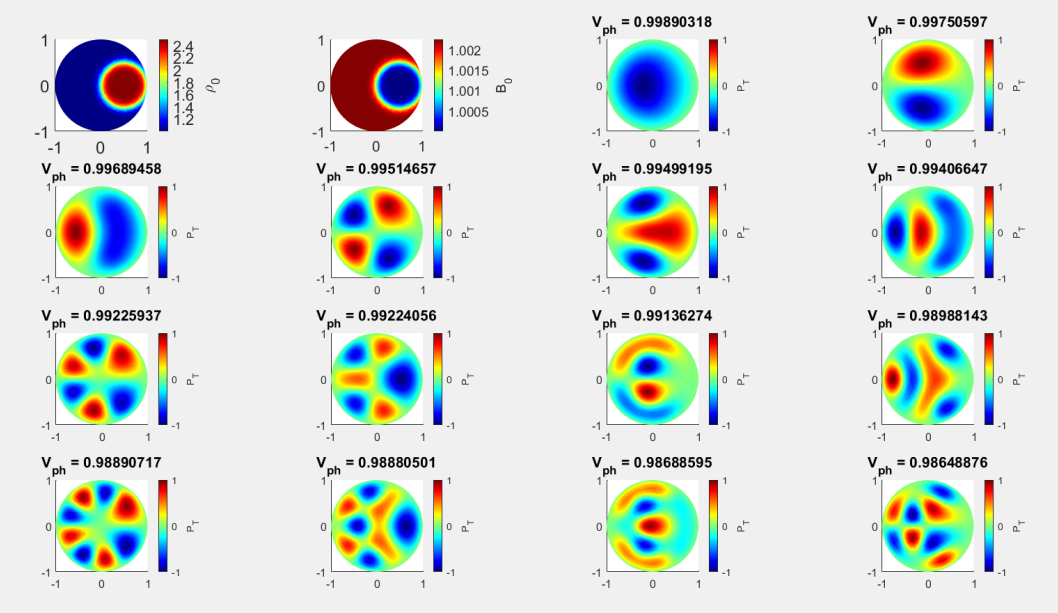

Figure 4.3: The same MHD modes as in Fig. 4.1, but here we show the results for an eccentric density (and magnetic field) loading, situated along the horizontal direction. The parameters used for this visualization are given by Case C2.2 in Table (4.1).

speed of the fluting mode of order $n = 6$. Low order modes such as the sausage, kink, and kink overtone fluting modes of order $n = 2$ and $n = 3$ can still be distinguished in terms of their spatial structure. Their orthogonal slow body modes, on the other hand, exhibit contradictory behaviour, with some modes shifting leftward and others rightward in the direction of the higher density.

When the inhomogeneous region is shifted along an arbitrary direction (along the first bisector as in Fig. (4.4), the modification in the spatial structure of modes remains qualitatively the same as the one presented when the inhomogeneity loading was placed along the horizontal axis.

4.5.2 Slow body modes in the presence of concentric and eccentric depleted equilibrium density inhomogeneity

In the case of a depleted density, (and consequently, the plasma pressure) inhomogeneity, the maximum value of density of the inhomogeneous region is less than the density of the homogeneous part of the waveguide, i.e. we consider the case when $\sigma < 1$. At the same time, given the requirement of total

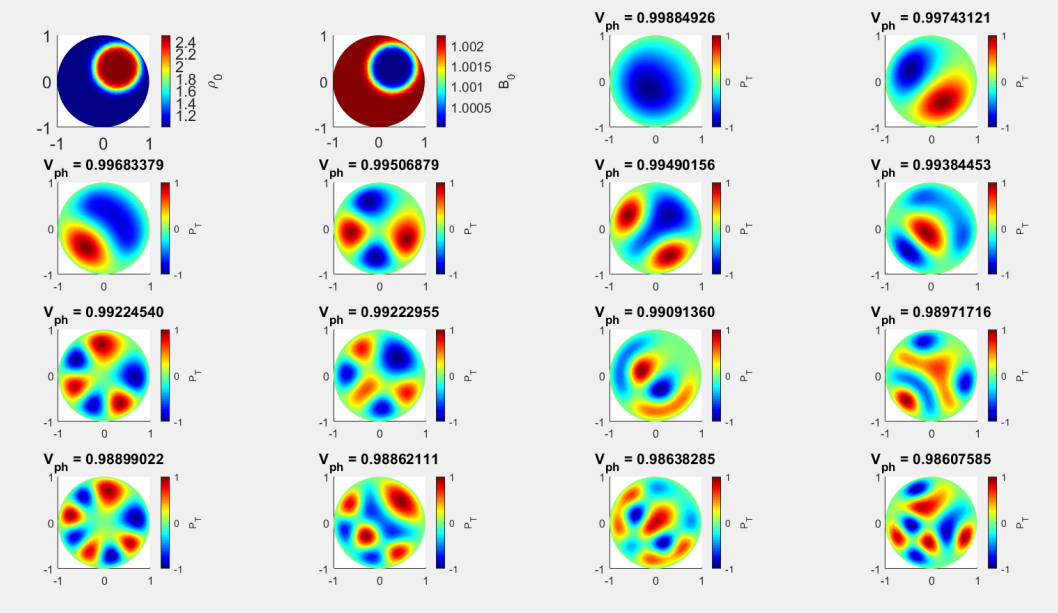

Figure 4.4: The same MHD modes as in Fig. (4.1), but here we show the results for an eccentric density loading (and magnetic field), situated along the bisector direction. The parameters used for this visualization are given by Case C2.3 in Table (4.1).

pressure conservation, the equilibrium magnetic field takes its maximum value inside the inhomogeneous region. In this section we are going to investigate the modifications in the spatial structure of the same slow body modes as before, when the inhomogeneity has a concentric position ($\epsilon_1 = \epsilon_2 = 0$) and an eccentric position when the values of the centre of inhomogeneity, ϵ_1 and ϵ_2 take any value but zero at the same time.

The values of parameters used for our numerical investigations are given in Table (4.1), case C3). Figure (4.5), with parameters given by Case C3.1 shows the spatial structure of the normalized total pressure perturbation corresponding to the same body modes as before in the case of concentric loading, while Figs. (4.6, Case C3.2 in Table 4.1) and (4.7, Case C3.3 in Table 4.1) show the spatial structure of the total pressure for an eccentric loading, when the density inhomogeneity is placed along the horizontal axis and in a position along the first bisector. The modes in the panels of the Figs. (4.5)-(4.7) are listed in the descending order of their dimensionless eigenvalues (propagation speed in units of the sound speed in the homogeneous region) shown at the top of the panels.

Compared to the case when only the density inhomogeneity was consid-

ered, the spatial structure of the slow body modes we recovered in this case show a distinctive behaviour, and this is due solely to the inhomogeneity in the equilibrium magnetic field. Although from Figs. (4.2) and (4.5) is evident that the central symmetry is maintained (also similar to the symmetry in the homogeneous case), the spatial extent where modes are possible has increased. The associated eigenmodes exhibit new pattern features differing from those seen in the case of uniform and concentric densities in the presence of concentric equilibrium depletion density inhomogeneities. These results demonstrate that the eigenvalues have a very small decrease in the presence of concentric non-uniform equilibrium density. As the spatial extent of size of modes' space structure decreases, it may become more challenging to detect them compared to the scenario where density enhancement is uniform, particularly along the internal scattered nodes where centres are more reduced. The overtones of fluting modes of order $n = 2$ (Fig. 4.5) and the kink overtones displayed in the last row of the figure appear to be the most affected modes. Moreover, the spatial structure of these modes also tends to extend very near to the boundaries in the case of concentric equilibrium density depletion, indicating that they adhere to lower densities with less migration than that seen in Chapter 3. These intriguing findings have significant ramifications for optimising modal structures that may be viewed, compared, and correlated in observational data as well as for constructing and organising modes in circular structures.

In a similar vein, the eigenmodes are associated with eccentrically balanced enhanced density inhomogeneities (placed along the horizontal axis and the first bisector, Figs. 4.3 and 4.4) differ from those obtained for an eccentrically placed depleted density inhomogeneities shown in Figs. (4.6) and (4.7), respectively. The investigated modes are differentially affected by the presence of magnetic field and density inhomogeneities, with the higher order modes being the most affected. Here, the magnetic field inhomogeneity offsets the effect of inhomogeneous density, expanding the size of the regions where modes are possible. This is in contrast to the results obtained in the case when only the density inhomogeneity was considered, where the modes migrated towards lower density regions (as the regions where body wave solutions are possible shrunk). Similarly, depending on whether the polarisation direction of the waves coincides with the radial direction along which the inhomogeneous areas are shifted, the influence of all relevant inhomogeneities results in a varied effect on waves. This leads to a distortion of the modes' symmetry, making

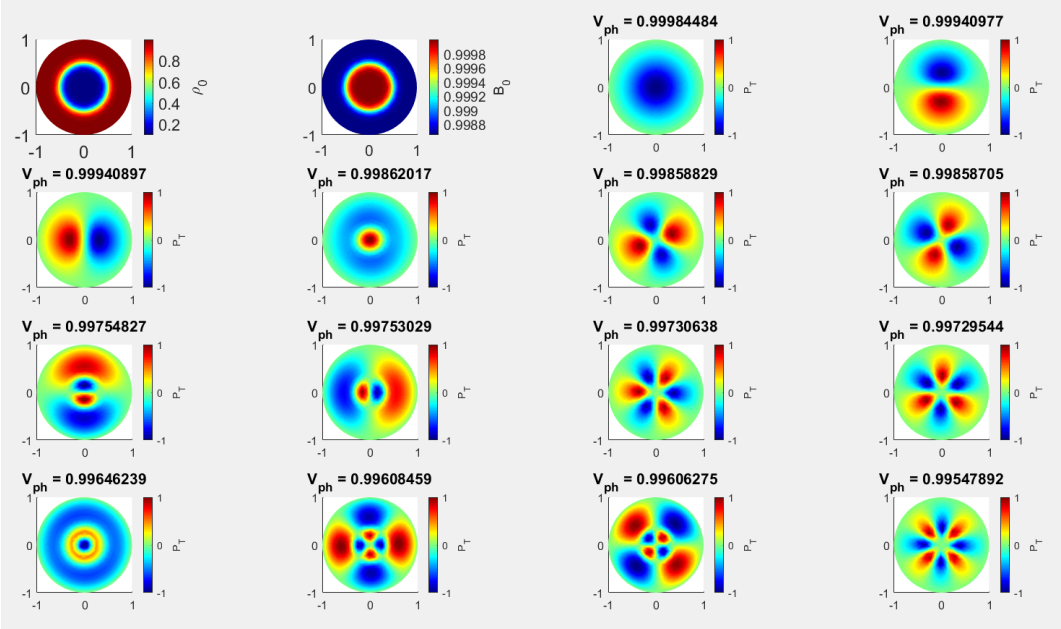

Figure 4.5: The same modes as in Fig. (4.1), but here we show the results in the presence of a concentric depleted density (and magnetic field) enhancement. All characteristic values of parameters used in these numerical solutions correspond to the case C3.1 in Table (4.1).

it impossible to classify some higher order modes by a mere visual inspection. As before, the higher order modes are the most affected by the presence of equilibrium density and magnetic field. Similar to the conclusion obtained in the case of enhanced density, the spatial structure of slow body modes does not change if the density loading is placed along the horizontal or vertical axes. A localized wave observation in a sunspot could be a way to identify the location of a plasma and field inhomogeneity in the umbral region, even if this inhomogeneity cannot be seen in observations.

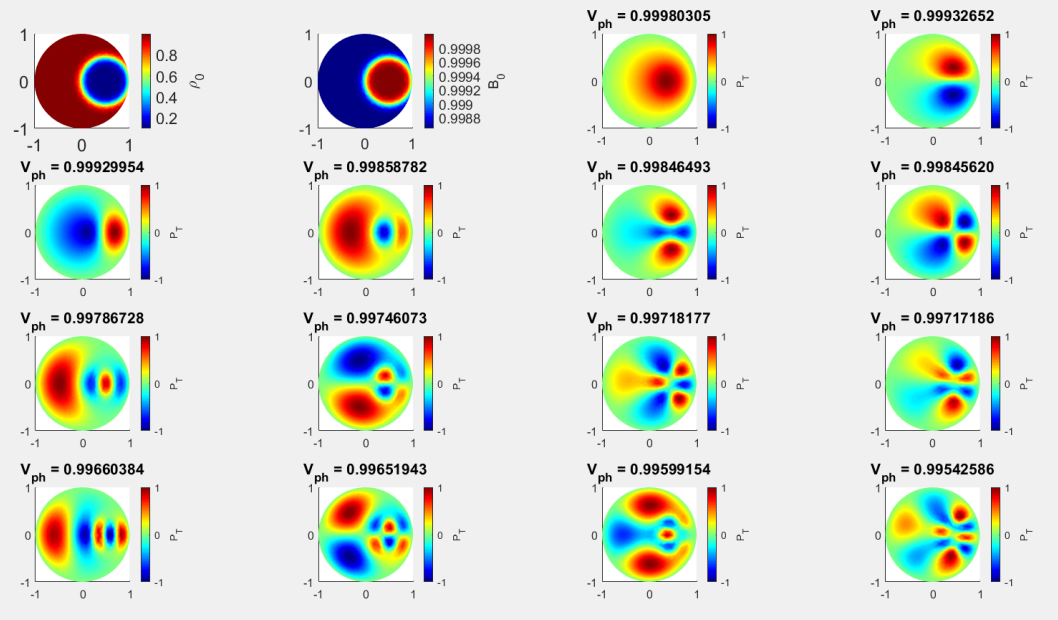

Figure 4.6: The same as in Fig. (4.1) but for the case of an eccentric density (and magnetic field) loading, situated along the horizontal direction. The parameters used for this visualization are given by case C3.2 in Table (4.1).

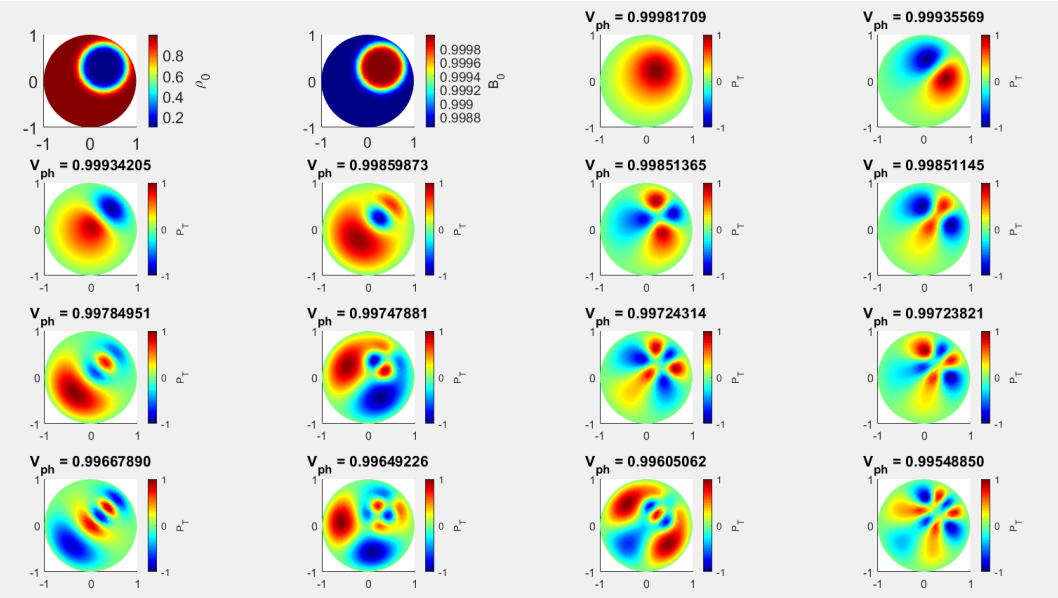

Figure 4.7: The same as in Fig. (4.1), but here the depleted density region is situated in an eccentric position along the bisector direction. The parameters used for this visualization are given as case C3.2 in Table (4.1).

4.6 The spatial structure of line-of-sight (LOS) velocity in the presence of plasma inhomogeneity

For practical reasons it is much more convenient to convert our results presented earlier in this Chapter into quantities that are easier to observe. Wave activity can be determined by the Doppler-shift of intensity lines of many instruments (e.g. SDO/HMI, Hinode/SOT), therefore representing the spatial structure of the line-of-sight (LOS) component of the velocity is much more closer to observations and allows a much easier identification. The variation of this quantity will be derived from the values of eigenvalue and eigenfunction (here the total pressure) obtained earlier.

In a recent investigation by Stangalini et al. (2022), the authors used high resolution Interferometric Bidimensional Spectropolarimeter (IBIS) at the DST (Dunn Solar Telescope; New Mexico, USA) observations of an intense (magnetic field in excess of 3.5 kG) to evidence the presence of large scale coherent MHD oscillations in a sunspot (see Fig. 4.8). The LOS velocity in both the spatial and temporal domains was filtered at the most significant frequencies that allowed the isolation of the determination of the contribution of global resonant modes from localized fluctuations detected in the same magnetic structure. Panel (c) in Fig. (4.8) shows how fragmented is the LOS velocity determined from observations. The oscillations associated with the global eigenmodes were found to account for up to 10% of the total variance of all the Doppler fluctuations observed in the umbra. The authors solved numerically the governing equation for waves in the given sunspot to model the pattern of the observed LOS velocity by linearly superposing several individual modes of higher degree. The dominating modes are found to be sausage-like and contain both the fundamental and the first radial overtone in reference to the usual magnetic cylinder model. Their results showed that most of the energy was contained in the first 10–15 eigenmodes, but at least 30 modes were needed to fully reproduce the observed signal (see the right-hand side panel of Fig. 4.8). When creating the numerical model, one must consider that the pattern is highly sensitive to the precise form of the umbra. As a result, the form of the umbra distorts the oscillatory rings, which diverge from the normal magnetic cylinder model's perfectly circular shape.

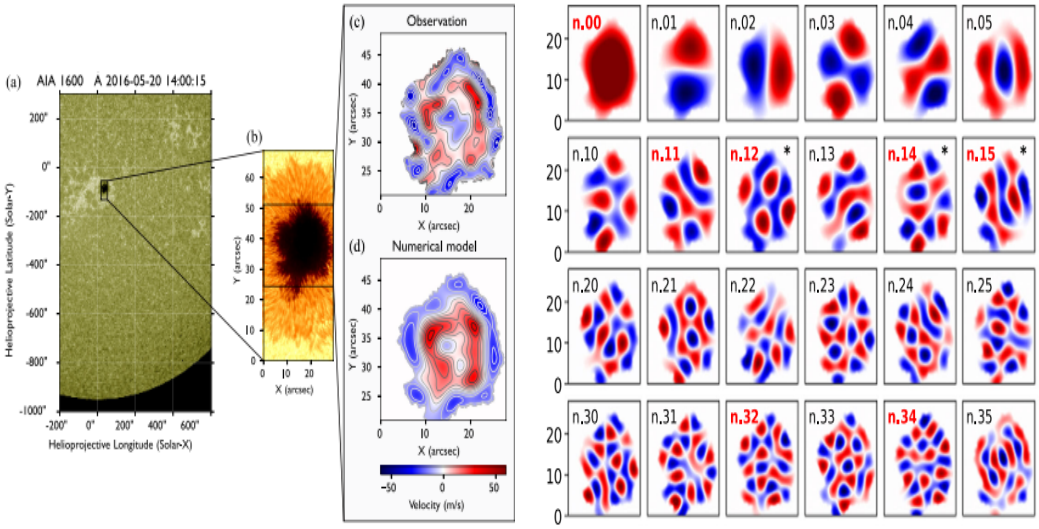

Figure 4.8: Detection of high radial order MHD oscillations in a sunspot (a): The AIA/SDO complete disc image in the 1600 Å band, displays the IBIS FOV as a rectangular area that is pure black. (b): High-resolution intensity picture taken by IBIS in the continuum close to the spectral line Fe I 6173 Å. (c): An illustration of an instantaneous map of the filtered Doppler velocity obtained from the spectrum imaging sequence of IBIS Fe I 6173 Å. The sunspot umbra can support concentric oscillatory annuli; (d): Numerically modelled LOS velocities, assuming a fixed umbra-penumbra boundary, produced by superposing nine orthogonal eigenmodes. The right-hand side panel shows the computed eigenmodes for the sunspot. The black asterisks indicate the most energetic modes during the whole observation, while the red labels highlight the sample modes that were used to recreate the pattern seen in panels (c) and (d). Decomposing the measured velocity pattern into a linear combination of the computed modes yields the modal reconstruction. Credit: Stangalini et al. (2022).

In this section we are approaching the problem of pattern determination of the LOS velocity in a sunspot with inhomogeneous magnetic field and density from a different perspective. We will numerically solve the governing equation that determines the spatial structure of the LOS velocity and find the morphology of this quantity that could be compared with observations of the Doppler velocity in various wavelengths.

In order to derive the governing equation of the z-component of the velocity we would need to go back to the linearised MHD equations we presented in Eqs. (4.8)-(4.14). After straightforward calculations, the connection between the z-component of the velocity, and the radial, azimuthal components of velocity can be given as

$$\omega u_z = \frac{kP_T}{\rho_0} + \frac{ikV_A^2}{r\omega}\frac{\partial}{\partial r}\left(ru_r\right) + \frac{ikV_A^2}{r\omega}\frac{\partial u_\theta}{\partial \theta}. \tag{4.38}$$

In addition, Eqs. (4.12)–(4.14) can be combined with Eq. (4.15), leading to

$$\frac{i\rho_0}{r\omega}(\omega^2 - k^2V_A^2)ru_r = \frac{\partial P_T}{\partial r}, \tag{4.39}$$

and

$$\frac{i\rho_0}{\omega}(\omega^2 - k^2V_A^2)u_\theta = \frac{1}{r}\frac{\partial P_T}{\partial \theta}. \tag{4.40}$$

Combining the last three relations, the field-aligned component of the velocity can be given in terms of the total pressure as

$$\omega u_z = \frac{kP_T}{\rho_0} + \frac{kV_A^2}{r}\frac{\partial}{\partial r}\left[\frac{r}{\rho_0(\omega^2 - k^2V_A^2)}\frac{\partial P_T}{\partial r}\right] + \frac{kV_A^2}{r^2}\frac{\partial}{\partial \theta}\left[\frac{1}{\rho_0(\omega^2 - k^2V_A^2)}\frac{\partial P_T}{\partial \theta}\right]. \tag{4.41}$$

As before, let us introduce the dimensionless radial variable, $\tilde{r}$ such that $\tilde{r} = r/R$, where R is the constant radius of the flux tube. In what follows we are going to neglect the *tilde*. As a result, our governing equation transforms into

$$\omega u_z = \frac{kP_T}{\rho_0} + \frac{kV_A^2}{rR^2}\frac{\partial}{\partial r}\left[\frac{r}{\rho_0(\omega^2 - k^2V_A^2)}\frac{\partial P_T}{\partial r}\right] + \frac{kV_A^2}{r^2R^2}\frac{\partial}{\partial \theta}\left[\frac{1}{\rho_0(\omega^2 - k^2V_A^2)}\frac{\partial P_T}{\partial \theta}\right]. \tag{4.42}$$

As our investigation closely resides on the previous analysis, we are going to assume, again, that we concentrate on slow body modes propagating with wavelengths that are shorter than the radius of the tube, i.e. we consider

waves in short wavelength limit. Here the phase speed of slow body modes is approaching the internal sound speed, C_S, therefore we can write that $\omega^2 \approx k^2 C_S^2(1-\nu)$, where ν is a small, but positive quantity. As a result, we have that

$$\nu = 1 - \frac{\omega^2}{k^2 C_S^2},$$

and the quantity ω/kC_S is the eigenvalue determined earlier. As a result, the governing equation becomes

$$u_z = \frac{P_T}{\rho_0 C_S} + \frac{V_A^2}{r(kR)^2 C_S}\frac{\partial}{\partial r}\left[\frac{r}{\rho_0(C_S^2 - V_A^2)}\frac{\partial P_T}{\partial r}\right] + \frac{V_A^2}{r^2(kR)^2 C_S}\frac{\partial}{\partial \theta}\left[\frac{1}{\rho_0(C_S^2 - V_A^2)}\frac{\partial P_T}{\partial \theta}\right]. \tag{4.43}$$

The coefficient function that appear in the terms on the right-hand side containing derivatives was written in terms of the parameters of the problem (see Eq. 4.18), so the governing equation leads to

$$u_z = (\gamma p_0(r,\theta)\rho_0(r,\theta))^{-1/2}\left\{P_T + \frac{\chi_B^2}{r(kR)^2}\frac{\partial}{\partial r}\left[rF(r,\theta)\frac{\partial P_T}{\partial r}\right] + \right.$$

$$\left. \frac{\chi_B^2}{r^2(kR)^2}\frac{\partial}{\partial \theta}\left[F(r,\theta)\frac{\partial P_T}{\partial \theta}\right]\right\}. \tag{4.44}$$

In this equation all quantities on the right-hand side were either determined earlier, or contain the chosen profiles of the plasma and field parameters, therefore the above equation allows us to study the spatial distribution of the LOS component of the velocity in an easy way.

4.7 Details of the numerical setup

Equation (4.44) will be solved numerically using the Galerkin FEM method. Given the particular form of this equation and the available values of the total pressure, it is more convenient to employ small quadratic triangular finite elements for numerical purposes rather than small linear triangular finite elements. The way the discretisation of the domain is carried out is shown in Fig. (4.10), where the upper panel displays the discretisation with linear triangular finite elements used to determine the values of the total pressure, and the lower panel shows the discretisation of the domain with quadratic triangular finite

elements used to determine the LOS velocity component.

In order to compute u_z, we must first compute the first and second order radial and azimuthal derivatives of the total pressure, P_T. Given that P_T was estimated using a linear combination of linear triangular elements, the second order derivatives of P_T would vanish. This leads us to the need of using a different approach to tackle this numerical problem, and the solution is provided by the use of quadratic triangle elements. Now the second order derivatives are calculated by interpolating the values of the total pressure using six nodes. This results in a more visually appealing but less accurate because, even in a uniform situation, we are unable to obtain the same u_z outcome as we obtained earlier for P_T, as P_T is an estimate value derived by linear interpolation rather than an exact value.

A two-dimensional finite element with coordinates is the quadratic triangular finite element. As illustrated in Fig. (4.9), a quadratic triangle consists of six nodes, each of which has two in-plane degrees of freedom. The sequence of

$$(x_1, y_1), (x_2, y_2), (x_3, y_3), (x_4, y_4), (x_5, y_5), (x_6, y_6),$$

represents the global coordinates of the six nodes. For our approach it matters which nodes are in which sequence for every element. The corner nodes should be mentioned first, followed by the midside nodes, in an anticlockwise direction. For the six nodes of each quadratic element the shape functions are given by

$$N_1 = \frac{\left(x_{23}\left(y - y_3\right) - y_{23}\left(x - x_3\right)\right)\left(x_{46}\left(y - y_6\right) - y_{46}\left(x - x_6\right)\right)}{\left(x_{23}y_{13} - y_{23}x_{13}\right)\left(x_{46}y_{16} - y_{46}x_{16}\right)},$$

$$N_2 = \frac{\left(x_{31}\left(y - y_1\right) - y_{31}\left(x - x_1\right)\right)\left(x_{54}\left(y - y_4\right) - y_{54}\left(x - x_4\right)\right)}{\left(x_{31}y_{21} - y_{31}x_{21}\right)\left(x_{54}y_{24} - y_{54}x_{24}\right)},$$

$$N_3 = \frac{\left(x_{21}\left(y - y_1\right) - y_{21}\left(x - x_1\right)\right)\left(x_{56}\left(y - y_6\right) - y_{56}\left(x - x_6\right)\right)}{\left(x_{21}y_{31} - y_{21}x_{31}\right)\left(x_{56}y_{36} - y_{56}x_{36}\right)},$$

$$N_4 = \frac{\left(x_{31}\left(y - y_1\right) - y_{31}\left(x - x_1\right)\right)\left(x_{23}\left(y - y_3\right) - y_{23}\left(x - x_3\right)\right)}{\left(x_{31}y_{41} - y_{31}x_{41}\right)\left(x_{23}y_{43} - y_{23}x_{43}\right)},$$

$$N_5 = \frac{\left(x_{31}\left(y - y_1\right) - y_{31}\left(x - x_1\right)\right)\left(x_{21}\left(y - y_1\right) - y_{21}\left(x - x_1\right)\right)}{\left(x_{31}y_{51} - y_{31}x_{51}\right)\left(x_{21}y_{51} - y_{21}x_{51}\right)},$$

$$N_6 = \frac{\left(x_{21}\left(y - y_1\right) - y_{21}\left(x - x_1\right)\right)\left(x_{23}\left(y - y_3\right) - y_{23}\left(x - x_3\right)\right)}{\left(x_{21}y_{61} - y_{21}x_{61}\right)\left(x_{23}y_{63} - y_{23}x_{63}\right)},$$

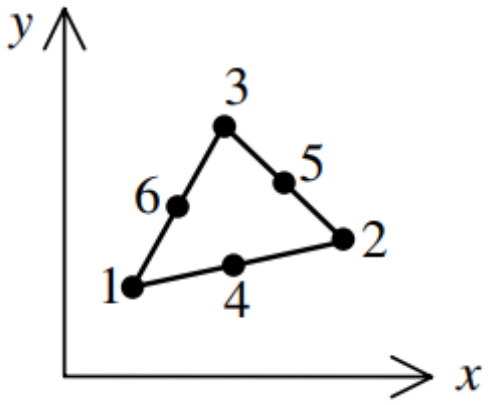

Figure 4.9: A schematic representation of quadratic triangular elements used to discretise the numerical domain.

where the midpoint values of $x_4 - x_6$ and $y_4 - y_6$ are calculated as $x_4 = (x_1+x_2)/2$, $y_4 = (y_1+y_2)/2$, $x_5 = (x_2+x_3)/2$, $y_5 = (y_2+y_3)/2$, $x_6 = (x_1+x_3)/2$ and $y_6 = (y_1 + y_3)/2$. Furthermore, we use $x_{jk} = x_j - x_k$ and $y_{jk} = y_j - y_k$.

4.7.1 Results

In this section we will examine how the spatial structure of the LOS velocity, u_z, is associated with slow body modes propagating in a cylindrical waveguide with inhomogeneous equilibrium under photospheric conditions, considering an isothermal plasma. Since the waves we are investigating propagate with wavelengths that are shorter than the radius of the flux tube, the sound speed, C_S, will be used to normalise the phase speed of the slow body wave modes in the presence of plasma inhomogeneity. The values of the LOS velocity are given by the governing equation (4.44), whose solutions are sought using a numerical approach. Given the particularity of the limit we are using, the dimensionless phase speed of modes will be slightly less than 1. Since the values of P_T are used in Eq. (4.44) are an estimate rather than an exact value obtained through linear interpolation, we are unable to obtain the same the values of u_z with same accuracy as we did for P_T, even in a uniform equilibrium situation. As a result of this, although we can draw conclusions on the spatial structure of the LOS velocity, the "inhomogeneous" aspect of u_z in the next few figures are apparent, resulting from the numerical analysis we

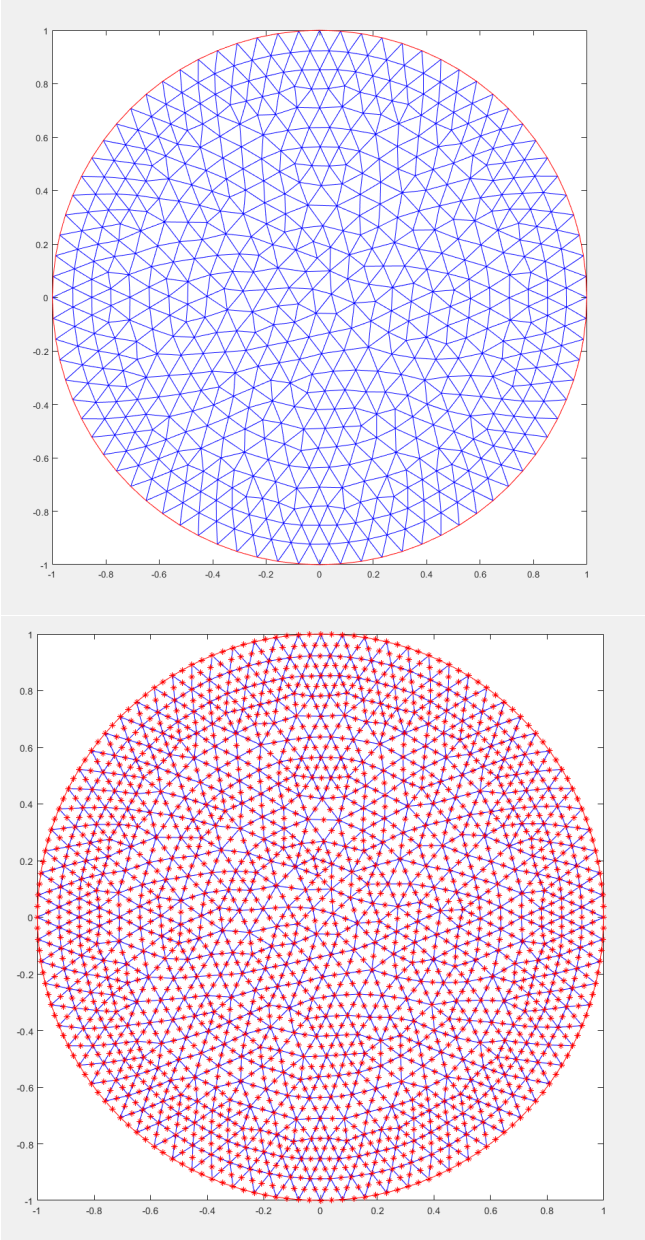

Figure 4.10: Mesh for linear and quadratic triangular elements used to determine numerically the values of the total pressure (upper panel) and LOS velocity component (lower panel).

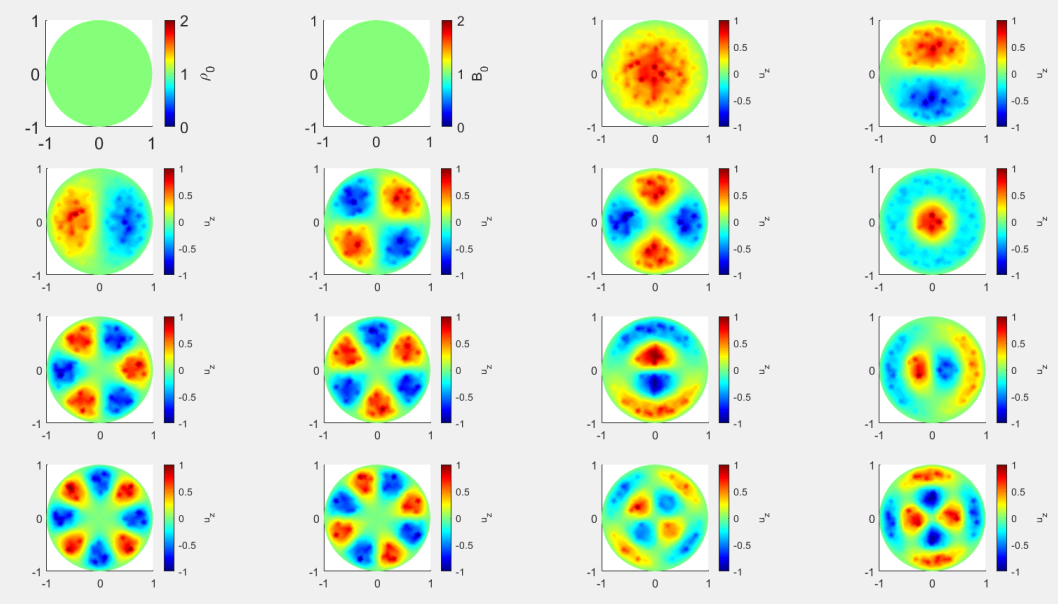

Figure 4.11: The spatial structure of the LOS velocity component corresponding to various slow body waves propagating in a homogeneous ($\sigma = 1$) cylindrical waveguide under photospheric conditions together with the density and magnetic field distribution (first two panels in the first row). The remaining panels show the spatial structure of the same slow body modes as in Fig. (4.1). The color bars display the normalised magnitude of the u_z. The red and blue shaded regions represent crests (maxima) and valleys (minima) of amplitude variation of u_z.

carried out. As before, the colour bars show the magnitude of the dimensionless amplitude of u_z. The amplitude's maxima and minima are represented by the shaded regions in red and blue, respectively. Our study will focus on the same modes of oscillation as before, with the equilibrium density inhomogeneity (enhancement and depletion) placed in a concentric and eccentric location and the results are displayed in Figs. (4.11)-(4.17). Given the way the LOS velocity is defined through Eq. (4.44) in terms of the total pressure, the spatial structure of the LOS velocity component will resemble the spatial structure we obtained for P_T, therefore being sensitive to the variations in the values of the radial distribution of equilibrium density, pressure, and magnetic field and the position of the inhomogeneities within the flux tube. In all the subsequent figures the modes are shown in descending order of their dimensionless phase speed.

The solutions obtained for the same modes as investigated before in the present chapter for the homogeneous case ($\sigma = 1$) are displayed in Fig. (4.11)

and these are used for reference to evidence the effect of inhomogeneities in density and magnetic field. Comparing Figs. (4.1) and (4.11) it is clear that the spatial structure of the LOS velocity corresponding to different slow body modes follows the patterns recovered for the total pressure and they present a clear symmetry.

When the inhomogeneous region has a concentric location, the spatial structure of the LOS velocity is shown by Fig. (4.12). It is clear that the spatial structures of recovered LOS velocity for the studied MHD modes are symmetric with respect to the center of the flux tube. The global nature of these modes can be readily identified, even though the spatial extent of the eigenfunction somewhat diminishes as a result of the concentric enhanced density loading that has been taken into consideration.

The spatial structures of u_z when the inhomogeneous region is placed in an eccentric position (along the horizontal direction and along the first bisector are shown by Figs. (4.13)-(4.14), with the parameters describing the inhomogeneity presented in Table 3.2), cases C2.2 and C2.3. Compared with the case of a concentric inhomogeneity distribution, the symmetry of u_z with respect to the centre of the flux tube is distorted, and the amplitude of the LOS velocity is higher in regions of lower (homogeneous) density. The location of the inhomogeneity will influence differently the orthogonal pairs of the same modes. Due to the considered density loading (and the presence of the inhomogeneous magnetic field), the spatial extent of the eigenfunctions shrinks and the global nature of these modes ceases. Comparing Figs. (4.11) and (4.13), it is evident that the oscillations are shifted, again, towards regions of lower density, so they become more localized. When the density inhomogeneity is shifted along an arbitrary direction (along the first bisector as in Fig. (4.14)), the modification in the spatial structure of modes remains qualitatively the same. One key conclusion that we can draw from these investigations is that the amplitudes of the distorted modes are not identical in every location, leading to a possible ambiguity of the mode identification based on observations.

In the case of a depleted density inhomogeneity, the maximum value of density of the inhomogeneous region is less than the density of the homogeneous part of the waveguide, i.e. we consider the case when $\sigma < 1$. The values of parameters used for our numerical investigations are given in Table (3.2), case C3. Figure (4.15, case C3.1) shows the spatial structure of the dimensionless amplitude of u_z corresponding to the same body modes as before in the case

of concentric loading, while Figs. (4.16, case C3.2) and (4.17, case C3.3) show the spatial structure of u_z for an eccentric loading, when the density inhomogeneity is placed along the horizontal axis and in a position along the first bisector.

The results obtained for these cases confirm the previous findings, namely, that in the case of an inhomogeneous distribution of the equilibrium plasma density and magnetic field, the modes tend to lose their global character, instead they become distorted, with the maximum value of the eigenfunction appearing in regions of the lowest density. However, in contrast to the C2 cases corresponding to density enhancement (concentric and eccentric), in this case, the modes tend to present a maximum eigenfunction in the region of equilibrium density inhomogeneity. The central symmetry of modes is distorted. As before, the spatial structure of slow body modes does not change if the density loading is placed along the horizontal or vertical axes, they undergo a rotational shift mimicking the change of the inhomogeneity location.

The migration of the location of modes and the distorted spatial structure of these modes in the presence of inhomogeneity reveals one important consequence for observations. A localized wave observation in a sunspot could be a way to identify the location of a density inhomogeneity in the umbral region, even if this inhomogeneity cannot be seen in observations.

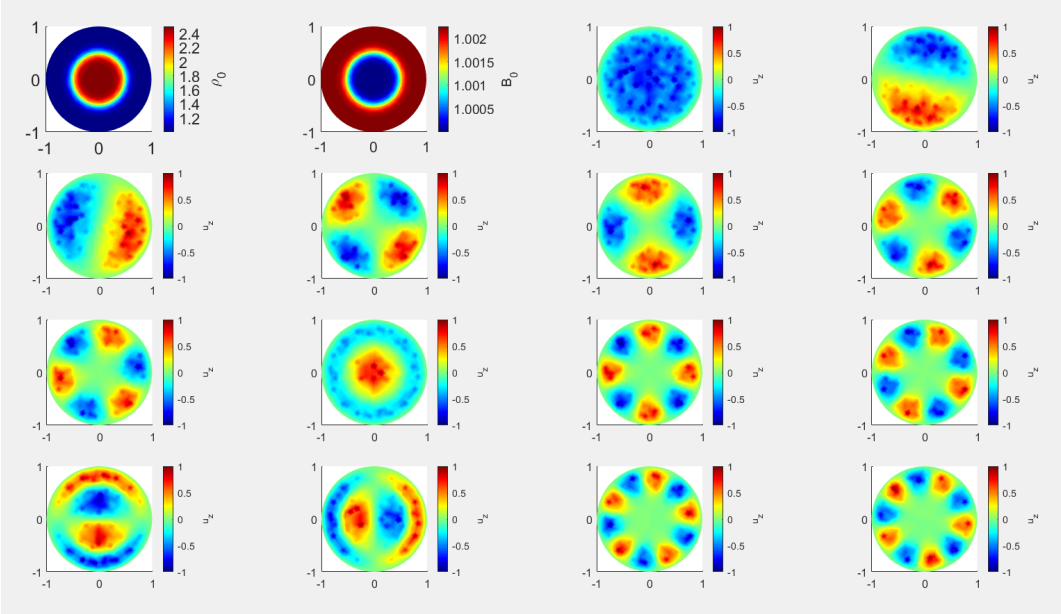

Figure 4.12: The spatial structure of the LOS velocity of the same modes as in Fig. (4.11), but here we show the results in the presence of a concentric density (and magnetic field) enhancement. All characteristic values of parameters used in these numerical solutions correspond to the case C2.1 in Table (4.1).

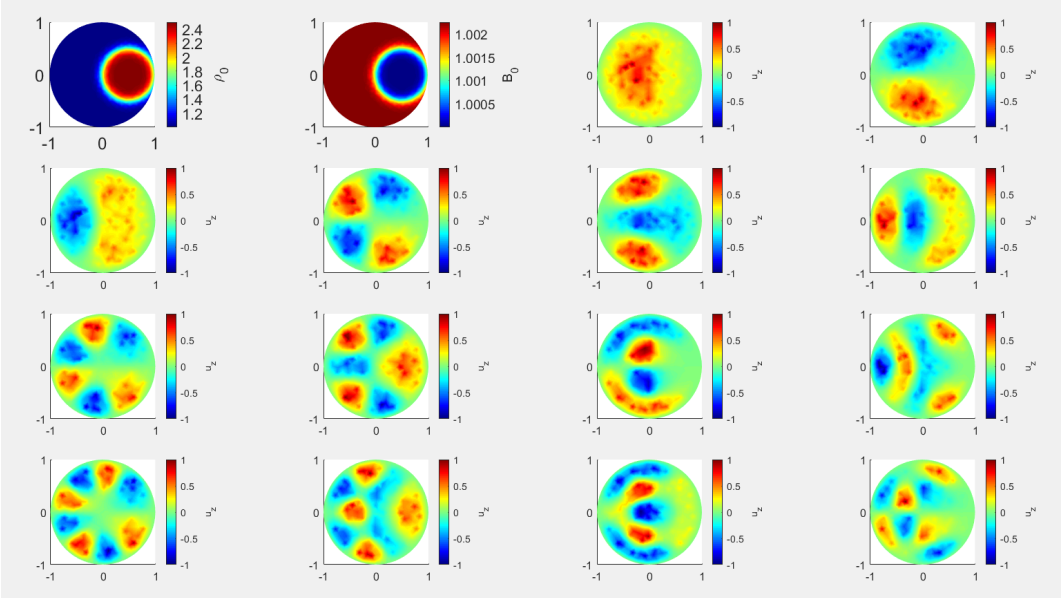

Figure 4.13: The spatial structure of the LOS velocity of the same modes as in Fig. (4.11), but here we show the results for an eccentric density (and magnetic field) loading, situated along the horizontal direction. The parameters used for this visualization are given as case C2.2 in Table (4.1).

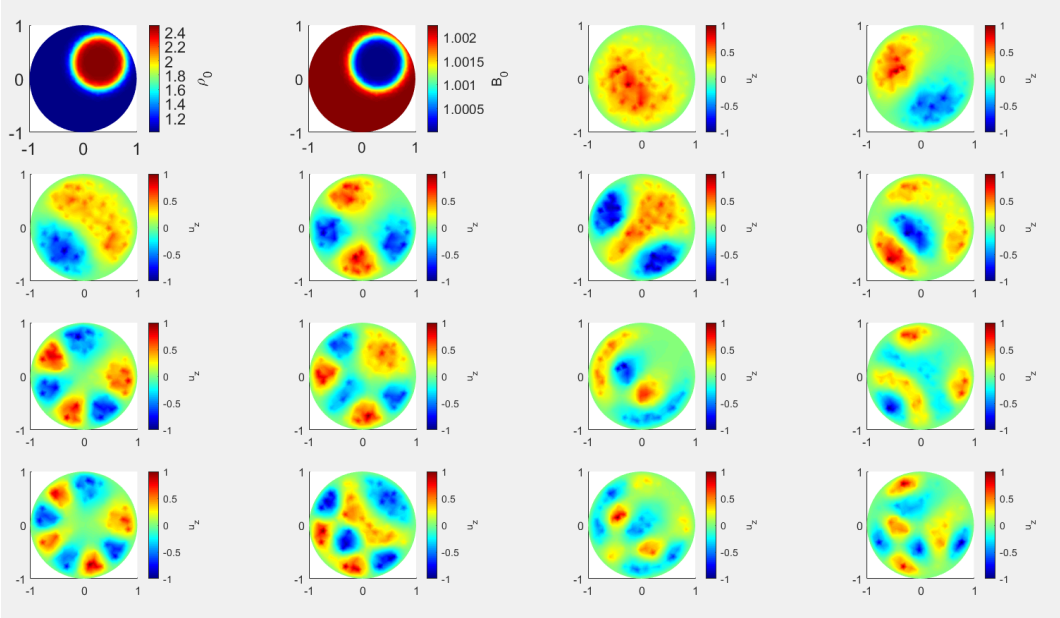

Figure 4.14: The spatial structure of the LOS velocity of the same modes as in Fig. (4.11), but here we show the results for an eccentric density loading (and magnetic field), situated along the bisector direction. The parameters used for this visualization are given by case C2.3 in Table (4.1).

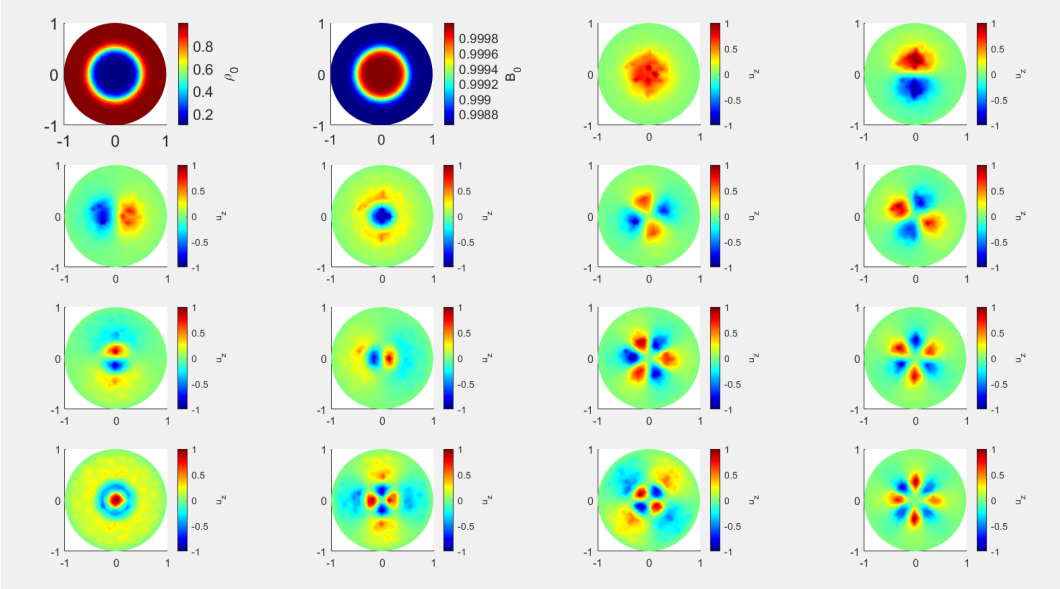

Figure 4.15: The spatial structure of the LOS velocity of the same modes as in Fig. (4.11), but here the depleted density region is situated in an eccentric position along the horizontal axis. The parameters used for this visualization are given as case C3.2 in Table (4.1).

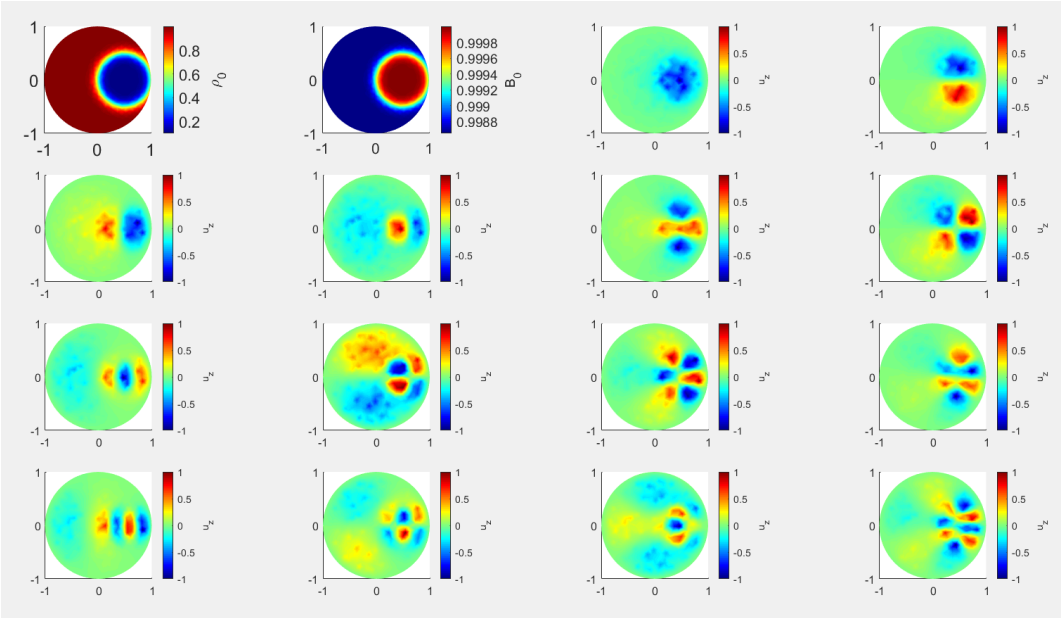

Figure 4.16: The spatial structure of the LOS velocity of the same modes as in Fig. (4.11), but here the depleted density region is situated in an eccentric position along the horizontal axis. The parameters used for this visualization are given as case C3.2 in Table (4.1).

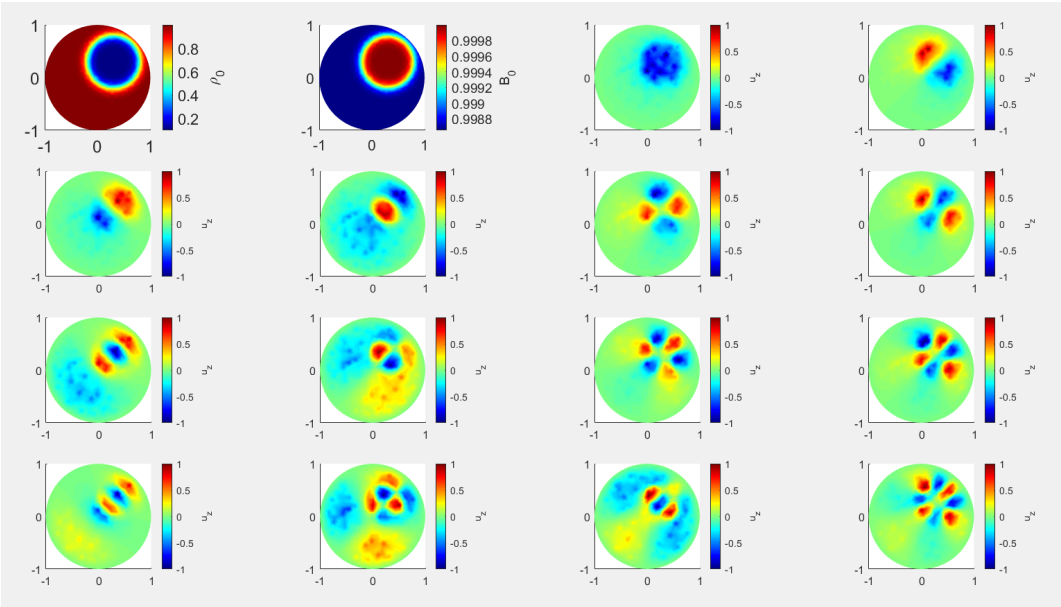

Figure 4.17: The spatial structure of the LOS velocity of the same modes as in Fig. (4.11), but here the depleted density region is situated in an eccentric position along the bisector axis. The parameters used for this visualization are given as case C3.2 in Table (4.1).

4.8 Conclusion

High resolution observations of the last few decades have shown that inhomogeneities in plasma and field parameters is one of the basic ingredients of magnetic flux tubes, from the solar photosphere to the solar corona. The mathematical description of wave propagation in such media is impossible, as the inhomogeneous character poses difficulties that cannot be resolved and the determination of the dispersion relation and properties of waves cannot be conducted. Numerical solutions to this complex problem are the only way forward and the determination of these solutions was the aim of this chapter that presents a study that attempts to close the gap in describing the properties of waves modelled in a realistic solar magnetic waveguide.

In this Chapter we extend the model used in Chapter (3), by considering not only the equilibrium density as function of coordinates, but also equilibrium pressure and magnetic field, in line with observations and numerical modelling. Analytical progress has been made by considering that the plasma pressure and density vary following the same dependency on coordinates, meaning that we are dealing with a constant sound speed, i.e. isothermal equilibrium. The equilibrium density profile inhomogeneity was represented by a local circular density enhancement or depletion whose strength, size and position can change. The profile of the equilibrium magnetic field has been determined based on the principle of force balance in the equilibrium state. Based on this physical requirement, it is clear that a decrease in the magnetic field would result from an increase in density or pressure due to the conservation of the equilibrium total pressure. We derive the Helmholtz-like governing equation with Dirichlet boundary condition and determine the eigenvalues and eigenvectors as a Sturm-Liouville problem. The Galerkin FEM method was employed to solve the governing equation.

In our analysis we concentrated on slow body waves in the short wavelength limit, therefore, all dimensionless speeds are converging to one, i.e. the constant sound speed. Our investigation dealt with the changes in the spatial structure of waves driven by the presence of inhomogeneity. As expected, under the assumption of a homogeneous equilibrium, the eigenmodes exhibit global harmonic oscillations and possess symmetrical characteristics along their respective axes. Inspired from the results presented in Chapter 3, where we showed that higher order modes are the most sensitive to the pres-

ence of localised inhomogeneities, here we analysed several higher order modes to provide a clearer picture of the impact of the considered inhomogeneities.

First of all, compared to the uniform equilibrium scenario, it is clear that the eigenvalues of the waves under study showed a very slight drop. The corresponding eigenmodes in the presence of concentric equilibrium density inhomogeneity are similar to those found in the case of uniform density and the modes show symmetry with respect to the circular waveguide's centre axis. The kink overtone and the fluting overtone of order $n = 2$ were the most affected modes.

The interaction between the inhomogeneous equilibrium magnetic field and density causes some intriguing patterns in the spatial structure of waves. The spatial structure of waves maintains its global character when compared to the spatial structures of modes we obtained when only the equilibrium density was taken into account (eccentric cases along the horizontal axis). However, the symmetry is distorted, making it impossible to categorise certain higher order modes based only on a visual inspection.

The inhomogeneity of the magnetic field will offset the effect of density inhomogeneity, in contrast to the results obtained in the case of only the inhomogeneous density. The recovered modes do not migrate towards lower density regions (as the regions where body wave solutions were allowed reduced). Modes tend to operate in the opposite way and have their greatest amplitude in the regions that correspond to higher densities. The modification of various higher order modes also depends on the direction in which the inhomogeneity is shifted with respect to the central symmetry axis, the degree of distortion is greater when the direction along which this inhomogeneity is moved coincides with the direction of wave polarisation.

In the presence of concentric equilibrium depletion density inhomogeneities, the corresponding eigenmodes display novel pattern features that differ from those observed in the case of uniform and concentric densities. As before, the eigenvalues exhibit a negligible drop in the presence of concentric non-uniform equilibrium density depletion. Compared to the case of uniform density augmentation, it may become harder to detect modes when their spatial structure shrinks, especially along the interior scattered nodes where the centres are more diminished. These results have important implications for optimising the structures that can be observed, compared, and correlated in observational data.

It is considerably more convenient from a practical standpoint to translate our results we obtained for the total pressure perturbation into quantities that are simpler to measure. Since many observational facilities can detect the Doppler-shift of intensity lines, depicting the spatial structure of the line-of-sight (LOS) component of the velocity is considerably closer to observations when it comes to wave activity. The eigenvalues and eigenfunctions determined for the total pressure were used to calculate the fluctuation of this LOS velocity component. Given the way the numerical recipe was constructed when determining P_T, the numerical approach used to find values of the LOS velocity had to be modified in the sense that the numerical domain was discretized into quadratic triangle elements. For the examined MHD modes, it is evident that the reconstructed LOS velocity's spatial structures are symmetric with regard to the flux tube's centre. Despite the fact that the concentric increased density loading that has been considered considerably reduces the spatial extent of the eigenfunction, it is still possible to identify the global character of these modes. A significant finding from these studies is that the distorted modes' amplitudes differ at different locations, which could cause confusion when identifying the modes based solely on observations.

Our investigations can be considered as a very first step in studying the properties of waves in sunspots and pores in the presence of local inhomogeneities in the form of umbral dots (UD) and light bridges (LB). Multistructure density distributions (as observations show) can often be replaced by a resulting structure that adequately captures the effects of multiple UDs present in the sunspot umbra. This means that the equilibrium density inhomogeneity profile is represented by a single local density inhomogeneity, which simulates the UDs observed in the sunspot umbra region, assuming that they are placed close to each other. Furthermore, the LB observed in sunspots can be modeled by a single local density inhomogeneity that separates the sunspot umbra region. The more complex the shape of the density inhomogeneity, the more complex the spatial structure of modes will become. As a result, the pattern of possible waves loses the high-degree of symmetry one can meet in homogeneous cases, especially for higher-order modes, which means that the pattern is no longer global and, therefore, cannot be easily identified. Local wave observations in sunspots may be a way to identify the location and size of density inhomogeneities in the umbra region.

The existence of the location of modes in the presence of density inhomo-

geneity determined for the density augmentation and depletion indicates one major consequence for observations. Even in cases when a density inhomogeneity in the umbral area is not visible in observations, the location of the inhomogeneity may be determined by means of a localised wave observation in a sunspot or pore.

CHAPTER 5

Slow body MHD waves in magnetic waveguides with multi-stranded inhomogeneities

All the waves studied so far in the present Thesis and all the models we have employed for inhomogeneities involved one single localised enhancement or depletion of density or magnetic field. In reality, though, inhomogeneities are much more complex, line intensity observations show that sunspots are pores covered by a number of inhomogeneities that appear as bright points in the umbral region. That is why, in this Chapter we will extend to inhomogeneities represented by a multi-stranded distribution of localised inhomogeneities.

5.1 Inhomogeneities in umbral regions of sunspots and pores: umbral dots and light bridges

As mentioned in the Chapter 4, transient photospheric phenomena, such as pores and sunspots with resolved inhomogeneities, do not have a single localised density distribution if they are positioned apart from one another. Since the resolved UDs are presumed to be somewhat far from one another, we thus assume that they can be modelled by using numerous strands of enhanced contour density distribution. Additionally, a single local density inhomogeneity that divides the sunspot umbra region can be used to simulate the LB seen in sunspots. As previously, an increase in density (or pressure) would result in a depletion of the magnetic field because of the necessity of maintaining the equilibrium total pressure.

A particular manifestation of inhomogeneities in pores and the umbral region of sunspots are UDs, which are regions of limited extent situated within

pores and the umbra of sunspots, believed to play an important role in the energy balance in sunspots (Solanki, 2003). They account for only $3\% - 10\%$ of the umbral area and $10\% - 20\%$ of its brightness (Watanabe et al., 2012). The majority of UDs appear to form close to the edge of the umbra and subsequently migrate towards the sunspots' centre at velocities of 700 m s^{-1} (Watanabe, 2014). UDs have a lifetime ranging from 2.5 to 10 min Riethmüller et al. (2008),Watanabe et al. (2009), Louis et al (2012). Based on their location, UDs are divided into central and peripheral dots. The magnetic fields of the peripheral UDs are weaker (and tilted) and they appear brighter than those situated in the centre. According to Watanabe et al. (2009), UDs appear when the magnetic field is weaker and inclined and disappear where it is the field becomes stronger and vertical. Using Hinode blue-continuum observations Watanabe (2014) found that, as sunspots progress, UDs become less dense and more clumped together. They also discovered that UDs migrate inward, their speeds are positively connected with the magnetic field inclination, and that UDs with longer lifetimes are typically larger and brighter.

Using observations by the New Vacuum Solar Telescope, Ji et al. (2016) showed that the lifetime of UDs located in several sunspots were correlated with the strength of the accompanying magnetic fields. They also found that the effective diameter, intensity, and velocity are affected by the fluctuation in the magnetic field. Yadav and Mathew (2018) performed a statistical comparison of the properties of UDs using Hinode observations of seven sunspots seen in high-resolution, G-band continuum filtergrams and they found that the average effective diameter of UDs is 270 km. The inhomogeneities, both in magnetic field and density, induced by UDs can drastically alter the frequency of waves and their propagation speed leading to a real challenge to identify the nature of waves and their properties. The physical parameters of UDs using high resolution observational data were studied in great detail by, e.g. Feng et al. (2015); Yadav and Mathew (2018); Kilcik et al. (2020).

Another form of localised inhomogeneities in sunspots and pores are light bridges (LB) that are bright features that divide umbral zones in two or more irregular regions. LBs typically show that magnetic zones are merging or, conversely, that the region is breaking up (Sobotka, 2003; Thomas and Weiss, 2004). LBs are structures that are frequently present during the creation or fragmentation of spots (Garcia de La Rosa, 1987). LBs can be thought of as either field-free hot plasma incursions into the umbral magnetic field (Parker,

1979; Choudhuri, 1986) or as large-scale magneto-convection manifestations in umbrae (Rimmele, 2008). The fine structure and energy transmission in sunspots are now mostly, if not completely, attributed to the latter hypothesis (Schüssler and Vögler, 2006; Cheung et al., 2010; Ortiz et al., 2010; van der Voort et al., 2010; Pozuelo et al., 2015). Magneto-convection in sunspots is further supported by the interaction between UDs and intruding penumbral filaments, which is frequently observed during the creation of LBs (Yukio et al., 2007; Louis et al., 2012). In this sense, LBs are a naturally occurring region of a sunspot where convective disruptions are more pronounced and obvious than elsewhere. Such a disruption might result in inhomogeneities that could account for the strong chromospheric activity in LBs that was described in studies by Louis et al. (2008) and Louis et al. (2014).

The inhomogeneities, both in magnetic field and density, induced by UDs or LBs can drastically alter the frequency of waves and their propagation speed leading to a real challenge to identify the nature of waves and their properties. The theory developed by Edwin and Roberts (1983*b*) predicts the qualitative behaviour of slow body waves under photospheric conditions, however it assumes an ideal case, when the plasma is homogeneous, static, and unbounded. High resolution observations show that these restrictions are not always realistic.

5.1.1 Slow body modes in the presence of multi-stranded density inhomogeneity distribution

Inspired from the results presented in the previous two chapters, we will expand our analysis to consider a circular waveguide in the presence of several localised density and magnetic field inhomogeneities. Similar to the model of Chapter 4, we are going to consider an isothermal equilibrium, where the equilibrium densities and pressures have the same coordinate dependence. The localised inhomogeneities considered in this chapter model the case of UDs in a sunspot.

The density of each individual strand is considered to have the same form as defined earlier, i.e.

$$\rho_{0i}(r,\theta) = \rho_2 \chi_i(r,\theta), \tag{5.1}$$

where ρ_2 is the homogeneous density of the annulus surrounding the inhomogeneous density distribution, the index i represent the sets of considered

inhomogeneities and $\chi_i(r,\theta)$ is the dimensionless quantity

$$\chi_i(r,\theta) = \left\{ 1 + \frac{(\sigma_i - 1)}{2} \left[1 - \tanh\left(\frac{\psi_i(r,\theta) - \tau}{\xi} \right) \right] \right\}$$

, σ_{0i} and σ_i describes the strength of the inhomogeneity and $\sigma_i > 1$ and $\sigma_i < 1$ denote an enhanced or depleteted density, respectively. In the above expression the function $\psi_i(r,\theta)$ contains information about the location of the inhomogeneity and takes the form

$$\psi_i(r,\theta) = \sqrt{(r\cos\theta - \epsilon_{1i})^2 + (r\sin\theta - \epsilon_{2i})^2},$$

where ϵ_{1i} and ϵ_{2i} describe the location of the center of the *i-th* density enhancement/depletion, τ is the ratio of the radii of the density inhomogeneity and the circular magnetic flux tube with $0 < \tau < 1$, ξ is the width of the annulus where the change of density occurs, i.e. gradual transition of density between two regions, and for simplicity we assume that the values of τ and ξ is identical for all density inhomogeneities. For simplicity the shape of all inhomogeneities are circular. The global inhomogeneity of the circular sunspot will be a quantity that will be used in the numerical analysis and it is defined as

$$\rho_0(r,\theta) = \frac{1}{N} \sum_{i=1}^{N} \rho_{0i}(r,\theta), \tag{5.2}$$

where N is the number of strands considered in the problem.

Since we consider an isothermal plasma, the equilibrium pressure will have the same coordinate dependence as density. The equilibrium pressure, in turn, will allow us to determine the distribution of the equilibrium magnetic field, in a similar fashion as in Chapter 4. Accordingly, the equilibrium magnetic field takes the form

$$B_{0i}(r,\theta) = B_0(\hat{r}_i, \hat{\theta}_i)\chi_{Bi}, \tag{5.3}$$

where

$$\chi_{Bi} = \left\{ 1 + \hat{\beta}_i \frac{\sigma_i - 1}{2} \left[\tanh\left(\frac{\psi_i(r,t) - \tau}{\xi} \right) - \tanh\left(\frac{\hat{\psi}_i - \tau}{\xi} \right) \right] \right\}^{1/2}, \tag{5.4}$$

and

$$\hat{\psi}_i = \sqrt{(\hat{r}_i \cos\hat{\theta}_i - \epsilon_{1i})^2 + (\hat{r}_i \sin\hat{\theta}_i - \epsilon_{2i})^2},$$

and the quantity β_2 is defined as $\hat{\beta}_i = p_2/[B_0^2(\hat{r}_i, \hat{\theta}_i)/(2\mu_0)]$ and

$$\hat{r}_i = (\epsilon_{1i}^2 + \epsilon_{2i})^{1/2}, \quad \hat{\theta}_i = \tan^{-1}(\epsilon_{2i}/\epsilon_{1i}).$$

The global magnetic field in the inhomogeneous waveguide, therefore, can be written as

$$B_0(r,\theta) = \frac{1}{N}\sum_{i=1}^{N} B_{0i}(r,\theta). \tag{5.5}$$

The eigenvalue problem solved in this chapter is identical with Eq. (4.18) and the numerical approach employed in this chapter is identical with the one detailed in Chapter 4 (see Section 4.7). For our numerical solutions we choose $N = 6$ localised inhomogeneities dispersed randomly across the cross-section of the waveguide. To evidence the effect of the multi-stranded inhomogeneities on the spatial structure of slow body waves, we will consider three particular cases: (1) when all density inhomogeneities have the same strength ($\sigma = 20$), and the location of inhomogeneities are chosen randomly (see Table 5.1); (2) the case when all density inhomogeneities are enhancement, but they take different values (see Table 5.2); and (3) for the same locations as the first two cases, but we chose three of the inhomogeneities to be depletions (see Table 5.3).

As before, due to the requirement of the conservation of the equilibrium total pressure, an enhancement/depletion in density (or pressure) would mean that the magnetic field will be depleted/enhanced.

5.1.2 Results and discussions

Figure (5.1) shows the distribution of equilibrium density and magnetic field in the first two panels and the parameters used for this simulation are given in Table (5.1). The modes present in this figure are shown in descending order of their dimensionless phase speed displayed on top of each panel. First of all, one important result of this simulation is that the spatial structure of fundamental sausage, kink and fluting modes (shown in the last two panels of the first row and the first three panels of the second row) are very little affected by the presence of inhomogeneities, meaning that describing these

Table 5.1: Values of the physical parameters used for the numerical modeling and analysis of modes in Fig. (5.1). For each case we consider $kR = 4$ and $\hat{\beta} = 3 \times 10^{-3}$, $\xi = 9.1 \times 10^{-2}$ and $\tau = 0.15$.

	σ	ϵ_1	ϵ_2
C1: enhanced density	20	-0.6	0.1
C2: enhanced density	20	0.6	0
C3: enhanced density	20	-0.3	-0.6
C4: enhanced density	20	0	0
C5: enhanced density	20	0.4	-0.6
C6: enhanced density	20	0	0.6

modes in a waveguide with homogeneous equilibrium would result in a fairly accurate description of these modes, both qualitatively and quantitatively. The inhomogeneities that represent the UDs have a much more pronounced effect on the higher order modes; we can observe a high degree of disorganisation of the spatial structure of modes and the loss of their symmetries. While sausage overtone (last panel of the second row) and the fluting mode $n = 3$ are recognisable in the first two panels of the third row, the pattern of the spatial structure of the remaining modes becomes too complicated to be diagnosed based on their symmetry.

Figure (5.2) displays the spatial structure of modes when the strength of the six density enhancements are different and their values are shown in Table (5.2). As before, the first two panels show the spatial distribution of the density and magnetic field inhomogeneities. While the fundamental sausage, kink modes are clearly very weakly affected (except one of the $n = 2$ fluting modes), all the other modes undergo a dramatic change in their spatial structure and their identification becomes challenging. The alteration of the spatial structure of modes is differentiated for the same orthogonaly polarised modes (see e.g. the $n = 3$ and $n = 4$ fluting mode in the first two panels of the third and fourth row, respectively). When comparing the results shown in Figs. (5.1) and (5.2), it is clear that having a distribution of inhomogeneous densities of different strengths will affect the higher order modes in a considerable way. It can be inferred that, in the case of more intricate configurations of inhomogeneity such as multi-structure systems the eigenfunctions will undergo alterations that correspond to the specific shape of the inhomogeneity being considered.

Finally, when the multi-stranded density inhomogeneity is represented by a mixture of localised density enhancements and depletions (seen in the first

Table 5.2: Values of the physical parameters used for the numerical modeling and analysis of modes shown in Fig. (5.2). For each case we consider $kR = 4$ and $\hat{\beta} = 3 \times 10^{-3}$, $\xi = 9.1 \times 10^{-2}$ and $\tau = 0.15$.

	σ	ϵ_1	ϵ_2
C1: enhanced density	20	-0.6	0.1
C2: enhanced density	15	0.6	0
C3: enhanced density	10	-0.3	-0.6
C4: enhanced density	5	0	0
C5: enhanced density	20	0.4	-0.6
C6: enhanced density	15	0	0.6

two panels of Fig. 5.3 with particular values used in the numerical analysis given in Table 5.3) the fundamental sausage and kink modes are practically unaffected, while the morphology of $n = 2$ fluting mode is changes, irrespective of its direction of polarisation (the second and third panel of the second row). The spatial structure of the sausage overtone obtained in this situation (fourth panel of the second row) is similar to the pattern we obtained for the case when all density inhomogeneities were enhancements, but different (see the fourth panel of the second row in Fig. 5.2), so for this mode the localised depletion of density does not have any effect. The $n = 3$ fluting mode seen in the first two panels of the third row behaves differently according to the direction of the polarisation. The kink overtone modes displayed in the last two panels of the third row undergo a slight change in their spatial structure. Unlike the previous two cases (all localised density are enhancements) the $n = 4$ fluting mode shown in the first two panels of the fourth row surprisingly maintain their symmetry, meaning that the depleted density inhomogeneities compensate for the distortions of density enhancements seen in Figs. (5.1) and (5.2), therefore the density depletions have the opposite effect as enhancements. The last two panels of the fourth row display the fluting overtone of order $n = 2$ and these confirm the above results, their spatial structure suffers a rather little change compared to the pattern we obtained for the homogeneous case (Fig. 4.1). Comparing the values of the dimensionless phase speeds in the two cases of a single localised and multi- stranded density distributions, it is obvious that density enhancement actually leaves the dimensionless phase velocity significantly unchanged. This is result could be attributed to the very small value of the plasma-β parameter in magnetic waveguides of strong intensity, such is in sunspots and pores. It is likely that the changes in the phase speed

Table 5.3: Values of the physical parameters used for the numerical modeling and analysis of modes in Fig. (5.3). For each case we consider $kR = 4$ and $\hat{\beta} = 3 \times 10^{-3}$, $\xi = 9.1 \times 10^{-2}$ and $\tau = 0.15$.

	σ	ϵ_1	ϵ_2
C1: enhanced density	8	-0.6	0.1
C2: enhanced density	10	0.6	0
C3: enhanced density	5	-0.3	-0.6
C4: depleted density	0.9	0	0
C5: depleted density	0.5	0.4	-0.6
C6: depleted density	0.1	0	0.6

could be more pronounced in waveguides where the plasma-β takes moderate values. Therefore, once density inhomogeneities are taken into account, the phase velocities of specific waves become much closer, making them difficult to distinguish from one another. This means that propagation speed of waves cannot be considered as a diagnostic tool for the slow body modes propagating in the photospheric waveguides.

The theoretical patterns of slow body modes obtained in our study could be used to identify modes in a different way. Similar to the study by Albidah et al. (2021*a*), the spatial structures of the modes obtained in the present Thesis can be used in conjunction with observational patterns of waves detected by various instruments and decomposed using the Proper Orthogonal Decomposition (POD) and Dynamic Mode Decomposition (DMD) methods. The nature of waves and oscillations can be determined using a goodness-of-fit test of by Pearson correlation. This method would indirectly allow us to determine the location of density inhomogeneities inside a photospheric waveguide.

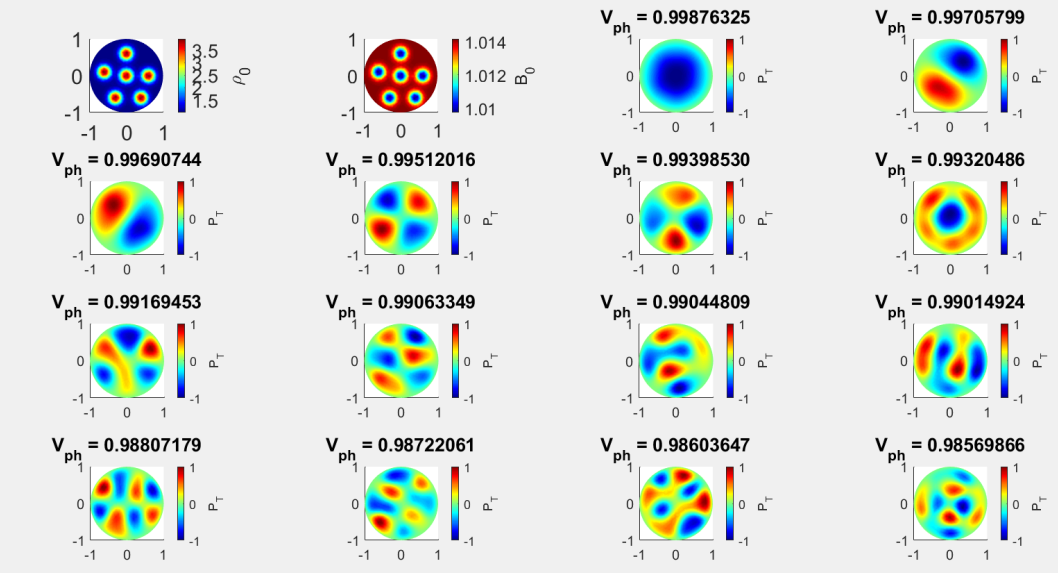

Figure 5.1: The same modes as in Fig. (4.1), but here we show the spatial structure of modes in the presence of the multi-stranded enhanced density distribution modelling UDs observed in the umbral region of sunspot. The inhomogeneous strands have the same strength. The numerical solutions were obtained for the particular values of the parameters shown in Table (5.1).

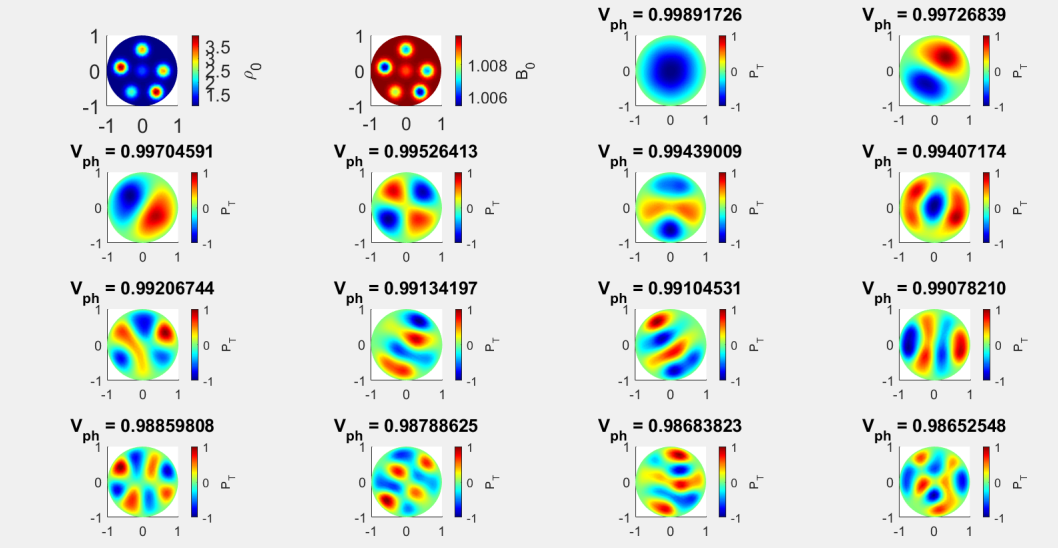

Figure 5.2: The same modes as in Fig. (5.1), but the inhomogeneous density distribution contains a mixture of enhanced regions of different strengths. The numerical solutions were obtained for the particular values of the parameters shown in Table (5.2).

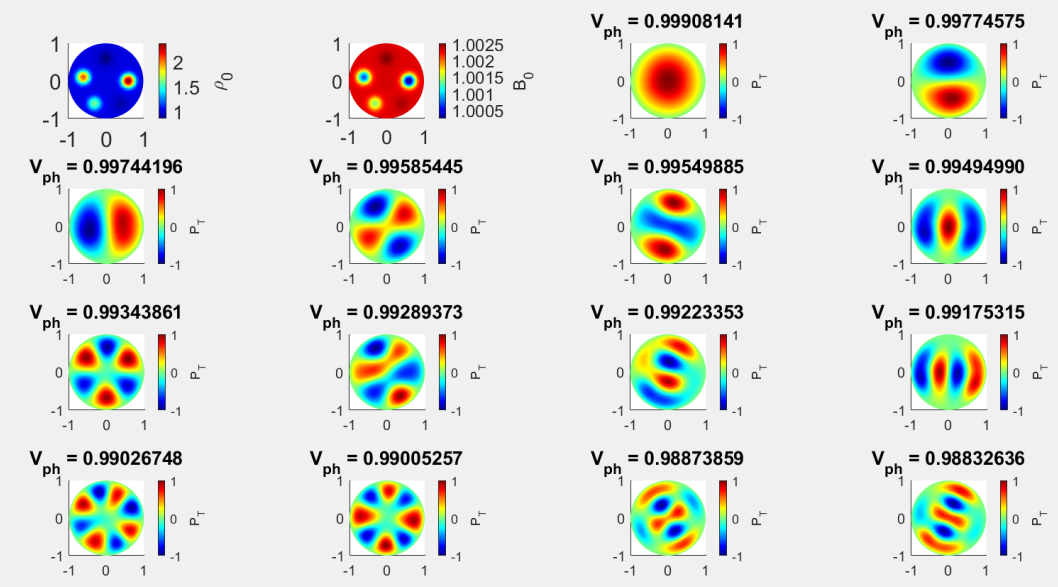

Figure 5.3: The same modes as in Fig. (5.1), but the inhomogeneous density distribution contains a mixture of enhanced and depleted regions. The numerical solutions were obtained for the particular values of the parameters shown in Table (5.3).

CHAPTER 6

Conclusions and possible future directions of research

6.1 Summary of findings

Intense magnetic waveguides in the solar photosphere, such as pores and sunspots are ideal environments for the propagation of guided waves. Waves are often used to diagnose the thermodynamic and plasma properties. The theory developed by Edwin and Roberts (1983*b*) predicts the qualitative behaviour of different waves in such environments, however it assumes an ideal case, when the plasma is homogeneous, static, and unbounded along the symmetry axis of the flux tube. Their model also assumes a high degree of symmetry. High resolution observations show that these restrictions are not always realistic. The present Thesis aimed to address these shortcomings and provide an in-depth analysis of the spatial structures of waves that can appear in inhomogeneous waveguides, where the inhomogeneity was present in the equilibrium density (pressure) and magnetic field.

6.1.1 Summary of Chapter 3

It is well-known that pores and sunspots are inhomogeneous, both in magnetic field and density. These inhomogeneities can drastically alter the frequency of waves and their propagation speed leading to a real challenge to identify the nature of waves and their properties. The research covered in this Chapter addresses the modification of the properties of waves (their phase speed or frequency, in particular) when a symmetric and geometrically well-defined inhomogeneity is considered that could model the umbral dots observed in the pores and the umbra region of sunspots. In order to simplify the problem we employed a result by Aldhafeeri et al. (2022*a*), who showed that in the case of slow body waves under photospheric conditions the dispersive character of waves and their properties can be confidently described by solving a Helmholtz-type differential equation with Dirichlet boundary condition, i.e. we assumed that the total pressure perturbation (and implicitly the longitudinal

component of velocity) vanishes at the boundary of the waveguide. In addition, we assumed a situation when the wavelength of waves is much smaller (and later much larger) than the radius of the tube (als known as the short/long wavelength limit). The frequency as well as the eigenfunctions related to the studied waves were investigated as a Sturm-Liouville eigenvalue problem and the governing equation with non-constant coefficients was solved numerically using the Fourier-Chebyshev spectral method. As the inhomogeneous equilibrium plasma density considered here was described by a series of parameters that determine the size, the strength and location of the inhomogeneity, we conducted a parametric study with the aim to highlight what effects these parameters have on the characteristics of waves. In order to provide a general approach, we have considered both cases of an enhanced and depleted equilibrium plasma density. Since we assumed waveguides for which the equilibrium plasma pressure is constant, these density changes would appear as dark or bright regions inside a magnetic waveguide.

First, we analysed the case of short wavelength limit, i.e. when the wavelength of slow body waves under photospheric conditions is much smaller than the radius of the tube. Inspired from the results by Edwin and Roberts (1983*b*) we expect that in this limit the phase speed of waves is slightly less than the sound speed. With a constant sound speed assumed in our model, this assumption remains perfectly viable. Our results indicate that a significant change driven by the inhomogeneous equilibrium plasma density is the modification in the spatial structure of waves. A direct consequence of the particular density distribution is that slow body waves in cylindrical waveguides lose their global character, instead, they become more localized and always tend to appear in the regions that correspond to a lower density. This property might help identify locations of density inhomogeneity when these are not visible in intensity spectral lines.

The parameters that describe the equilibrium plasma density modification (strength, location, size, smoothness of the transition to a homogeneous density) affect the modes in different ways. In general, the eigenfrequencies of fluting modes were shown to be more sensitive to the modifications of the equilibrium plasma density parameters. In the case of depleted density, the modifications in the phase speed of waves is more significant (nearly 40% decrease) and the differentiation between different modes according to the size of the inhomogeneity or its location very often is very small, meaning that for modeling purposes one can choose the most convenient location for equilibrium plasma density inhomogeneity.

In the long wavelength limit (when the phase speed of slow waves approaches the internal tube speed, or the slender tube model) the changes in the phase speed of waves is small, similar to the changes we had in the short wavelength limit. However, in this limit the most important change is in the modifications in the spatial structure of modes. For an enhanced density inhomogeneity waves remain global in nature, however they lose their symmetry.

These findings can lead us to conclude that, in contrast to the short-wavelength limit, the spatial structure of the slow-body modes in the long-wavelength limit exhibits less alterations because of the variations in the phase velocity of the slow-body modes vary slightly over the long wavelength limit. When the inhomogeneous equilibrium density presents itself as a depleted region, the spatial structure of waves is similar to the results found in the short wavelength limit.

The analysis and the numerical recipe discussed in this chapter can be considered as a starting point in the investigation of waves in realistic solar photospheric waveguides, where the equilibrium plasma density inhomogeneity derived from observations or realistic sunspot simulations can be incorporated in the study of the properties of slow body waves. The present analysis can be considered as a tool for diagnosing the inhomogeneous character of sunspots or pores, however this diagnosis is rather qualitative, rather than quantitative. The choice of a waveguide of high symmetry is not entirely realistic, however it allows us to use a fairly simple mathematical approach and the obtained results show the modifications of the properties of waves due solely to the density inhomogeneity. It is known (see, e.g. Albidah et al., 2021*b*, 2022*b*) that the irregular shape of the waveguides has very serious effects on the spatial structure of waves, especially in the case of higher order modes. The constant plasma-β limit considered here is also a rather crude approximation. Observations show (see, e.g. Gary, 2001; Grant et al., 2018) that the plasma-β changes over small spatial scales, and around the density inhomogeneities this quantity may exhibit a sharp gradient that could influence the property of waves studied by us.

6.1.2 Summary of Chapter 4

In this Chapter we extended the model used in Chapter 3, by considering not only the equilibrium density as function of coordinates, but also equilibrium pressure and magnetic field, in line with observations and numerical modelling. Analytical progress was made by considering that the plasma pressure and density vary following the same dependency on coordinates, meaning that we are dealing with a constant sound speed, i.e. isothermal equilibrium. The equilibrium density profile inhomogeneity was represented by a local circular density enhancement or depletion whose strength, size and position can change. Using the requirement of the conservation of the total pressure, the magnetic field aligned with the symmetry axis of the tube was determined. Naturally, a decrease in the magnetic field would result from an increase in density or pressure. We derived a Helmholtz-like governing equation that has been solved numerically (by means of the Galerkin FEM method) by imposing, again, Dirichlet boundary conditions for the total pressure perturbation. This equation was adequate to allow us to determine the eigenvalues and eigenvectors as a Sturm-Liouville problem.

Since we are dealing with a short wavelength limit, all dimensionless speeds

are converging to one, i.e. the constant sound speed. Inspired from the results obtained in Chapter 3 that showed that inhomogeneities are affecting more dramatically the higher order modes, we displayed the results for several higher order modes in addition to the three modes analysed earlier to provide a clearer picture of the impact of the considered inhomogeneities here.

First of all, compared to the uniform scenario, it is clear that the eigenvalues of the waves under study showed a very slight drop. The corresponding eigenmodes in the presence of concentric equilibrium density inhomogeneity are identical to those found in the case of uniform density, i.e. the modes show symmetry with respect to the central axis of the circular waveguides. Our results show that the eigenvalues of modes gradually decrease in the presence of a concentric inhomogeneous equilibrium density enhancement; however, the oscillating modes exhibit global harmonic oscillations character in contrast to the case where the density enhancement was the only inhomogeneity. The kink overtone and the fluting overtone of order $n = 2$ seem to be the most affected modes. The interaction between the magnetic field and inhomogeneous density causes some intriguing patterns in the wave's spatial structure. The symmetry of higher order modes is distorted, making it impossible to categorise them based only on a visual inspection.

Comparing the obtained results with the corresponding findings listed in Chapter 3 indicate that the inhomogeneity of the magnetic field will offset the effect of density inhomogeneity, modes no longer migrate towards lower density regions. While all other modes tend to operate in the opposite way, that is, to have their greatest amplitude in the regions that correspond to higher densities, fundamental sausage, kink, and fluting modes tend to exhibit a tendency to have larger amplitude in the lower density regions.

In the presence of concentric equilibrium depletion density inhomogeneities the corresponding eigenmodes display novel pattern features that differ from those observed in the case of uniform and concentric densities. The eigenvalues exhibit a negligible drop in the presence of concentric non-uniform equilibrium density loss, as the aforementioned data show. Compared to the case of uniform density augmentation, it may become harder to detect modes when their spatial structure shrinks, especially along the interior scattered nodes where the centres are more diminished. These results have important implications not only for building and organising modes in circular structures, but also for optimising modal structures that can be observed, compared, and correlated in data.

It is considerably more convenient from a practical standpoint to translate our total pressure perturbation results into numbers that are simpler to measure. Since several observational facilities are equipped to measure the Doppler shift of spectral intensity lines, depicting the spatial structure of the line-of-sight (LOS) component of the velocity is considerably closer to observations when it comes to wave activity. The eigenvalue and eigenfunction values (here, the total pressure) that were previously obtained were used to calculate the

fluctuation of this quantity. The numerical method used to solve this problem was modified by using quadratic triangle elements to discretise the numerical domain. For the examined MHD modes, it is evident that the spatial structure of the reconstructed LOS velocity is symmetric with regard to the flux tube's centre. Despite the fact that the concentric increased density loading that has been considered considerably reduces the spatial extent of the eigenfunction, it is still possible to identify the global character of these modes. A significant finding from these studies is that the distorted modes' amplitudes differ at different locations, which could cause confusion when identifying the modes based solely on observations.

The existence of the location of modes in the presence of density inhomogeneity determined for the density ehnacement and depletion indicates one major consequence for observations. Even in when a density inhomogeneity in the umbral area is not visible in observations, the location of the inhomogeneity may be determined by means of the observation of localised waves in a sunspot.

6.1.3 Summary of Chapter 5

Spectral line intensity observations reveal that sunspots and pores are very often covered by several inhomogeneities that look as bright regions in the umbral area. In this Chapter we broaden our study to take into account a circular waveguide in the presence of a multi-stranded distribution of localised inhomogeneities, drawing inspiration from the findings reported in the preceding two chapters. We analysed an isothermal equilibrium, in which the equilibrium densities and pressures have the same coordinate dependency, as in the model of Chapter 4. The inhomogeneities considered in this chapter could model the UDs in a sunspot. For modelling purposes we modelled out inhomogeneity by several strands of both enhanced and depleted density distributions. To be able to use the results presented in previous chapters, we have introduced a global density and magnetic field. As previously, an increase in density (or pressure) would result in a depletion of the magnetic field because of the necessity of maintaining the equilibrium total pressure.

The numerical method used in this chapter is the same as that described in Chapter 4 (see Section 4.7), and the eigenvalue problem solved in this chapter is identical with Eq. (4.18). We selected $N = 6$ localised inhomogeneities distributed randomly across the waveguide's cross-section. To have a sense of generality of our results, we investigated three specific situations to analyse how multi-strand inhomogeneities affect the spatial structure of slow body waves. Our results showed that the propagation speeds are smaller in the context of the UDs equilibrium density inhomogeneity than they are in the homogeneous situation. As a result, with respect to the spatial structure of global oscillation, the morphology of low order eigenmodes remains fairly intact, however the spatial structure of higher order modes is rather distorted.

These results carry important implications for observations and the ability of observers to correctly identify the oscillating modes in a sunspot or pore.

6.2 Future work

Inspired by our findings, one can identify various avenues along which new kinds of investigations can be drafted as a natural extension of the presented research, but also a few other directions that stem from the methods developed here.

- Our investigations contained several simplifications that allowed us to derive an analytical eigenvalue equation that was solved numerically. These equations were relevant to specific cases when the wavelength of waves was much larger or much shorter than the radius of the waveguide. There is clearly a difference between the spatial structure of slow body waves in the two limits, and an investigation for the case when the wavelength of waves is comparable with the radius of the tube would provide the bridge between the two cases, it would help us better understand the way the morphology of oscillations is changing.

- Observations clearly show that, in reality, the cross-section of sunspots is not regular, sometimes the closest symmetric shape of a sunspots or pore resembles the one of an ellipse. Determining a relevant wave solution for the MHD equations in a realistic waveguide with an elliptical and irregular cross sectional structure is the important step towards understanding and assessing the behaviour of MHD observed in the solar environment. Wave characteristics and their dispersion curves are sensitive to the waveguide's transversal geometry, as shown by a comparison of the solutions of the dispersion relations for regular circular and elliptical cross-sections Aldhafeeri et al. (2021) and Albidah et al. (2022*b*). Once the possible theoretical modes in a realistic waveguide have been determined, these can be compared with the modes recovered after applying the Proper Orthogonal Decomposition (POD) and Dynamic Mode Decomposition (DMD) techniques to observational data. Various correlation techniques can be applied to identify the modes, as well as their contribution to the overall signal.

- Our analysis can be expended also in the direction of analytical investigation. The presence of a circular cross-section inhomogeneity (as assumed in the present Thesis) in a circular waveguide can be modelled as a system of co-axial waveguides, where a homogeneous cylindrical magnetic flux tube of radius r_1 is embedded in a larger homogeneous magnetic cylinder of radius r_2 with $r_1 = \tau r_2$ and $\tau < 1$. The densities of the two cylinders is homogeneous, however there is a sharp transition at the

boundary r_1. Proper boundary conditions have to be applied at the interface r_1 (continuity of the radial component of the velocity and total pressure) and at the outer surface of the system, r_2, toghether with the requireemnt that at $r > r_2$ waves are evanescent. This complex system will allow us to study not only body waves, but also surface waves.

- The inhomogeneity profiles used in the present Thesis were assumed to be circular ($a = b = 1$ in Eqs. 3.16-3.17). Observations clearly show that UDs are not really circular, instead they tend to be elliptical. That is why the above investigation can be expanded by considering inhomogeneities of elliptical shape, that would require a new determination of the profiles of the magnetic field that satisfy the condition of conservation of the total pressure. In an extreme conditions the parameters a and b can be modified so that the inhomogeneity becomes an elongated elliptical structure that could model a light bridge. The large number of parameters in the expression of the inhomogeneous density allow us to place this inhomogeneity in an arbitrary location, mimicking a real situation of a light bridge.

- Additional developments of the analysis presented in this Thesis might involve simulating asymmetric profiles, such as non-steady asymmetric background plasma flows, which would require some adjustments to the physics of MHD wave modes in the sense that the obtained frequencies will be all Doppler shifted. Line of sight observations of plasma flows in sunspots are continuously observed, therefore such an addition would bring the modelling much closer to reality.

References

Albidah, A. B., Brevis, W., Fedun, V., Ballai, I., Jess, D. B., Stangalini, M., Higham, J. and Verth, G. (2021*a*), 'Proper orthogonal and dynamic mode decomposition of sunspot data', *Philosophical Transactions of the Royal Society A* **379**(2190), 20200181.

Albidah, A. B., Fedun, V., Aldhafeeri, A. A., Ballai, I., Brevis, W., Jess, D. B., Higham, J., Stangalini, M., Silva, S. S. A. and Verth, G. (2022*a*), 'Magnetohydrodynamic Wave Mode Identification in Circular and Elliptical Sunspot Umbrae: Evidence for High-order Modes', *Astrophys. J.* **927**(2), 201.

Albidah, A., Brevis, W., Fedun, V., Ballai, I., Jess, D., Stangalini, M., Higham, J. and Verth, G. (2021*b*), 'Proper orthogonal and dynamic mode decomposition of sunspot data', *Philosophical Transactions of the Royal Society A* **379**(2190), 20200181.

Albidah, A., Fedun, V., Aldhafeeri, A., Ballai, I., Brevis, W., Jess, D., Higham, J., Stangalini, M., Silva, S. and Verth, G. (2022*b*), 'Magnetohydrodynamic wave mode identification in circular and elliptical sunspot umbrae: Evidence for high-order modes', *The Astrophysical Journal* **927**(2), 201.

Aldhafeeri, A. A., Verth, G., Brevis, W., Jess, D. B., McMurdo, M. and Fedun, V. (2021), 'Magnetohydrodynamic wave modes of solar magnetic flux tubes with an elliptical cross section', *The Astrophysical Journal* **912**(1), 50.

Aldhafeeri, A. A., Verth, G., Fedun, V., Lennard, M. and Ballai, I. (2022*a*), 'Comparison of exact and approximate mhd slow body mode solutions in photospheric waveguides', *The Astrophysical Journal* **938**(1), 32.

Aldhafeeri, A. A., Verth, G., Fedun, V., Lennard, M. and Ballai, I. (2022*b*), 'Comparison of Exact and Approximate MHD Slow Body Mode Solutions in Photospheric Waveguides', *Astrophys. J.* **938**(1), 32.

Aschwanden, M. (2004), 'Physics of the solar corona. an introduction, ed. aschwanden, mj'.

Asiri, F., Ballai, I., Fedun, V., Verth, G., Ruzheinikov, S. and Albidah, A. (2024), 'Slow body magnetohydrodynamic waves in solar photospheric flux tubes with density inhomogeneity', *Monthly Notices of the Royal Astronomical Society* p. stae497.

Ballai, I. (2007), 'Global Coronal Seismology', *Solar Phys.* **246**(1), 177–185.

Ballai, I., Erdélyi, R. and Goossens, M. (2000), 'Linear and nonlinear resonant interaction of sound waves in dissipative layers', *Journal of Plasma Physics* **64**(3), 235–247.

Ballai, I., Erdélyi, R. and Hargreaves, J. (2006), 'Slow magnetohydrodynamic waves in stratified and viscous plasmas', *Physics of Plasmas* **13**(4), 042108.

Ballester, J. L. (2005), 'Theoretical Advances in Prominence Seismology', *Space Sci. Rev.* **121**(1-4), 105–113.

Banerjee, D., Krishna Prasad, S., Pant, V., McLaughlin, J. A., Antolin, P., Magyar, N., Ofman, L., Tian, H., Van Doorsselaere, T., De Moortel, I. and Wang, T. J. (2021), 'Magnetohydrodynamic Waves in Open Coronal Structures', *Space Sci. Rev.* **217**(7), 76.

Beckers, J. M. and Tallant, P. E. (1969), 'Chromospheric inhomogeneities in sunspot umbrae', *Solar Physics* **7**, 351–365.

Beckers, J. and Schultz, R. (1972), 'Oscillatory motions in sunspots', *Solar Physics* **27**(1), 61–70.

Bhatnagar, A. (1971), On the oscillatory velocity field in sunspot atmosphere., *in* 'Bulletin of the American Astronomical Society', Vol. 3, p. 259.

Bhatnagar, A. and Tanaka, K. (1972), 'Intensity oscillation in hα-fine structure', *Solar Physics* **24**(1), 87–97.

Bose, S., Joshi, J., Henriques, V. M. and van der Voort, L. R. (2021), 'Spicules and downflows in the solar chromosphere', *Astronomy & Astrophysics* **647**, A147.

Briard, A., Gréa, B.-J. and Nguyen, F. (2024), 'Turbulent mixing in the vertical magnetic rayleigh–taylor instability', *Journal of Fluid Mechanics* **979**, A8.

Chen, G., Guo, Y., Ding, M. and Erdélyi, R. (2023), 'Measuring local physical parameters in coronal loops with spatial seismology'.

Cheung, M., Rempel, M., Schüssler, M. et al. (2010), 'Simulation of the formation of a solar active region', *The Astrophysical Journal* **720**(1), 233.

Choudhuri, A. R. (1986), 'The dynamics of magnetically trapped fluids. i. implications for umbral dots and penumbral grains', *The Astrophysical Journal* **302**, 809–825.

Christopoulou, E., Skodras, A., Georgakilas, A. and Koutchmy, S. (2003), 'Wavelet analysis of umbral oscillations', *The Astrophysical Journal* **591**(1), 416.

Cowling, T. G. (1976), 'Magnetohydrodynamics'.

Cristaldi, A., Guglielmino, S., Zuccarello, F., Romano, P., Falco, M., van der Voort, L. R., de la Cruz Rodriguez, J., Ermolli, I. and Criscuoli, S. (2014), 'Dynamic properties along the neutral line of a delta spot inferred from high-resolution observations', *The Astrophysical Journal* **789**(2), 162.

De Moortel, I. and Browning, P. (2015), 'Recent advances in coronal heating', *Philosophical Transactions of the Royal Society of London Series A* **373**(2042), 20140269–20140269.

De Moortel, I. and Nakariakov, V. M. (2012), 'Magnetohydrodynamic waves and coronal seismology: an overview of recent results', *Philosophical Transactions of the Royal Society of London Series A* **370**(1970), 3193–3216.

De Pontieu, B., McIntosh, S., Carlsson, M., Hansteen, V., Tarbell, T., Schrijver, C., Title, A., Shine, R., Tsuneta, S., Katsukawa, Y. et al. (2007), 'Chromospheric alfvénic waves strong enough to power the solar wind', *Science* **318**(5856), 1574–1577.

De Pontieu, B., Testa, P., Martínez-Sykora, J., Antolin, P., Karampelas, K., Hansteen, V., Rempel, M., Cheung, M. C., Reale, F., Danilovic, S. et al. (2022), 'Probing the physics of the solar atmosphere with the multi-slit solar explorer (muse). i. coronal heating', *The Astrophysical Journal* **926**(1), 52.

Edwin, P. M. and Roberts, B. (1983*a*), 'Wave Propagation in a Magnetic Cylinder', *Solar Phys.* **88**(1-2), 179–191.

Edwin, P. and Roberts, B. (1982*a*), 'Wave propagation in a magnetically structured atmosphere', *Solar Physics* **76**(2), 239–259.

Edwin, P. and Roberts, B. (1982*b*), 'Wave propagation in a magnetically structured atmosphere', *Solar Physics* **76**(2), 239–259.

Edwin, P. and Roberts, B. (1983*b*), 'Wave propagation in a magnetic cylinder', *Solar Physics* **88**(1), 179–191.

Edwin, P. and Roberts, B. (1983*c*), 'Wave propagation in a magnetic cylinder', *Solar Physics* **88**(1-2), 179–191.

Enerhaug, E., Howson, T. A. and De Moortel, I. (2024), 'Identifying alfvén wave modes in the solar corona', *Astronomy & Astrophysics* **681**, L11.

Erdélyi, R. and Ballai, I. (2007), 'Heating of the solar and stellar coronae: a review', *Astronomische Nachrichten* **328**(8), 726–733.

Feng, S., Zhao, Y., Yang, Y., Ji, K., Deng, H. and Wang, F. (2015), 'Identifying and Tracking of Peripheral and Central Umbral Dots', *Solar Phys.* **290**(4), 1119–1133.

Garcia de La Rosa, J. (1987), 'Umbral dots: A case of penetrative convection between sunspot fragments', *Solar physics* **112**(1), 49–58.

Gary, G. A. (2001), 'Plasma beta above a solar active region: rethinking the paradigm', *Solar Physics* **203**, 71–86.

Gilchrist-Millar, C. A., Jess, D. B., Grant, S. D., Keys, P. H., Beck, C., Jafarzadeh, S., Riedl, J. M., Van Doorsselaere, T. and Ruiz Cobo, B. (2021), 'Magnetoacoustic wave energy dissipation in the atmosphere of solar pores', *Philosophical Transactions of the Royal Society A* **379**(2190), 20200172.

Goedbloed, H., Goedbloed, J., Keppens, R. and Poedts, S. (2019), *Magnetohydrodynamics: Of Laboratory and Astrophysical Plasmas*, Cambridge University Press.

Goedbloed, J. H., Goedbloed, J. and Poedts, S. (2004), *Principles of magnetohydrodynamics: with applications to laboratory and astrophysical plasmas*, Cambridge university press.

Goedbloed, J. P., Keppens, R. and Poedts, S. (2010), *Advanced magnetohydrodynamics: with applications to laboratory and astrophysical plasmas*, Cambridge University Press.

Goossens, M., Hollweg, J. V. and Sakurai, T. (1992), 'Resonant behaviour of mhd waves on magnetic flux tubes', *Solar physics* **138**(2), 233–255.

Grant, S. D., Jess, D. B., Zaqarashvili, T. V., Beck, C., Socas-Navarro, H., Aschwanden, M. J., Keys, P. H., Christian, D. J., Houston, S. J. and Hewitt, R. L. (2018), 'Alfvén wave dissipation in the solar chromosphere', *Nature Physics* **14**(5), 480–483.

Grant, S., Jess, D., Moreels, M., Morton, R., Christian, D., Giagkiozis, I., Verth, G., Fedun, V., Keys, P., Van Doorsselaere, T. et al. (2015), 'Wave damping observed in upwardly propagating sausage-mode oscillations contained within a magnetic pore', *The Astrophysical Journal* **806**(1), 132.

Grant, S., Jess, D., Stangalini, M., Jafarzadeh, S., Fedun, V., Verth, G., Keys, P., Rajaguru, S., Uitenbroek, H., MacBride, C. et al. (2022), 'The propagation of coherent waves across multiple solar magnetic pores', *The Astrophysical Journal* **938**(2), 143.

Griffiths, M., Gyenge, N., Zheng, R., Korsós, M. and Erdélyi, R. (2023), 'p-mode oscillations in highly gravitationally stratified magnetic solar atmospheres', *Physics* **5**(2), 461–482.

Hou, Y., Li, T., Zhong, S., Yang, S., Guo, Y., Li, X., Zhang, J. and Xiang, Y. (2020), 'Sunspot penumbral filaments intruding into a light bridge and the resultant reconnection jets', *Astronomy & Astrophysics* **642**, A44.

Jess, D. B., Jafarzadeh, S., Keys, P. H., Stangalini, M., Verth, G. and Grant, S. D. T. (2022), 'Waves in the lower solar atmosphere: the dawn of next-generation solar telescopes', *arXiv e-prints* p. arXiv:2212.09788.

Jess, D. B., Van Doorsselaere, T., Verth, G., Fedun, V., Prasad, S. K., Erdélyi, R., Keys, P. H., Grant, S. D., Uitenbroek, H. and Christian, D. J. (2017),

'An inside look at sunspot oscillations with higher azimuthal wavenumbers', *The Astrophysical Journal* **842**(1), 59.

Jess, D., De Moortel, I., Mathioudakis, M., Christian, D., Reardon, K., Keys, P. and Keenan, F. (2012), 'The source of 3 minute magnetoacoustic oscillations in coronal fans', *The Astrophysical Journal* **757**(2), 160.

Jess, D., Morton, R., Verth, G., Fedun, V., Grant, S. and Giagkiozis, I. (2015), 'Multiwavelength studies of mhd waves in the solar chromosphere', *Space Science Reviews* **190**(1), 103–161.

Ji, K., Jiang, X., Feng, S., Yang, Y., Deng, H. and Wang, F. (2016), 'Investigation of umbral dots with the new vacuum solar telescope', *Solar Physics* **291**(2), 357–369.

Kalkofen, W., Rossi, P., Bodo, G. and Massaglia, S. (1994), 'Propagation of acoustic waves in a stratified atmosphere I.', *Astron. Astrophys.* **284**, 976–984.

Kang, J., Chae, J., Nakariakov, V. M., Cho, K., Kwak, H. and Lee, K. (2019), 'The physical nature of spiral wave patterns in sunspots', *The Astrophysical Journal Letters* **877**(1), L9.

Keppens, R., Bogdan, T. J. and Goossens, M. (1994), 'Multiple Scattering and Resonant Absorption of p-Modes by Fibril Sunspots', *Astrophys. J.* **436**, 372.

Kerr, G. S. (2023), 'Interrogating solar flare loop models with iris observations 2: Plasma properties, energy transport, and future directions', *Frontiers in Astronomy and Space Sciences* **9**, 1060862.

Keys, P. H., Morton, R. J., Jess, D. B., Verth, G., Grant, S. D., Mathioudakis, M., Mackay, D. H., Doyle, J. G., Christian, D. J., Keenan, F. P. et al. (2018), 'Photospheric observations of surface and body modes in solar magnetic pores', *The Astrophysical Journal* **857**(1), 28.

Khomenko, E. and Collados, M. (2015), 'Oscillations and waves in sunspots', *Living Reviews in Solar Physics* **12**(1), 1–78.

Kilcik, A., Sarp, V., Yurchyshyn, V., Rozelot, J.-P. and Ozguc, A. (2020), 'Physical Characteristics of Umbral Dots Derived from a High-Resolution Observations', *Solar Phys.* **295**(4), 58.

Kwon, Y. W. and Bang, H. (2018), *The finite element method using MATLAB*, CRC press.

Leighton, R. B., Noyes, R. W. and Simon, G. W. (1962), 'Velocity Fields in the Solar Atmosphere. I. Preliminary Report.', *Astrophys. J.* **135**, 474.

Li, B., Antolin, P., Guo, M. Z., Kuznetsov, A. A., Pascoe, D. J., Van Doorsselaere, T. and Vasheghani Farahani, S. (2020), 'Magnetohydrodynamic Fast Sausage Waves in the Solar Corona', *Space Sci. Rev.* **216**(8), 136.

Li, K., Li, J., Lu, X. and Chen, S. (2022), 'Heating and acceleration of ions with kappa distribution functions by low-frequency alfvén wave', *Contributions to Plasma Physics* **62**(3), e202100056.

Lighthill, M. J. (1960), 'Studies on magneto-hydrodynamic waves and other anisotropic wave motions', *Philosophical Transactions of the Royal Society of London. Series A, Mathematical and Physical Sciences* **252**(1014), 397–430.

Lites, B. (1984), 'Photoelectric observations of chromospheric sunspot oscillations. ii-propagation characteristics', *The Astrophysical Journal* **277**, 874–888.

Louis, R. E., Bayanna, A. R., Mathew, S. K. and Venkatakrishnan, P. (2008), 'Dynamics of sunspot light bridges as revealed by high-resolution images from hinode', *Solar Physics* **252**(1), 43–54.

Louis, R. E., Beck, C. and Ichimoto, K. (2014), 'Small-scale chromospheric jets above a sunspot light bridge', *Astronomy & Astrophysics* **567**, A96.

Louis, R. E., Ravindra, B., Mathew, S. K., Rubio, L. R. B., Bayanna, A. R. and Venkatakrishnan, P. (2012), 'Analysis of a fragmenting sunspot using hinode observations', *The Astrophysical Journal* **755**(1), 16.

Markwick, R., Frank, A., Blackman, E., Carroll-Nellenback, J., Lebedev, S., Russell, D., Halliday, J., Suttle, L. and Hartigan, P. (2024), 'Cooling and instabilities in colliding radiative flows with toroidal magnetic fields', *Monthly Notices of the Royal Astronomical Society* p. stae312.

Mathioudakis, M., Jess, D. B. and Erdélyi, R. (2013), 'Alfvén Waves in the Solar Atmosphere. From Theory to Observations', *Space Sci. Rev.* **175**(1-4), 1–27.

Moore, R. (1981), 'Dynamic phenomena in the visible layers of sunspots', *Space Science Reviews* **28**(4), 387–421.

Morton, R., Erdélyi, R., Jess, D. and Mathioudakis, M. (2011*a*), 'Observations of sausage modes in magnetic pores', *The Astrophysical Journal Letters* **729**(2), L18.

Morton, R. J., Erdélyi, R., Jess, D. B. and Mathioudakis, M. (2011*b*), 'Observations of Sausage Modes in Magnetic Pores', *Astrophys. J. Lett.* **729**(2), L18.

Morton, R. J., Verth, G., Jess, D. B., Kuridze, D., Ruderman, M. S., Mathioudakis, M. and Erdélyi, R. (2012), 'Observations of ubiquitous compressive waves in the sun's chromosphere', *Nature Communications* **3**(1), 1–8.

Morton, R., Tomczyk, S. and Pinto, R. (2015), 'Investigating alfvénic wave propagation in coronal open-field regions', *Nature Communications* **6**(1), 7813.

Morton, R., Weberg, M. and McLaughlin, J. (2019), 'A basal contribution from p-modes to the alfvénic wave flux in the sun's corona', *Nature Astronomy* **3**(3), 223–229.

Nagashima, K., Sekii, T., Kosovichev, A. G., Shibahashi, H., Tsuneta, S., Ichimoto, K., Katsukawa, Y., Lites, B., Nagata, S., Shimizu, T. et al. (2007), 'Observations of sunspot oscillations in g band and ca ii h line with solar optical telescope on hinode', *Publications of the Astronomical Society of Japan* **59**(sp3), S631–S636.

Nakariakov, V. M. and Kolotkov, D. Y. (2020), 'Magnetohydrodynamic waves in the solar corona', *Annual Review of Astronomy and Astrophysics* **58**, 441–481.

Nakariakov, V., Ofman, L., Deluca, E., Roberts, B. and Davila, J. (1999), 'Trace observation of damped coronal loop oscillations: Implications for coronal heating', *Science* **285**(5429), 862–864.

Nicholeen, M. V., De Moortel, I., Downs, C., Klimchuk, J., Parenti, S. and Reale, F. (2022), 'The coronal heating problem', *Authorea Preprints* .

Oliver, R. (2009), 'Prominence Seismology Using Small Amplitude Oscillations', *Space Sci. Rev.* **149**(1-4), 175–197.

Ortiz, A., Rubio, L. B. and van der Voort, L. R. (2010), 'Downflows in sunspot umbral dots', *The Astrophysical Journal* **713**(2), 1282.

O'shea, E., Muglach, K. and Fleck, B. (2002), 'Oscillations above sunspots: Evidence for propagating waves?', *Astronomy & Astrophysics* **387**(2), 642–664.

Pagano, P., De Moortel, I. and Morton, R. (2020), 'Effect of coronal loop structure on wave heating through phase mixing', *Astronomy & Astrophysics* **643**, A73.

Parker, E. (1974), 'The nature of the sunspot phenomenon. ii: Internal overstable modes', *Solar Physics* **37**, 127–144.

Parker, E. (1979), 'Sunspots and the physics of magnetic flux tubes. ix-umbral dots and longitudinal overstability', *The Astrophysical Journal* **234**, 333–347.

Pozuelo, S. E., Rubio, L. B. and de la Cruz Rodriguez, J. (2015), 'Lateral downflows in sunspot penumbral filaments and their temporal evolution', *The Astrophysical Journal* **803**(2), 93.

Priest, E. (2014*a*), *Magnetohydrodynamics of the Sun*, Cambridge University Press.

Priest, E. (2014*b*), *Magnetohydrodynamics of the Sun*, Cambridge University Press.

Rae, I. C. and Roberts, B. (1982), 'Pulse propagation in a magnetic flux tube', *Astrophys. J.* **256**, 761–767.

Riedl, J. M., Gilchrist-Millar, C. A., Van Doorsselaere, T., Jess, D. B. and Grant, S. D. (2021), 'Finding the mechanism of wave energy flux damping in solar pores using numerical simulations', *Astronomy & Astrophysics* **648**, A77.

Riethmüller, T., Solanki, S., Zakharov, V. and Gandorfer, A. (2008), 'Brightness, distribution, and evolution of sunspot umbral dots', *Astronomy & Astrophysics* **492**(1), 233–243.

Rimmele, T. (2008), 'On the relation between umbral dots, dark-cored filaments, and light bridges', *The Astrophysical Journal* **672**(1), 684.

Roberts, B. (1981*a*), 'Wave propagation in a magnetically structured atmosphere', *Solar Physics* **69**(1), 39–56.

Roberts, B. (1981*b*), 'Wave propagation in a magnetically structured atmosphere, surface waves at a magnetic interface', *Solar Physics* **69**(1), 27–38.

Roberts, B. (1981*c*), 'Wave propagation in a magnetically structured atmosphere, waves in a magnetic slab', *Solar Physics* **69**(1), 39–56.

Roberts, B. (2019), *MHD waves in the solar atmosphere*, Cambridge University Press.

Ruderman, M. S. and Roberts, B. (2002), 'The Damping of Coronal Loop Oscillations', *Astrophys. J.* **577**(1), 475–486.

Sakurai, T., Goossens, M. and Hollweg, J. V. (1991*a*), 'Resonant Behaviour of Magnetohydrodynamic Waves on Magnetic Flux Tubes - Part One', *Solar Phys.* **133**(2), 227–245.

Sakurai, T., Goossens, M. and Hollweg, J. V. (1991*b*), 'Resonant behaviour of mhd waves on magnetic flux tubes', *Solar Physics* **133**(2), 227–245.

Sathej, G. and Adhikari, R. (2009), 'The eigenspectra of indian musical drums', *The Journal of the Acoustical Society of America* **125**(2), 831–838.

Schüssler, M. and Vögler, A. (2006), 'Magnetoconvection in a sunspot umbra', *The Astrophysical Journal* **641**(1), L73.

Shi, T., Manchester, W., Landi, E., van der Holst, B., Szente, J., Chen, Y., Tóth, G., Bertello, L. and Pevtsov, A. (2024), 'Awsom magnetohydrodynamic simulation of a solar active region. ii. statistical analysis of alfvén wave dissipation and reflection, scaling laws, and energy budget on coronal loops', *The Astrophysical Journal* **961**(1), 60.

Sigalotti, L. D. G. and Cruz, F. (2023), 'Unveiling the mystery of solar-coronal heating', *Physics Today* **76**(4), 34–40.

Skirvin, S., Fedun, V., Silva, S. S. and Verth, G. (2022*a*), 'Ii. the effect of axisymmetric and spatially varying equilibria and flow on mhd wave modes: cylindrical geometry', *Monthly Notices of the Royal Astronomical Society* **510**(2), 2689–2706.

Skirvin, S., Fedun, V. and Verth, G. (2021), 'I. the effect of symmetric and spatially varying equilibria and flow on mhd wave modes: slab geometry', *Monthly Notices of the Royal Astronomical Society* **504**(3), 4077–4092.

Skirvin, S. J., Fedun, V., Silva, S. S. A. and Verth, G. (2022*b*), 'II. The effect of axisymmetric and spatially varying equilibria and flow on MHD wave modes: cylindrical geometry', *Mon. Not. Roy. Astron. Soc.* **510**(2), 2689–2706.

Sobotka, M. (2003), 'Solar activity ii: Sunspots and pores', *Astronomische Nachrichten: Astronomical Notes* **324**(4), 369–373.

Sobotka, M. and Hanslmeier, A. (2005), 'Photometry of umbral dots', *Astronomy & Astrophysics* **442**(1), 323–329.

Solanki, S. K. (2003), 'Sunspots: an overview', *The Astronomy and Astrophysics Review* **11**(2), 153–286.

Solar Dynamics Observatory (SDO) (n.d.), https://sdo.gsfc.nasa.gov Solar Dynamics Observatory (SDO) . Accessed: 2021-12-03.

Soler, R., Terradas, J., Oliver, R. and Ballester, J. L. (2017), 'Propagation of torsional alfvén waves from the photosphere to the corona: reflection, transmission, and heating in expanding flux tubes', *The Astrophysical Journal* **840**(1), 20.

Spruit, H. (1982), 'Propagation speeds and acoustic damping of waves in magnetic flux tubes', *Solar Physics* **75**(1), 3–17.

Srivastava, A., Singh, B., Murawski, K., Chen, Y., Sharma, K., Yuan, D., Tiwari, S. and Mathioudakis, M. (2023), 'Impulsive origin of solar spicule-like jets', *The European Physical Journal Plus* **138**(3), 209.

Stangalini, M., Del Moro, D., Berrilli, F. and Jefferies, S. (2011), 'Mhd wave transmission in the sun's atmosphere', *Astronomy & Astrophysics* **534**, A65.

Stangalini, M., Jess, D. B., Verth, G., Fedun, V., Fleck, B., Jafarzadeh, S., Keys, P. H., Murabito, M., Calchetti, D., Aldhafeeri, A. A. et al. (2021), 'A novel approach to identify resonant mhd wave modes in solar pores and sunspot umbrae: $b-\backslash$omega $analysis', arXivpreprintarXiv$: 2103.11639.

Stangalini, M., Verth, G., Fedun, V., Aldhafeeri, A. A., Jess, D., Jafarzadeh, S., Keys, P., Fleck, B., Terradas, J., Murabito, M. et al. (2022), 'Large scale coherent magnetohydrodynamic oscillations in a sunspot', *Nature communications* **13**(1), 1–9.

Sutmann, G., Musielak, Z. E. and Ulmschneider, P. (1998), 'Acoustic wave propagation in the solar atmosphere. III. Analytic solutions for adiabatic wave excitations', *Astron. Astrophys.* **340**, 556–568.

The Swedish Solar Telescope (SST) (n.d.), https://www.iac.es/en?op1=2&op2=3&id=10 The Swedish Solar Telescope (SST) . Accessed: 2021-12-03.

Thomas, J. H., Cram, L. E. and Nye, A. H. (1984), 'Dynamical phenomena in sunspots. I - Observing procedures and oscillatory phenomena.', *Astrophys. J.* **285**, 368–385.

Thomas, J. H. and Weiss, N. O. (2004), 'Fine structure in sunspots', *Annual Review of Astronomy and Astrophysics* **42**(1), 517–548.

Thomas, J. H., Weiss, N. O., Tobias, S. M. and Brummell, N. H. (2002), 'Downward pumping of magnetic flux as the cause of filamentary structures in sunspot penumbrae', *Nature* **420**(6914), 390–393.

Tomczyk, S., McIntosh, S., Keil, S., Judge, P., Schad, T., Seeley, D. and Edmondson, J. (2007), 'Alfvén waves in the solar corona', *Science* **317**(5842), 1192–1196.

Trefethen, L. N. (2000), *Spectral methods in MATLAB*, SIAM.

Trefethen, L. N. (2023), 'Numerical analytic continuation', *Japan Journal of Industrial and Applied Mathematics* pp. 1–50.

van der Voort, L. R., Rubio, L. B. and Ortiz, A. (2010), 'Upflows in the central dark lane of sunspot light bridges', *The Astrophysical Journal Letters* **718**(2), L78.

Van Doorsselaere, T., Nakariakov, V. M. and Verwichte, E. (2008), 'Detection of waves in the solar corona: kink or alfvén?', *The Astrophysical Journal* **676**(1), L73.

Van Doorsselaere, T., Srivastava, A. K., Antolin, P., Magyar, N., Vasheghani Farahani, S., Tian, H., Kolotkov, D., Ofman, L., Guo, M., Arregui, I., De Moortel, I. and Pascoe, D. (2020), 'Coronal Heating by MHD Waves', *Space Sci. Rev.* **216**(8), 140.

Verth, G. (2007), 'Magneto-seismology of the solar atmosphere', *Astronomische Nachrichten* **328**(8), 764.

Watanabe, H. (2014), 'Observations of umbral dots and their physical models', *Publications of the Astronomical Society of Japan* **66**(SP1).

Watanabe, H., Kitai, R. and Ichimoto, K. (2009), 'Characteristic dependence of umbral dots on their magnetic structure', *The Astrophysical Journal* **702**(2), 1048.

Watanabe, H., Rubio, L. R. B., De la Cruz Rodríguez, J. and van der Voort, L. R. (2012), 'Temporal evolution of velocity and magnetic field in and around umbral dots', *The Astrophysical Journal* **757**(1), 49.

Williams, T., Walsh, R. W., Peter, H. and Winebarger, A. R. (2020), 'Evidence for and analysis of multiple hidden coronal strands in cross-sectional emission profiles: Further results from nasa's high-resolution solar coronal imager', *The Astrophysical Journal* **902**(2), 90.

Xu, L., Huang, Q., Wang, H., Hao, Y., Bai, Q., Hu, J., Li, Y., Wang, P., Chen, X., He, R. et al. (2017), 'The kinase mtorc1 promotes the generation and suppressive function of follicular regulatory t cells', *Immunity* **47**(3), 538–551.

Yadav, R. and Mathew, S. K. (2018), 'Physical properties of umbral dots observed in sunspots: A hinode observation', *Solar Physics* **293**(4), 1–18.

Yukio, K., Yokoyama, T., Berger, T. E., Ichimoto, K., Kubo, M., Lites, B., Nagata, S., Shimizu, T., Shine, R. A., Suematsu, Y. et al. (2007), 'Formation

process of a light bridge revealed with the hinode solar optical telescope', *Publications of the Astronomical Society of Japan* **59**(sp3), S577–S584.

Zhao, J., Su, J., Yang, X., Li, H., Schmieder, B., Ahn, K. and Cao, W. (2022), 'Chromospheric recurrent jets in a sunspot group and their intergranular origin', *The Astrophysical Journal* **932**(2), 95.

Zheng, R., Liu, Y., Liu, W., Wang, B., Hou, Z., Feng, S., Kong, X., Huang, Z., Song, H., Tian, H. et al. (2023), 'Why "solar tsunamis" rarely leave their imprints in the chromosphere', *The Astrophysical Journal Letters* **949**(1), L8.

Zsámberger, N. K., Tong, Y., Asztalos, B. and Erdélyi, R. (2022), 'Mhd wave propagation and the kelvin–helmholtz instability in an asymmetric magnetic slab system', *The Astrophysical Journal* **935**(1), 41.